



Title	STUDY ON BIOMIMETIC SQUID-LIKE UNDERWATER ROBOTS WITH TWO UNDULATING SIDE FINS
Author(s)	Rahman, Md. Mahbubar
Citation	大阪大学, 2013, 博士論文
Version Type	VoR
URL	<a href="https://doi.org/10.18910/26168">https://doi.org/10.18910/26168</a>
rights	
Note	

*The University of Osaka Institutional Knowledge Archive : OUKA*

<https://ir.library.osaka-u.ac.jp/>

The University of Osaka

**Doctoral Dissertation**

**STUDY ON BIOMIMETIC SQUID-LIKE UNDERWATER  
ROBOTS WITH TWO UNDULATING SIDE FINS**

**MD. MAHBUBAR RAHMAN**

**July 2013**

**Department of Naval Architecture and Ocean Engineering**

**Graduate School of Engineering**

**Osaka University**

**Japan**

# STUDY ON BIOMIMETIC SQUID-LIKE UNDERWATER ROBOTS WITH TWO UNDULATING SIDE FINs

A dissertation by

MD. MAHBUBAR RAHMAN

Submitted to the Department of Naval Architecture and Ocean Engineering, Division of

Global Architecture, Graduate School of Engineering, Osaka University,

in partial fulfillment of the requirements for the degree of

DOCTOR OF ENGINEERING

## **Thesis Review Committee:**

Chairman: Yasuyuki Toda (Professor)

Members: Naomi Kato (Professor)

Kiyoshige Matsumura (Associate Professor)

Hiroyoshi Suzuki (Associate Professor)

**Supervisor: Prof. Yasuyuki Toda**

**July 2013**

*Dedicated to  
those great hearts who are  
serving to the welfare of mankind unprofitably.*

সে'সব মহৎ প্রানের উদ্দেশ্যে উৎসর্গীকৃত,  
যারা মানব কল্যাণে নিঃস্বার্থভাবে নিরলস পরিশ্রম করে যাচ্ছে।

## *Acknowledgement*

*First and foremost, I offer my deepest gratitude and sincere thanks to my supervisor, Professor Yasuyuki Toda, for his cordial support throughout my thesis with his patience and knowledge. I attribute the level of PhD degree to his encouragement and effort; without him, this thesis would not have been completed. I simply can't wish for a better or friendlier supervisor.*

*I would like to express my cordial gratefulness to my lab mates; especially, the members of the group of Squid-Robot for their restless effort to bring the project in the present state.*

*I would like to thank my family and friends- particularly my parents Md. Moshir Rahman and Rokeya Begum, for giving birth to me at the first place and supporting me spiritually throughout my life; my wife Sonifa Sharmin and my son Md. Radil Mahub because of their sacrifice, cooperation and mental support during my research.*

*The financial support from Japanese Ministry of Education, Culture, Sports, Science and Technology (MEXT) in the form of Monbukagakusho fellowship is gratefully acknowledged.*

*Above all, all gratitude is due to Almighty Allah for making things and situations congenial and favorable for me for the task undertaken.*

# Contents

<b>1. Chapter 1: General Introduction.....</b>	<b>8</b>
1.1 Background .....	8
1.2 Literature Review.....	8
1.3 History of Development of the Squid-robot.....	9
1.4 Objective .....	17
<b>2. Chapter 2: Computational Study on a Squid-Like Underwater Robot with Two Undulating Side Fins.....</b>	<b>18</b>
2.1 Preamble .....	18
2.2 Introduction.....	18
2.3 Methodology .....	19
2.3.1 Experimental Set up .....	19
2.3.2 Outline of Model-4.....	21
2.3.3 Grid Generation.....	22
2.3.4 CFD Computation.....	29
2.3.5 Boundary Conditions .....	31
2.4 Computational Results of Flat Body with Side Fin .....	32
2.4.1 Forces .....	32
2.4.2 Contours.....	36
2.4.3 Fin Open Characteristics .....	42
2.4.4 Efficiency .....	44
2.4.5 Verification .....	45
2.4.6 Comparison .....	46

2.5	Computational Results of Model-4 .....	47
2.5.1	Forces .....	48
2.5.2	Contours .....	51
2.5.3	Comparison of Results .....	62
2.6	Summery .....	68
<b>3.</b>	<b>Chapter 3: Braking Performance of the Undulating Fin Propulsion System of the Squid-Robot.....</b>	<b>69</b>
3.1	Preamble .....	69
3.2	Introduction.....	69
3.3	Methodology .....	71
3.3.1	Experimental Setup.....	71
3.3.2	Simulation .....	73
3.4	Results and Discussion .....	76
3.4.1	Comparison .....	76
3.4.2	Braking in Translational Motion.....	80
3.4.3	Braking in Rotational Motion .....	84
3.5	Summery .....	88
<b>4.</b>	<b>Chapter 4: Development of a Real Time Simulator Based on the Analysis of 6-DOF Motion of the Squid-Robot (Model-4) .....</b>	<b>90</b>
4.1	Preamble .....	90
4.2	Introduction.....	90
4.3	Methodology .....	91
4.3.1	Simulation .....	91

4.3.2	Formation of Circular and Vertical Motions.....	96
4.4	Results and Discussion .....	98
4.4.1	3-DOF Circular Motion .....	99
4.4.2	3-DOF Vertical Motion.....	102
4.4.3	Spiral Motion using Side Fin and Caudal Fin .....	104
4.4.4	Spiral Motion using Only Side Fin .....	106
4.4.5	Real Time Simulator .....	113
4.5	Summery .....	116
<b>5.</b>	<b>Chapter 5:.....</b>	<b>117</b>
5.1	General Conclusion.....	117
5.2	Future Plan.....	118
	<b>Reference .....</b>	<b>119</b>

# **1. Chapter 1: General Introduction**

## **1.1 Background**

Oceans, seas and adjoining coastal regions are essential constituents of the Earth's ecosystem playing critical roles in global food security, transportation and more generally the human existence. Mankind has conquered the surface of the water world and their footprints are visible everywhere on the surface of the hydrosphere. However, the world of underwater - the main source of resources has remained almost unexplored largely due to the inaptness of traditional exploration technology. The underwater robot is a basic tool to explore the unknown resources or sunken ship in the complicated sea bed topology of the coastal area and oceans, both from the scientific and industrial perspectives. For designing a competent and environmentally friendly underwater vehicle, usually robotic engineers borrow the sense and structure from the animals of the ocean to optimize their designs. Aquatic animals are the smart swimmers so the naval architects investigate their swimming mechanisms to improve the design of underwater vehicles. Different types of underwater vehicles and robots have been developed for solving different purpose; however there is still huge scope to contribute this vast and important field.

## **1.2 Literature Review**

The increasing demand for high-performance underwater vehicle has attracted many researchers in studying this challenging but intellectually satisfying field. A lot of studies have been conducted theoretically, numerically and experimentally with respect to the swimming motion of fishes for understanding the mechanism of the propulsion of fish for applying the mechanism to the artificial underwater vehicle. Many books (e.g. Barrett et al. (1999), Kato et al. (2004)), conference proceedings (e.g. Proceedings of ISABMEC 2000, 2003, 2006, 2009, 2012), review papers (e.g. Sfakiotakis et al. (1999)) and academic papers (e.g. Kato (2000), Heo et al. (2010), Riggs et al. (2010), Zhang et al. (2012)) have been published.

Based on the propulsive structure, Breder (1926) identified two modes in fish swimming - Body and/or caudal fin (BCF) and median and/or paired Fin (MPF). The BCF movement yields greater thrust and accelerations while the MPF is employed at slower speeds to attain greater maneuverability and better propulsive efficiency. The present study was based on the undulating side-fin propulsion robot, which is belonging to the MPF group. In the field of underwater robotic research, undulating-fin robot offers exceptional advantage over propeller in preserving an undisturbed condition of its surroundings for data acquisition. Though the movement of this biomimetic type of robot is slow, it has compelling areas of applications such as underwater localization, acoustic communications, optical and acoustic imagery, guidance navigation and control, mission planning and mapping etc. Military and defense are the most important areas where biomimetics finds its significant role in ensuring safety and covertness. The undulating finned robot might be undetected when swims with a school of fish and therefore may find its application as an espionage tool. Considering the usefulness of the undulating fin propulsion system, many researchers are interested in studying in this field. Many new concepts of biologically inspired underwater propulsion systems have been developed including several undulating-finned underwater robots. The computational study on the undulating fin of a bio-robot was conducted by Zhang et al., (2006) and Zhang et al., (2007). The biomimetic design and the workspace study of undulating fin propulsion mechanisms of fish with long and/or wide undulating body/fin were discussed by Low (2009). The motion control of an underwater robotic fish with two undulating long fins was studied by Shang et al. (2009). Unfortunately, till date, the development of capable and eco-friendly underwater vehicle with undulating side fins is not up to the mark and it offers adequate opportunity to contribute to this field.

### **1.3 History of Development of the Squid-robot**

A squid-like underwater robot with two undulating side fins has been studied in the Laboratory of Hull Form Design of Osaka University for several years. The investigation aimed at the development of a competent and eco-friendly underwater vehicle. The idea was borrowed from some fishes which

use undulating side fins for swimming in the underwater; e.g. Squid, Stingray, Cuttlefish, Manta etc. (Fig.1.1).

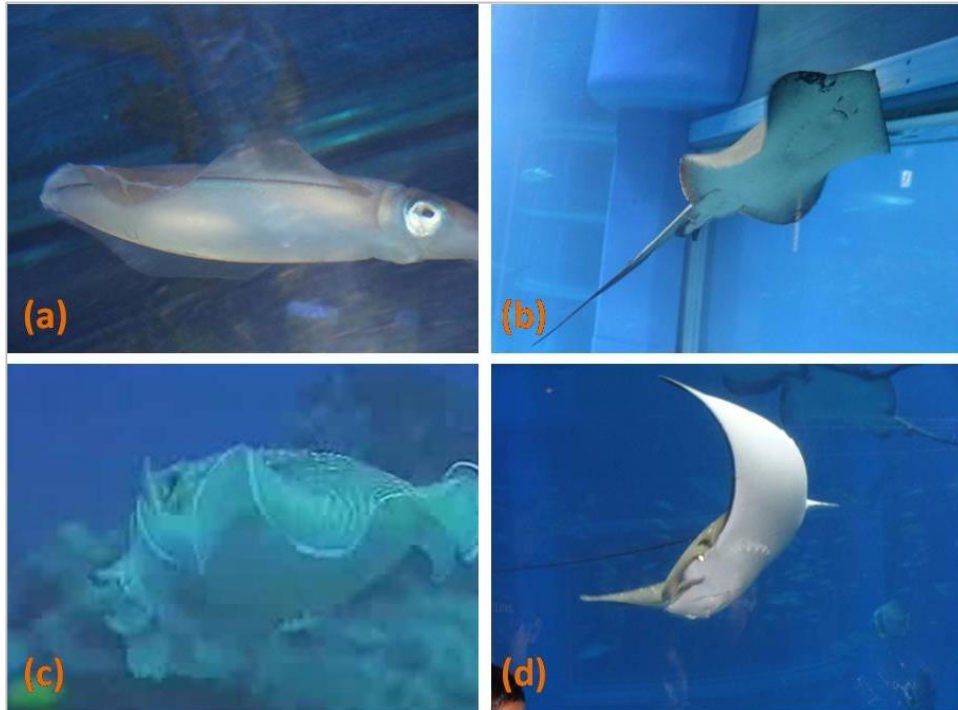


**Fig. 1.1 Fishes which use undulating side fins for swimming; (a) Squid, (b) Stingray, (c) Cuttlefish, (d) Manta**

The project started at 2002 by constructing the primary model, **Model-1**. The picture of the Model-1 at different angles is shown in Fig. 1.2. The computation of the flow field around the simple model with undulating fins and resistance body was presented by Toda et al., (2002A). The feature of flow field and hydrodynamic forces acting on the body and fins was elucidated based on the computed results to augment the understanding of the complex fluid mechanics that fishes use to propel themselves. These results were good information for understanding the complex fluid mechanics that a kind of fishes uses to propel itself.

A preliminary experiment of Model-1 with a strut operated at very low frequency was presented in the 1<sup>st</sup> APHydro conference by Toda et al., (2002B). Model-1 has a resistance body and the two fins are attached the side of the resistance body. The driving part that has two motors and encoders for

driving each fin and the fish-like body are connected by a big strut. Each fin ray was controlled by scotch yoke mechanism to make the progressive wave fin's motion.



**Fig. 1.2 Model-1 of the Squid-robot**

Next, **Model-2** was constructed in 2004 (Toda et al. 2004) which consisted of 16 servomotors for both sides that were controlled independently by the computer from outside to make any kind of motions of the fin. From Fig. 1.3, it is seen that this model was free from strut but still consisted of large cables.

The strut of Model-1 and the bulky cables of Model-2 hindered their free movement for which **Model-3** was constructed without strut and hefty cable (Toda et al., 2006). Model-3 had 17 servo motors for both sides to produce any fin's motion with the servo controller and the microcomputer being housed inside the model (Fig. 1.4). The model has one thin cable that is connected to the floating wireless communication units to the computer on the ground for control.

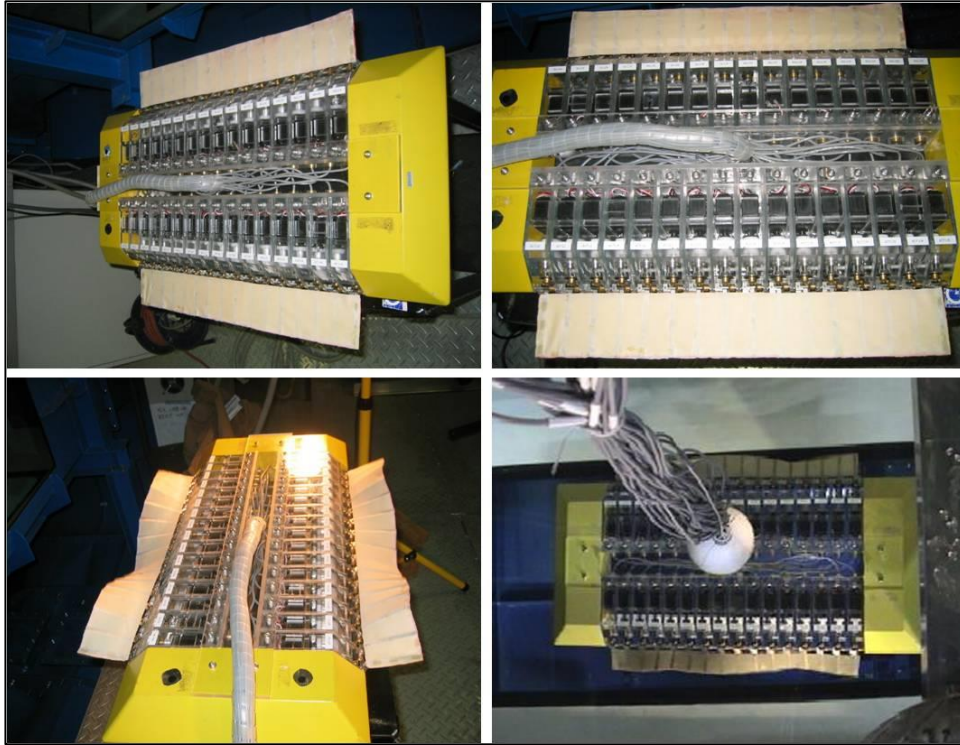


**Fig. 1.3 Model-2 of the Squid-robot**

It can run freely to any direction and change the angle around any axis. It had the dorsal fin to keep a direction and the caudal fin to change the depth. These fins also can be controlled timely by the ground computer. The adjustment of vertical gravity center was also attached and controlled by the ground computer. Various motions were demonstrated through free-run tank experiment and numerical simulation using the hydrodynamic coefficients obtained by captive model tests. The model could turn over on its back. By using Model-3, the motion in the 6 degree of freedom direction was demonstrated and controlled easily. But the gravity center adjustment device was attached on the resistance body. So, it had the resistance and made some asymmetric hydrodynamic forces. And the RS232C protocol was used for wireless communication. So, it had a trouble in communication at large distance.

In order to overcome these discrepancies, the **Model-4** was constructed in 2009 (Fig. 1.5). In this model, the LAN communication device and the gravity center adjustment system was introduced.

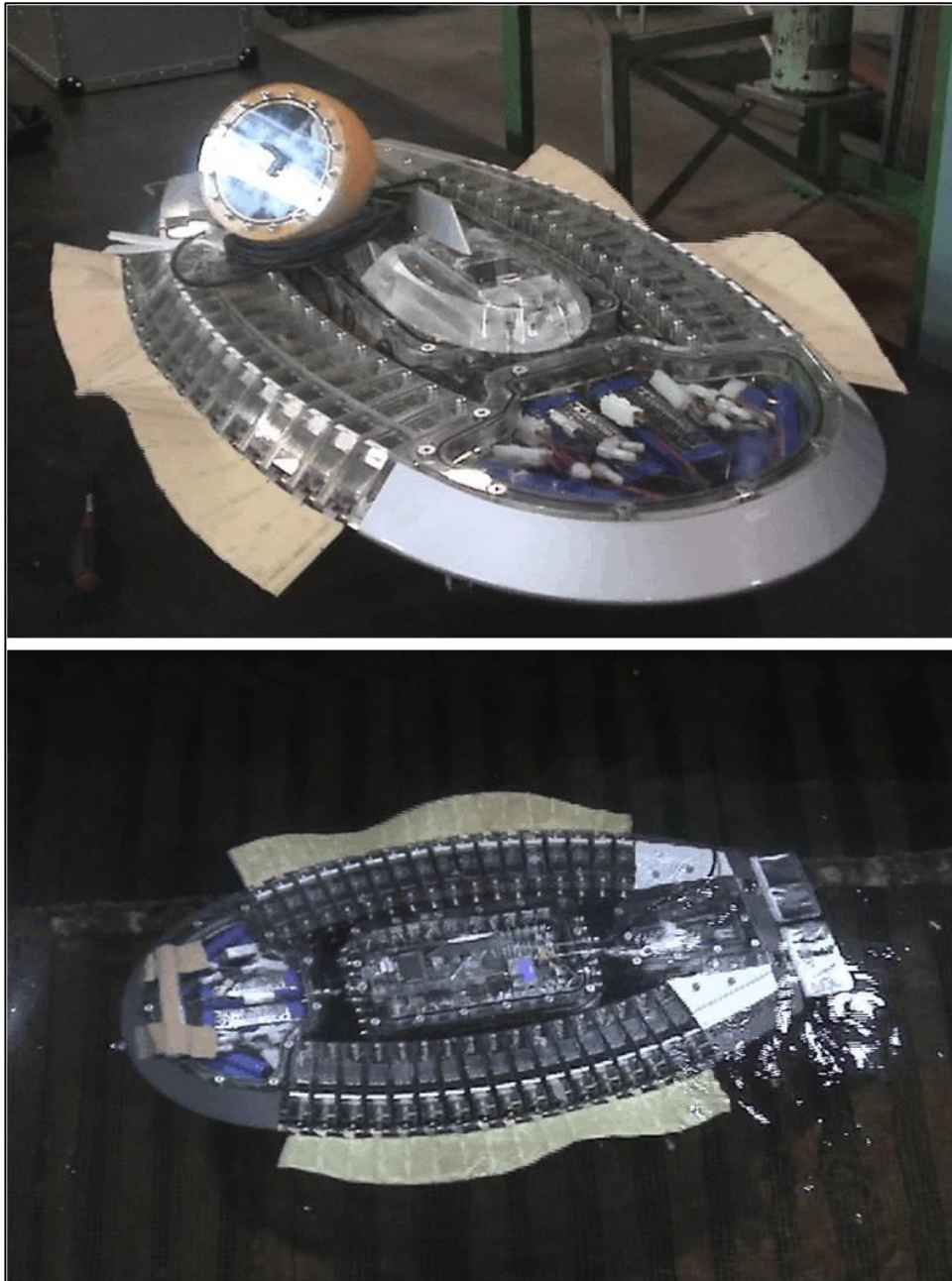


**Fig. 1.4 Model-3 of the Squid-robot**

The detailed description on the configuration of Model-4 will be discussed in the Chapter 2 (Section 2.3.2). The brief description of the Model-4 along with the force calculations and free-run tests were presented through towing tank experiments in the 4<sup>th</sup> ISABMEC conference (Toda et al., 2009). The simple prediction for different aspect ratio of the side fins was also shown. Some studies were also conducted based on the experiment, CFD computation and motion simulation using Model-4 and

similar bodies by the present author (Rahman et al. 2010A, 2010B, 2011, 2012, 2013A and 2013B).The Model-4 shows improved performance than the previous models.



**Fig. 1.5 Model-4 of the Squid-robot**

In the continuous development of a competent and eco-friendly underwater robot, recently **Model-5** has been constructed (Fig. 1.6). This model is the simplest model among all models of the Squid-robot. The undulating motion of the side fins of Model-5 are produced by using the Scotch Yoke mechanism. In one unit of Scotch Yoke, a small and a large gear are connected with the long shaft of the motor and a bone is connected with the system so that it moves only up-down direction. There are seven such units in one side of the robot and only one motor is used to move seven bones. Mountain-shaped side fins are made by covering the bones by thin rubber sheet. There are also two caudal fins attached at the tail of the robot which are connected to separate motor. The motors for the side fins and tail fins can be controlled independently by a commercially available radio-controller. The linear motion and rotational motion can be made by manipulating the voltage of the motors of the side fins. Also the tail

fins can be controlled by the same controller to move the robot up or down. Using this wireless controller, the robot can be controlled up to 70 m long and about 5.0 m depth in the water.

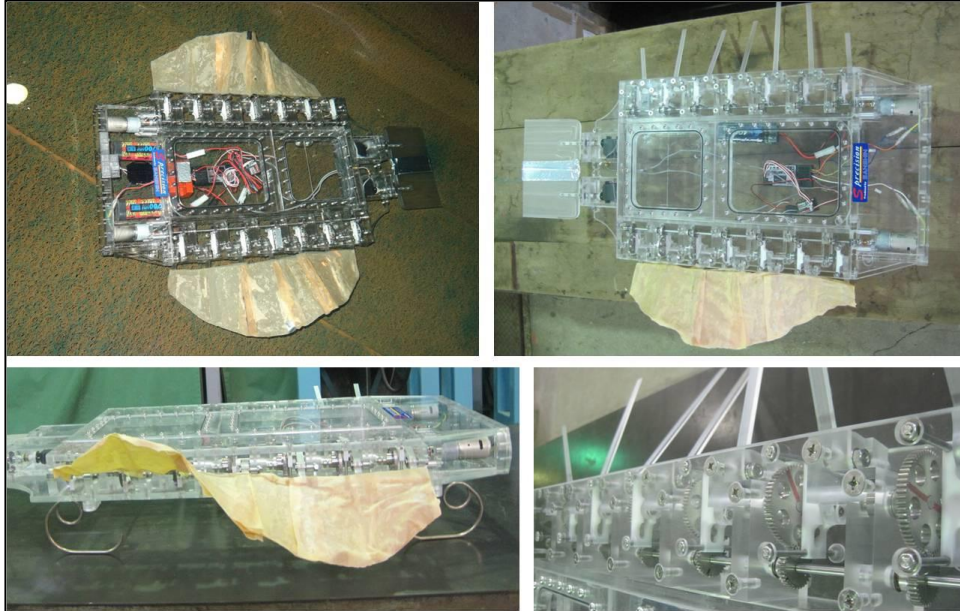


**Fig. 1.6 Model-5 of the Squid-robot**

The Model-4 had an opportunity of swimming with the real fish at the Suma Aqua-life Park, Kobe, Japan. Also, Model-4 and Model-5 attained in some Underwater Robot Festivals in Kobe, Japan and attained great achievements. The pictures are shown in Fig. 1.7 and Fig. 1.8.

The robot could swim freely in any direction using its undulating fin propulsion system. The side fins of the robot have been successfully used to make the straight line motions in surge, sway and heave directions and also to make the rotating motions in roll, pitch and yaw directions by changing the frequency and progressive wave direction or the vertical center of standing wave motion on the fin. Our robot swam freely in the environment similar to real coastal water with tidal current. Interestingly, the robot didn't annoy the fishes – fishes were not scared swimming together with it and they did not attack it; which proves the environmental friendliness of the robot.

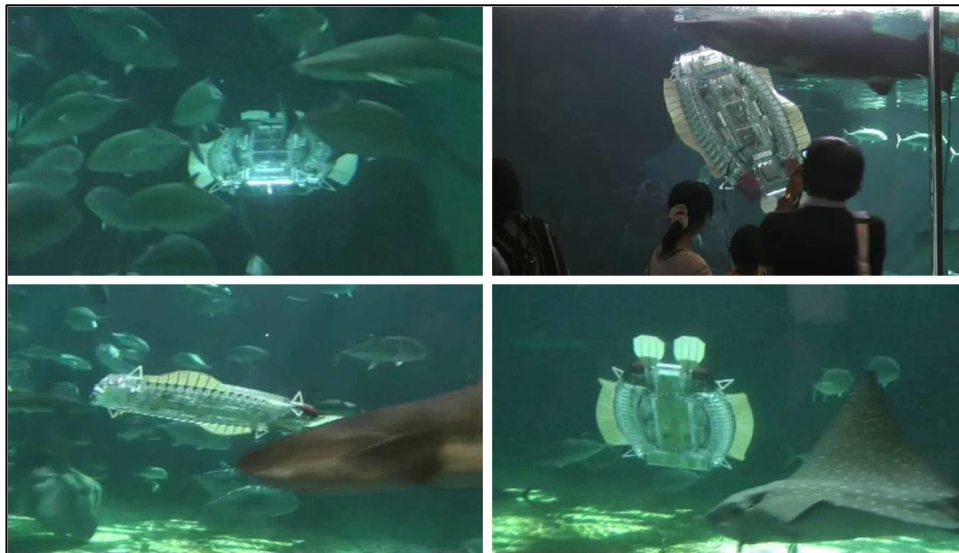


**Fig. 1.7 Squid-robot (Model-4) is swimming with the real fish at the Suma Aqua-life Park, Japan.**



**Fig. 1.8 Squid-robots (Model-4 & Model-5) in the underwater robot festivals**

## 1.4 Objective

The intent of this research was twofold: First, computation of flow field of the Squid-like underwater robot with two undulating side fins. Second, simulation of motion of the Squid-robot with undulating fins. In both cases, the computed and simulated results were compared with that of the experiment.

The specific studies are:

1. Development of the computational code to recognize the flow physics around undulating side fins of the Squid-robot.
2. Establishment of a simple relationship among the undulating side fin's principal particulars and hydrodynamic forces.
3. Analysis of the thrust force produced by the undulating fin propulsion system of the squid-robot.
4. Investigation of the flow field around the Model-4 of the Squid-robot through experimentation and computation.
5. Investigation of braking performance of the undulating side fin propulsion system.
6. Investigation of the motion of a Squid-robot through towing tank experiment and simulation of 6-DOF mathematical model in 3D space.
7. Development of the real time simulator of the Squid-robot.

## **2. Chapter 2: Computational Study on a Squid-Like Underwater Robot with Two Undulating Side Fins**

### **2.1 Preamble**

In this study, the computation of the flow field around bodies with two undulating side fins similar to Squid-robot was investigated. At first, the computation was conducted on a flat body with two undulating side fins then the computation was extended to Model-4 of the Squid-robot. The Finite Analytic Method for space discretization and Euler Implicit Scheme for time discretization along with the PISO algorithm for velocity pressure coupling were used in the computation. Body-fitted moving grids were generated around the bodies using the Poisson equation at each time step. Based on the computed results, the features of the flow field and hydrodynamic forces acting on the body and fin were discussed. A simple relationship among the fin's principle dimensions was established. Subsequently, the relationship was examined base on the distribution of the thrust force on the fin surface. Finally, for the fin, the open characteristics from computed data were compared with the experimental observations.

### **2.2 Introduction**

In our laboratory, a squid-like underwater robot with undulating side fins similar to that of a Stingray or a Cuttlefish has been under active investigation for many years. Our investigation aimed at the development of a competent and environmentally friendly underwater vehicle. This is a continuous process of development; many experimental and computational studies have been conducted. An experimental study was presented in the 4<sup>th</sup> ISABMEC conference in Shanghai, china (Toda et al. 2009). In that study, the free run tests are presented through towing tank experiments. The force measurements was conducted and compared with the results for Model-3. The simple prediction for different aspect ratio of fin was also shown and the Model-4 shows improved performance than previous models. However, it is known that the experimental and numerical studies are

complementary to each other. Experiments give the total force characteristics while the detail analysis of force can only be obtained through the numerical study. In this chapter, the flow field computation around the bodies similar to that of Squid-robot with two undulating side fins are discussed. At first, the flow field computation around a flat body with two undulating side fins was studied. The fins are similar to that of Model-4; however the body is considered as flat for convenience in grid generation. Then the computation was extended to the real Model-4 of the Squid-robot. The main objectives were to recognize the flow physics around the undulating fin and to investigate the mechanism of thrust generation. A simple relationship among the undulating side fin's principal particulars and hydrodynamic forces was also established through numerical analysis of the flow physics around the fin. The computed results were compared with the experimental results and found good conformity.

## **2.3 Methodology**

### **2.3.1 Experimental Set up**

The experiment was conducted in the Towing Tank of Osaka University (width 8m, depth 4.5m, length 100m) Fig. 2.1(a). The hydrodynamic force measurements were carried out to examine the relation among the thrust produced by fins, the advance speed and the frequency of the fin. The sketch of the experiment is shown in Fig. 2.1(b). Here the arrangement of the equipments used in the experiment can be understood. The experiment was installed in a carriage and a dynamometer was attached at the top of the model. The data detected by the dynamometer was saved in a personal computer through AC/DC converter and then analyzed the value. A picture of the experiment and the experimental condition is also shown in Fig. 2.1(c). The axial force, carriage speed and frequency of the fins were measured at steady state. From these experiments, most of hydrodynamic derivatives of mathematical model were obtained.

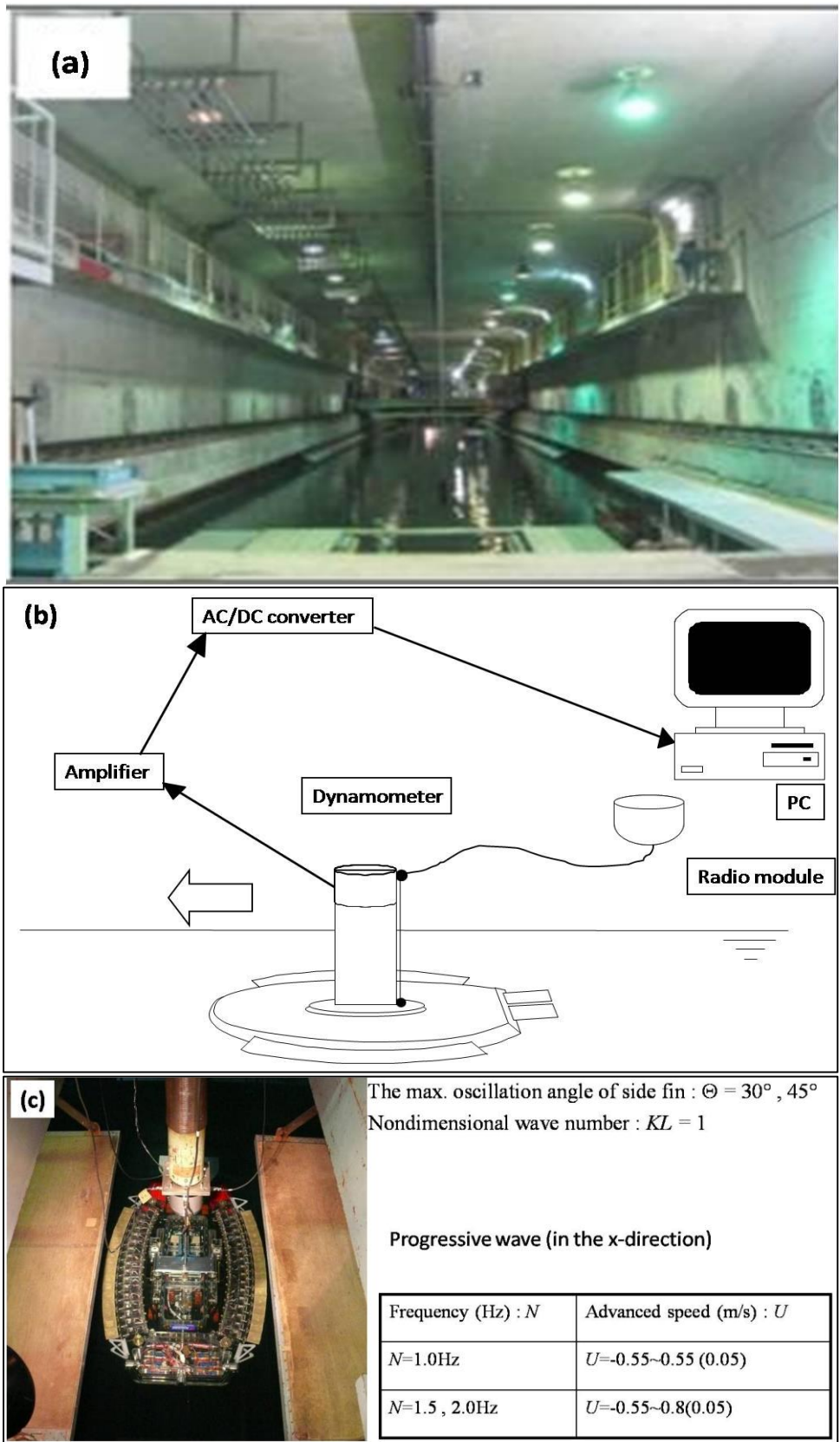
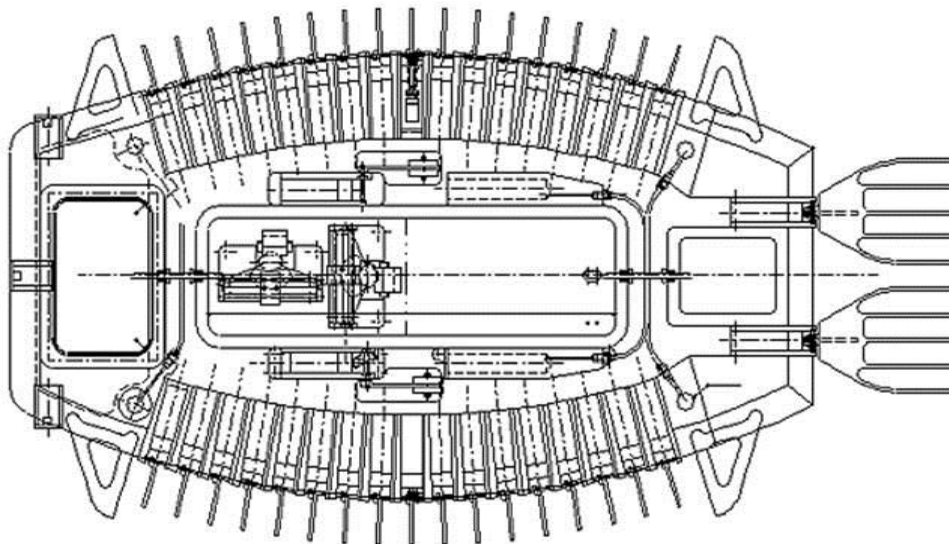


Fig. 2.1 (a) Towing Tank of Osaka University; (b) Sketch of the experimental set up  
 (c) Picture of the experiment with experimental condition

### 2.3.2 Outline of Model-4

The Model-4, a better creation than the previous models was constructed in 2009. Alike the second and third models it has the 17 servo motor units at each side to produce any kind of fin's motion the servo controllers and the microcomputer unit are board inside the model. The model has a thin cable (6m) to connect with the floating wireless communication unit. This can be controlled by the computer on the ground. The robot can run freely to any direction and change the angle around any axis. It is possible to move the model for about 4 hours using 10 batteries installed inside the model. It has also two caudal fins longer than Model-3 which is used to change the trim angle to change the depth during swimming. These fins can also be controlled by the ground computer. The brief drawing of the Model-4 is shown in Fig. 2.2 and the principal dimensions are given in Table 2.1. The fin width is same as that of the Model-3; so, the aspect ratio of fin is different from Model-3. The wireless communication system was changed to the general wireless LAN from RS232C system for better communication for both distance and speed. The usual devices of home use are used for wireless LAN.



**Fig. 2.2 Design of Model-4**

The center of gravity position can be adjusted by the system inside the model both vertically and horizontally (longitudinally and laterally). The weights can be moved by servo motors. The buoyancy

can be controlled by the change of the air volume of the two pistons (100cm<sup>3</sup> each) at both sides and the pistons are controlled by servo motors. On the control board, the CPU (Renesas SH1 HD6417032F-20), position signal generator, LAN port (LANTRONIX XP100200S- 03R) and servo motor controllers are installed inside the model. The control system and the process of data collection were discussed in detail the 4<sup>th</sup> ISABMEC conference (Toda *et al.*, 2009).

**Table 2.1: The Principal Particulars of Model-4**

	Fuselage (m)	Side fin (m)	Tail fin (m)
Length	1.3	0.874 (outside) 0.833 (inside)	0.22
Width	0.714	0.075	0.17
Thickness	0.1	0.0005	0.0005
Distance between gravity and buoyancy center (BG)	0.0002~ 0.003*		
Total weight	62.8 (kg)		

\*BG can be changed from 0.2mm to 3mm by moving vertical gravity center using the device.

### 2.3.3 Grid Generation

#### 2.3.3.1 Grid on a Flat Plate with Two Undulating Side Fins

Computation for the fin geometries similar to that of experiment was conducted for comparisons. However, in the computation, at first, the model was approximated as rectangular flat plate for simplicity in grid generation. The model sketch and coordinate system are shown in Fig. 2.3. The body is symmetric with respect to  $x$ -axis, so only half of the body (shaded region) was simulated to save computational cost. The widths of the resistance body and the fin are denoted by  $b$  and  $bm$  respectively. Also  $u$ ,  $v$  and  $w$  are the velocity components in  $x$ ,  $y$  and  $z$  directions respectively.

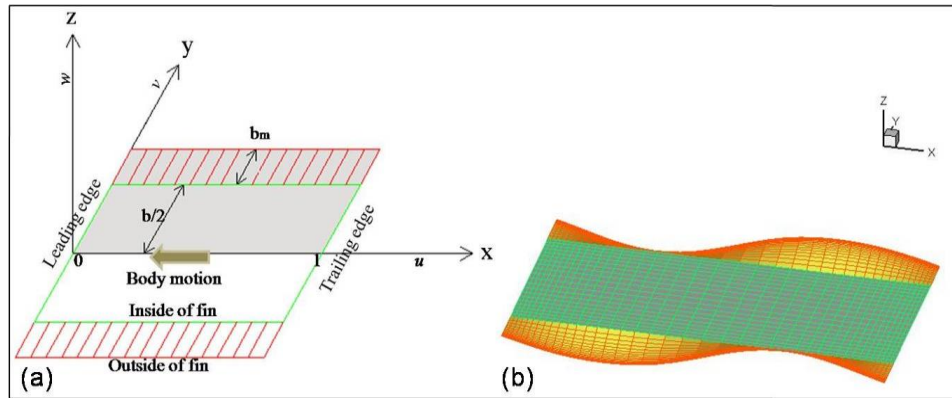


**Fig. 2.3 (a) Simple model sketch and coordinate system; (b) Computational Model with undulating side fin**

At first, the numerical grid was constructed around a rectangular flat plate of same area of the robot (including fin). Then two fins were produced at the lateral sides of the flat plate by gradually increasing the vertical amplitude using Eq. 2.1 to Eq. 2.3.

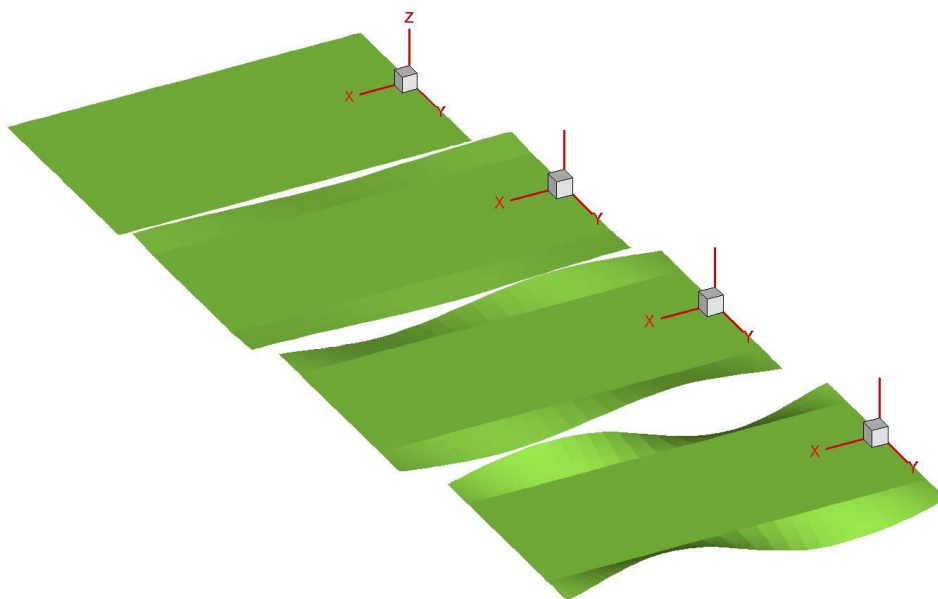


**Fig. 2.4 Formation of fin at the sides of the flat plate**

All variables were nondimensionalized using resistance body length ( $L$ ), advanced speed ( $U$ ), density ( $\rho$ ) and their combinations. So, the nondimensional body length and the advanced speed were 1. In

this case, the formation of the fin from flat plate was done in the first period, which is shown in Fig. 2.4. In other periods, full amplitude of fin was used and also they are symmetric. The time history of fin angle in  $x$ -direction  $\theta(x,t)$  was expressed as follows:

$$\theta = \theta_m \sin(2\pi nt - 2\pi x) \quad (2.1)$$

$$\theta_m = \arcsin \left[ \left\{ 1 - 0.905(x-0.5)^2 \right\} \sin \Theta \right] * I \quad (2.2)$$

$$I = \frac{1}{2} - \frac{1}{2} \cos \left( \frac{t}{T_{ini}} \right) \pi; \quad \text{where, } 0 \leq t \leq T_{ini}; \quad t \geq T_{ini}, I = 1 \quad (2.3)$$

where,

$\theta$  : the deflection angle from flat plate ( $0 < x < 1$ )

$\theta_m$  : angle amplitude ( $0 < x < 1$ )

$n$  : frequency

$t$  : time

$T_{ini}$  : initial period

$x$  : the distance along fin from leading edge

$\Theta$  : the maximum fin angle from the flat position

As mentioned above  $n$ ,  $t$  and  $x$  are all dimensionless. The dimensional value of  $n$  is  $N$  and  $n=NL/U$ .

A moving grid was constructed around the body to handle the unsteady motion. The numerical grid was generated around half of the body at each time step using Poisson equation. At the first period, undulating side fins were produced at the lateral sides of the flat plate by gradually increasing its amplitude, while the other periods were kept symmetric. The grid independency was confirmed by checking different number of grids. Finally, the computational domain and the number of grids for half domain written in the Table 2.2 were chosen. The full grid at one time step is shown in Fig. 2.5a, also the enlarged view near the fin is shown in Fig. 2.5b. The body was covered by 41 and 16 grid points in  $x$  and  $y$  directions respectively. The minimum grid spacing was 0.0015 in the  $y$  and  $z$  direction.

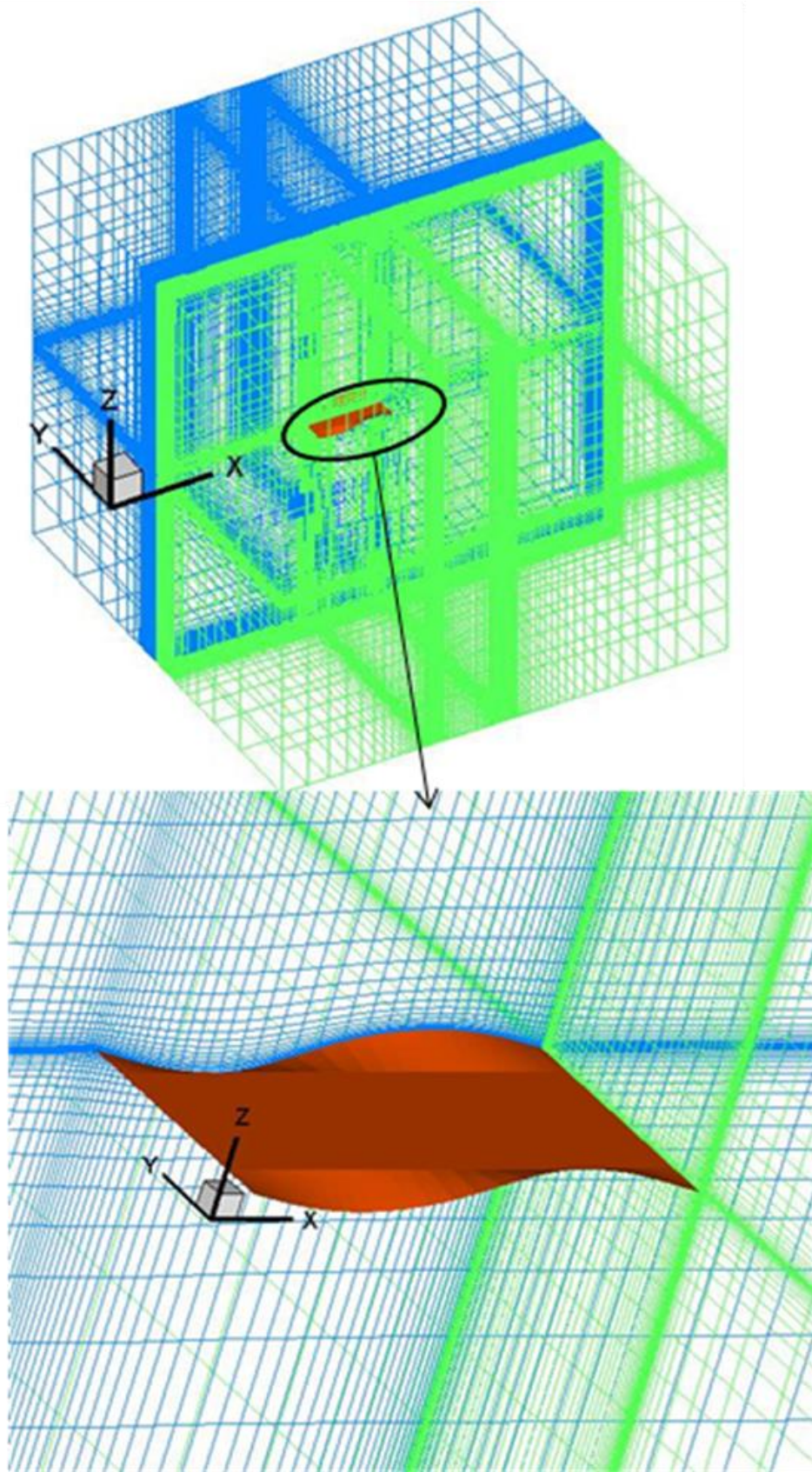


**Fig. 2.5: (a) Full Computational grid of one time step (b) Enlarged view near the fin**

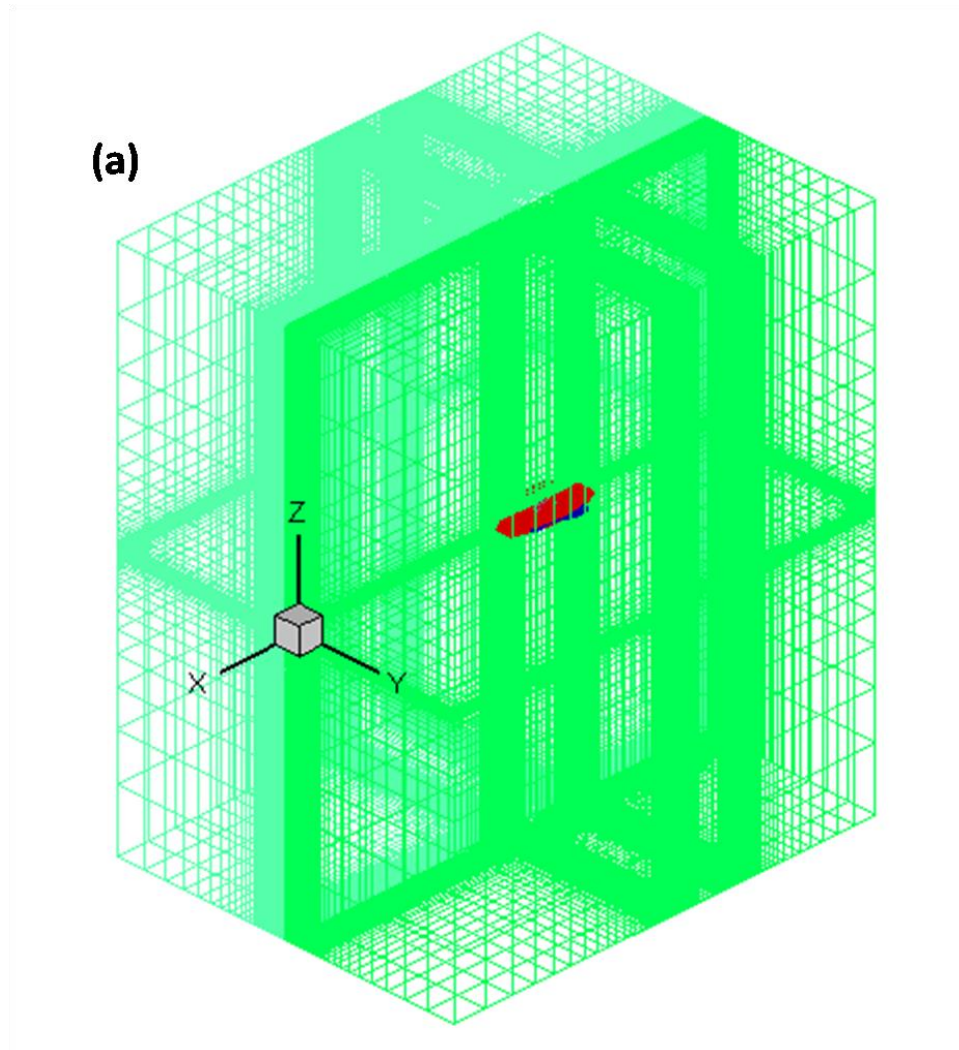
**Table 2.2. Computational domain and grid points for half domain**

Axis	Computational domain	Number of grid points
$x$	-1 ~ 4	90
$y$	0 ~ 3	40
$z$	-3 ~ 3	51

### **2.3.3.2 Grid on the Real Model-4**

A body-fitted moving grid was generated around a body similar to Model-4 of the Squid-robot. The coordinate system and the strategy of generating the grid are similar to that discussed in the previous section; however in this case, special concentration was given due to thick resistance body and thin undulating side fin. In the previous grid the body was considered as rectangular flat plate and the body length and fin length was same. In the present case, the side of the body is little curved and the body is little asymmetric with respect to  $xy$  plane. Also the fin length is smaller than the length of the body. The body is symmetric with respect to  $x$ -axis, so in this case also only half portion of the grid was created; the other portion can be found by applying mirror. The grids were generated in three steps for convenience in flow field computation. First, the grid was created around the body keeping the fin as flat position; second, the amplitude of the fin was gradually increased using the Eq. 2.1 - 2.3 to make the undulation; finally, the grid with full amplitude of undulation was created. In second and third cases, 40 grids were created in 40 time steps in one period and the periods are symmetric for the latter case. The aspect ratio of the side fin was 0.09 as the real Model-4; the maximum fin angle was considered as 30 degree and 45 degree for keeping consistence with the experiment. The smoothness of the numerical grid was maintained by using Poisson equation at each time step. Moreover, concentration factors were applied at both sides (body side and outer side) of the fin for making smooth grid. Fig. 2.6 shows the computational grid of one time step; where (a) is the full grid, (b) is enlarged view near the body and (c) is the grid on the body.

The grid independency was also confirmed by checking different number of grids; finally the best possible grid was chosen. The body was covered by 74 and 16 grid points and fin was enclosed by 34 and 10 grid points in  $x$  and  $y$  directions respectively. The computational domain and the number of grids for half domain are shown in Table 2.3.



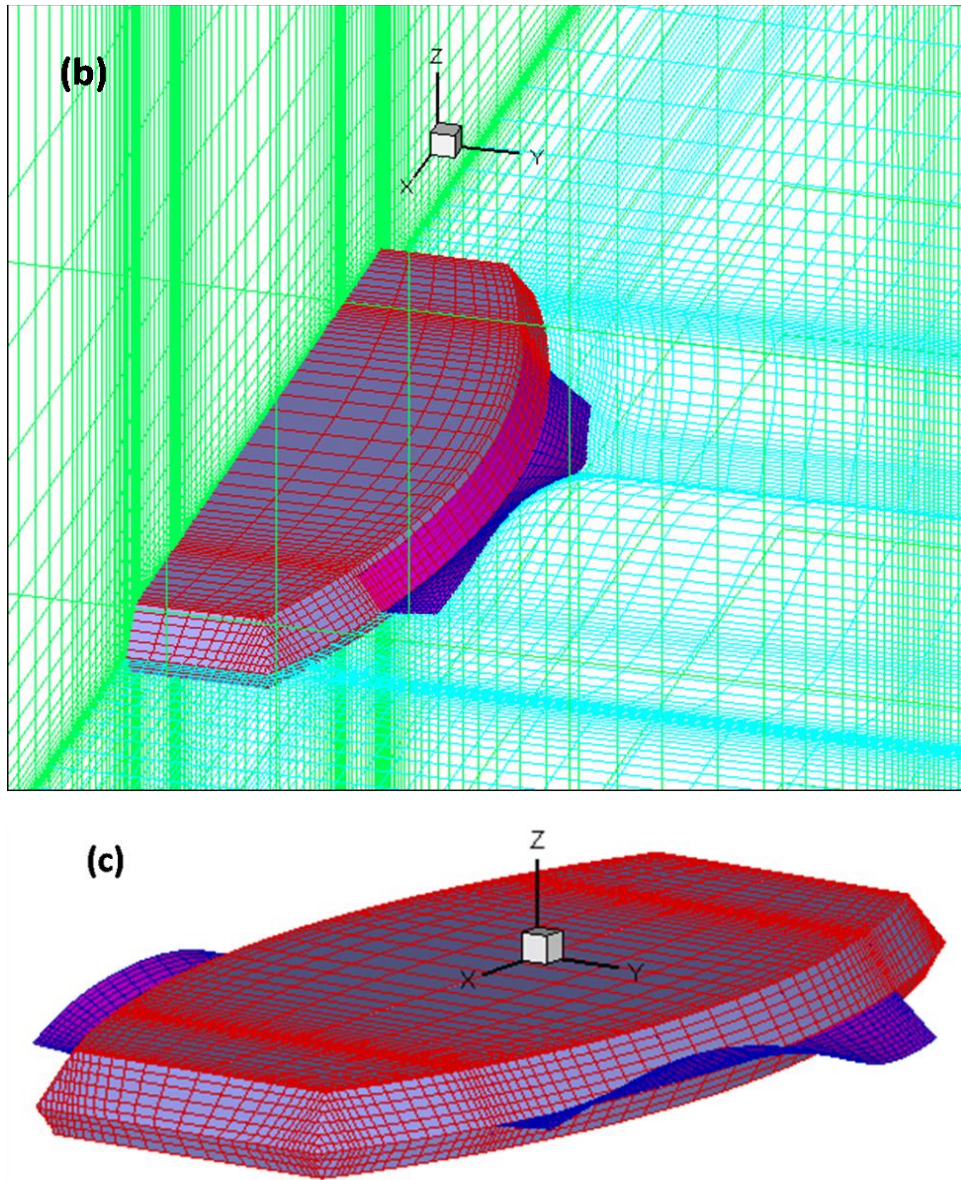


**Fig. 2.6** Computational grid around Model-4 (a) Full grid, (b) Enlarged view (half) near the body, (c) Body grid

**Table 2.3.** Computational domain and number of grids for half domain around Model-4

Axis	Computational domain	Number of grid points
$x$	-2 ~ 3	126
$y$	0 ~ 2	50
$z$	-3 ~ 3	50

*The minimum grid spacing was 0.005 in  $x$  direction and 0.0015 in  $y$  and  $z$  direction.*

### 2.3.4 CFD Computation

The Navier-Stokes equations and continuity equation were solved numerically. For the computation around a moving body, the equations were transformed to moving general curvilinear coordinate. The unsteady three-dimensional Navier Stokes and continuity equations for an incompressible fluid in Cartesian coordinate can be written as follows (Eq. 2.4~2.7):

$$\frac{\partial u}{\partial t} + u \frac{\partial u}{\partial x} + v \frac{\partial u}{\partial y} + w \frac{\partial u}{\partial z} = -\frac{\partial p}{\partial x} + \frac{1}{R_n} \left( \frac{\partial^2 u}{\partial x^2} + \frac{\partial^2 u}{\partial y^2} + \frac{\partial^2 u}{\partial z^2} \right) \quad (2.4)$$

$$\frac{\partial v}{\partial t} + u \frac{\partial v}{\partial x} + v \frac{\partial v}{\partial y} + w \frac{\partial v}{\partial z} = -\frac{\partial p}{\partial y} + \frac{1}{R_n} \left( \frac{\partial^2 v}{\partial x^2} + \frac{\partial^2 v}{\partial y^2} + \frac{\partial^2 v}{\partial z^2} \right) \quad (2.5)$$

$$\frac{\partial w}{\partial t} + u \frac{\partial w}{\partial x} + v \frac{\partial w}{\partial y} + w \frac{\partial w}{\partial z} = -\frac{\partial p}{\partial z} + \frac{1}{R_n} \left( \frac{\partial^2 w}{\partial x^2} + \frac{\partial^2 w}{\partial y^2} + \frac{\partial^2 w}{\partial z^2} \right) \quad (2.6)$$

$$\frac{\partial u}{\partial x} + \frac{\partial v}{\partial y} + \frac{\partial w}{\partial z} = 0 \quad (2.7)$$

The equations were transformed from the physical domain in Cartesian coordinates  $(x, y, z, t)$  into the computational domain in non-orthogonal curvilinear coordinates  $(\xi, \eta, \zeta, \tau)$ . A partial transformation was used in which only the independent variables were transformed, leaving the velocity components  $u_i$  in Cartesian coordinates. Using the transformed relations the momentum (Eq. 2.4~2.6) equations were written in general form:

$$g^{11} \phi_{\xi\xi} + g^{22} \phi_{\eta\eta} + g^{33} \phi_{\zeta\zeta} = A \phi_{\xi} + B \phi_{\eta} + C \phi_{\zeta} + D \phi_{\tau} + S_{\phi} \quad (2.8)$$

Here,  $\phi$  was represented by the velocity component  $u, v, w$ .

The coefficients were

$$A = \frac{R_n}{J} \left( b_1^1 (u - x_{\tau}) + b_2^1 (v - y_{\tau}) + b_3^1 (w - z_{\tau}) \right) - f^1 \quad (2.9)$$

$$B = \frac{R_n}{J} (b_1^2(u - x_\tau) + b_2^2(v - y_\tau) + b_3^2(w - z_\tau)) - f^2 \quad (2.10)$$

$$C = \frac{R_n}{J} (b_1^3(u - x_\tau) + b_2^3(v - y_\tau) + b_3^3(w - z_\tau)) - f^3 \quad (2.11)$$

$$D = R_n \quad (2.12)$$

Where,  $x_\tau, y_\tau, z_\tau$  are the grid velocities along  $x, y, z$  directions respectively. Also,

$$f^1 = \frac{1}{J} \left\{ \frac{\partial}{\partial \xi} (Jg^{11}) + \frac{\partial}{\partial \eta} (Jg^{21}) + \frac{\partial}{\partial \zeta} (Jg^{31}) \right\} \quad (2.13)$$

$$f^2 = \frac{1}{J} \left\{ \frac{\partial}{\partial \xi} (Jg^{12}) + \frac{\partial}{\partial \eta} (Jg^{22}) + \frac{\partial}{\partial \zeta} (Jg^{32}) \right\} \quad (2.14)$$

$$f^3 = \frac{1}{J} \left\{ \frac{\partial}{\partial \xi} (Jg^{13}) + \frac{\partial}{\partial \eta} (Jg^{23}) + \frac{\partial}{\partial \zeta} (Jg^{33}) \right\} \quad (2.15)$$

$$J(\text{Jacobian}) = x_\xi (y_\eta z_\zeta - y_\zeta z_\eta) + x_\eta (y_\zeta z_\xi - y_\xi z_\zeta) + x_\zeta (y_\xi z_\eta - y_\eta z_\xi) \quad (2.16)$$

$$S_\phi = \frac{R}{J} \left( b_j^1 \frac{\partial p}{\partial \xi} + b_j^2 \frac{\partial p}{\partial \eta} + b_j^3 \frac{\partial p}{\partial \zeta} \right) - 2(g^{12} \phi_{\xi\eta} + g^{13} \phi_{\xi\zeta} + g^{23} \phi_{\eta\zeta}) \quad (2.17)$$

(where,  $j=1, 2, 3$ )

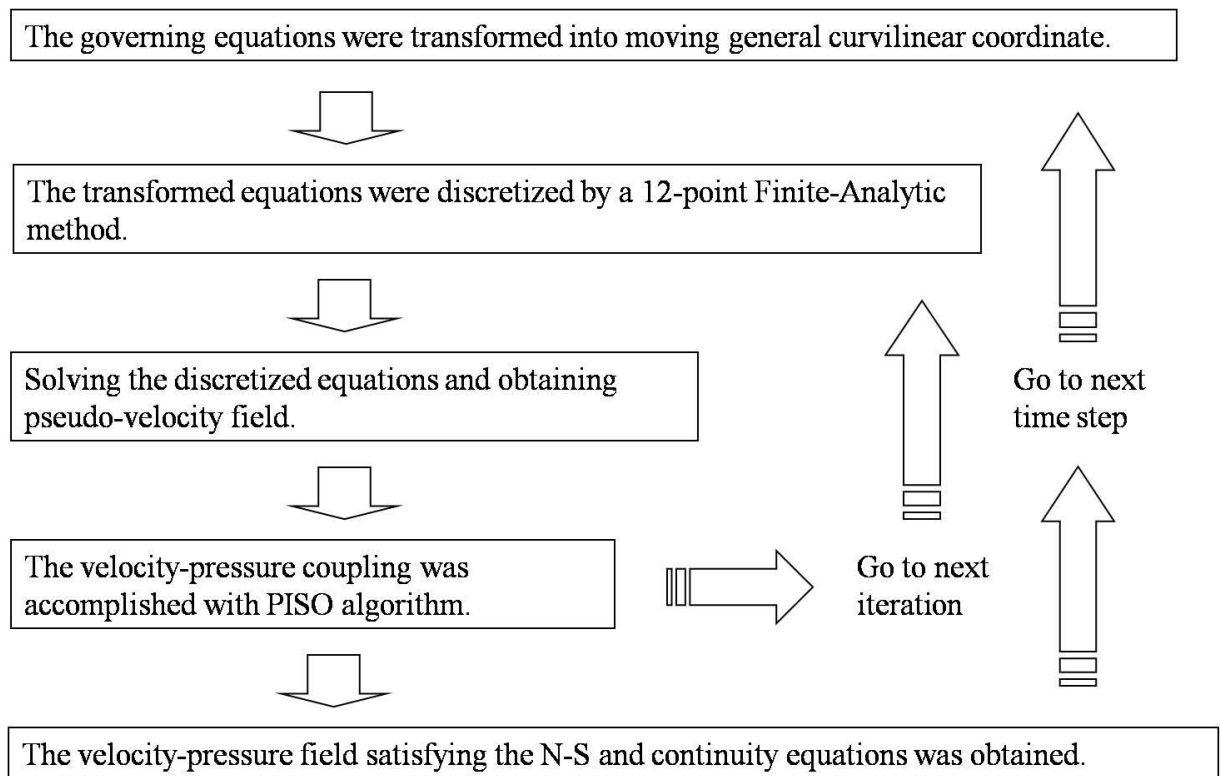
The element  $b_j^i$  and  $g^{ij}$  were found from the equation (2.18~2.19)

$$\begin{bmatrix} b_1^1 & b_2^1 & b_3^1 \\ b_1^2 & b_2^2 & b_3^2 \\ b_1^3 & b_2^3 & b_3^3 \end{bmatrix} = \begin{bmatrix} y_\eta z_\zeta - y_\zeta z_\eta & z_\eta x_\zeta - z_\zeta x_\eta & x_\eta y_\zeta - x_\zeta y_\eta \\ y_\zeta z_\xi - y_\xi z_\zeta & z_\zeta x_\xi - z_\xi x_\zeta & x_\zeta y_\xi - x_\xi y_\zeta \\ y_\xi z_\eta - y_\eta z_\xi & z_\xi x_\eta - z_\eta x_\xi & x_\xi y_\eta - x_\eta y_\xi \end{bmatrix} \quad (2.18)$$

$$\begin{bmatrix} g^{11} & g^{12} & g^{13} \\ g^{21} & g^{22} & g^{23} \\ g^{31} & g^{32} & g^{33} \end{bmatrix} = \frac{1}{J^2} \begin{bmatrix} \mathbf{b}^1 \cdot \mathbf{b}^1 & \mathbf{b}^1 \cdot \mathbf{b}^2 & \mathbf{b}^1 \cdot \mathbf{b}^3 \\ \mathbf{b}^2 \cdot \mathbf{b}^1 & \mathbf{b}^2 \cdot \mathbf{b}^2 & \mathbf{b}^2 \cdot \mathbf{b}^3 \\ \mathbf{b}^3 \cdot \mathbf{b}^1 & \mathbf{b}^3 \cdot \mathbf{b}^2 & \mathbf{b}^3 \cdot \mathbf{b}^3 \end{bmatrix} \quad (2.19)$$

The transformed equation (2.8) was discretized by the 12- point Finite-Analytic method in space (Chen et al. 1984 and Tahara 1993). Euler implicit scheme were used for time discretization along with the PISO algorithm for velocity pressure coupling. For one time step computation, sufficient iterations were repeated to get a time-accurate solution. In every internal iteration the finite analytic coefficients were updated for retaining the nonlinear nature of the Navier-Stokes equations. The laminar flow computation was carried out at  $Re = 10,000$ . The total CFD computation is shown in the following flowchart:

### CFD Method Flowchart



#### 2.3.5 Boundary Conditions

The boundary conditions of the computation were as follows:

On inlet:  $u = 1$  ,  $v = w = p = 0$

On upper & lower side (i.e.,  $z = +/-3$ ):  $u = 1, v = 0$

On lateral side (i.e.,  $y = +3$ ):  $u = 1, w = 0$

On outer boundary:  $\frac{\partial u}{\partial x} = \frac{\partial v}{\partial x} = \frac{\partial w}{\partial x} = \frac{\partial p}{\partial x} = 0$

On Body surface:  $v = \frac{\partial y_b}{\partial \tau}, w = \frac{\partial z_b}{\partial \tau}$

On the symmetry plane (i.e.,  $y = 0$ ):  $\frac{\partial u}{\partial y} = v = \frac{\partial w}{\partial y} = \frac{\partial p}{\partial y} = 0$

## 2.4 Computational Results of Flat Body with Side Fin

### 2.4.1 Forces

The computation was first conducted around the flat plate having similar area of the model in order to validate the codes used for numerical study. In the simulation, the velocity of the flow was gradually accelerated from 0 to 1 and then kept at steady. The computational frictional force of flat plate agreed well with the well-known Blasius solution ( $B/L \times 0.01328$ ) in the steady state region (Fig. 2.7).

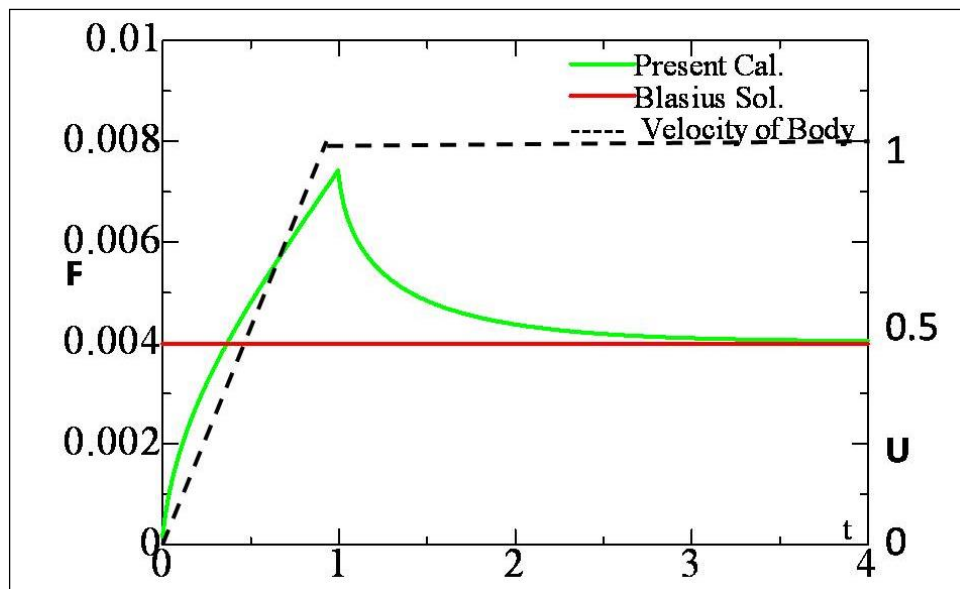
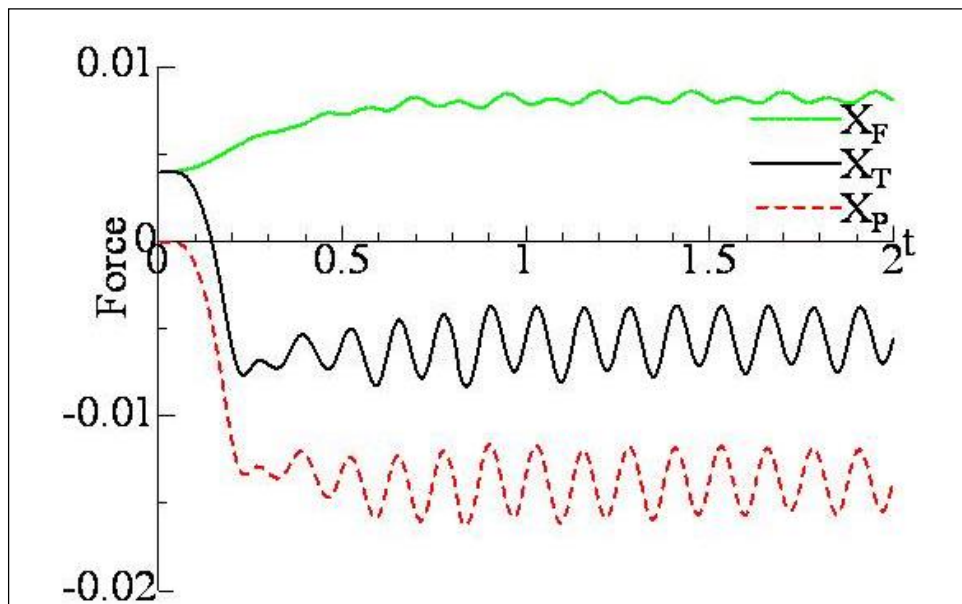


Fig. 2.7 Frictional force for a flat plate in acceleration stage and constant velocity stage

The hydrodynamic forces produced by different fins for which computation was conducted at different aspect ratios ( $AR = \text{width/length}$ ) and fin angles for different frequencies were analyzed. Sufficient convergence was censured by taking adequate iteration in all the cases. The time history of  $x$ -directional forces at aspect ratio ( $AR$ ) of 0.1, frequency ( $n$ ) of 4 and the maximum fin angle of  $30^\circ$  was drawn (Fig. 2.8). In this figure,  $X_F$  and  $X_P$  are the force due to frictional stress and pressure respectively, and  $X_T$  is the total force. Note that, the force direction is positive  $x$ ; that means the positive and negative values show the resistance and thrust respectively. The forces are nondimensionalized by  $\rho U^2 L^2$ .



**Fig. 2.8 Time history of  $x$ -directional forces for  $AR = 0.1$ ,  $n = 4$  and  $\theta = 30^\circ$**

The robot we used to mimic the flat fishes with undulating side fins, which usually use the progressive wave based swimming mode. In this mode, to propel forward, the progressive wave must be faster than the uniform flow. In this kind of lift-based swimming mode, no recovery stroke is necessary because lift force is generated during the upstroke and downstroke of the fin. In this fashion,  $x$ ,  $y$  and  $z$  direction forces are produced during the movement of the undulating side fins (Fig. 2.9).

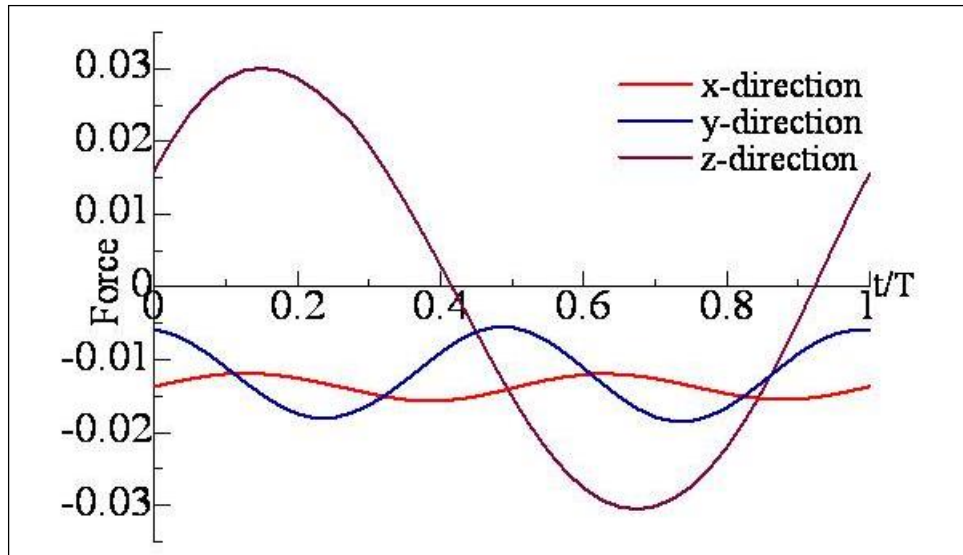


**Fig. 2.9**  $x$ ,  $y$  and  $z$  direction pressure forces produced by undulating side fin

The  $z$ -direction force is large but the body does not go up or down because of its flat shape. Also the mean of  $z$ -component force is zero. The  $y$ -component is also cancelled out due to the symmetrical movements of two side fins in opposite directions. So, only the  $x$ -direction force acts on the body. This figure also indicates two peaks in one period for the  $x$ -component force, which confirmed that the fin produces force in both upstroke and downstroke movements. The total forces for one period of aspect ratio 0.1 at different frequencies ( $n$ ) and maximum fin angles ( $\theta$ ), as shown in Fig. 2.10, reveals that, for  $\theta = 30^\circ$  and  $n = 3$ , the total force is very close to zero. This is in agreement with the experiment as the self propulsion frequency of the model is similar to this value.

The amount of thrust and the propulsive efficiency depend mostly upon the aspect ratio and maximum fin angle. High aspect ratio fins are more capable as they induce less drag per unit of lift or thrust produced. The effect of changes in aspect ratio and fin angle on the  $x$ -direction force were calculated for the same frequency ( $n = 4$ ) (Fig. 2.11). The thrust force dominated the frictional resistance of the body for  $AR = 0.1$  in case of  $\theta = 30^\circ$  and the similar value was found from  $AR = 0.075$  in case of  $\theta = 45^\circ$ .

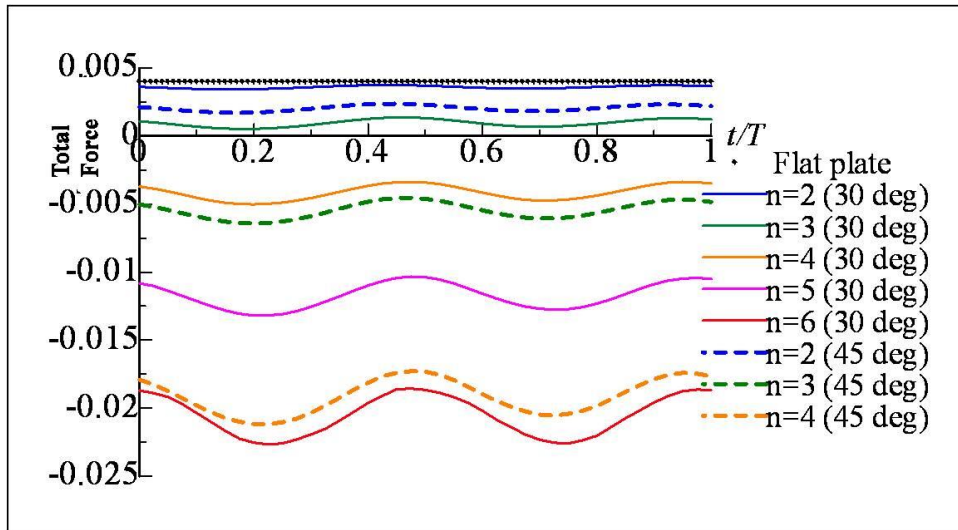


Fig. 2.10 Time history (one period) of the  $x$ -directional total force for  $AR = 0.1$  at different frequencies and maximum fin angles

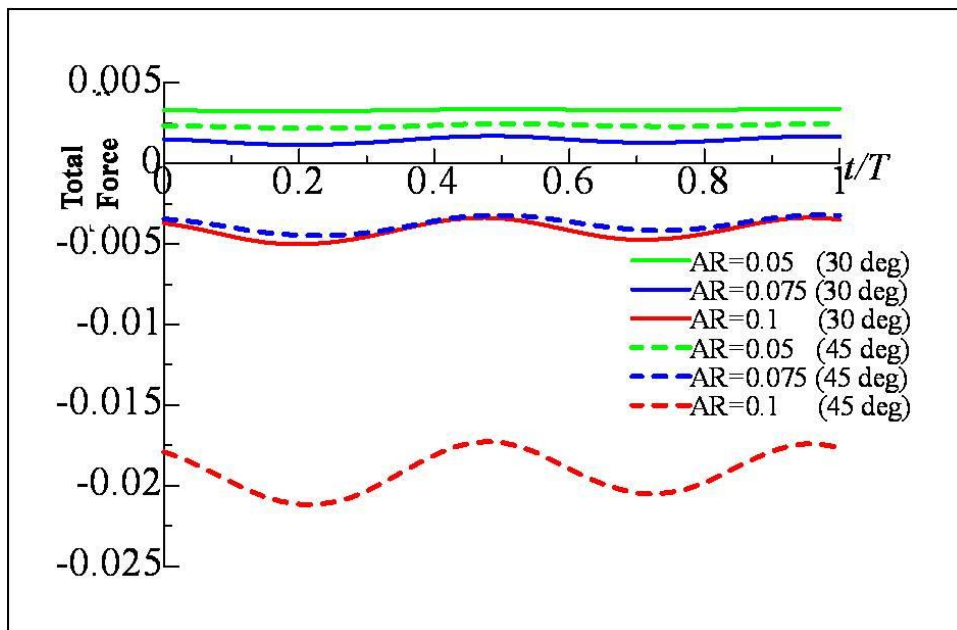
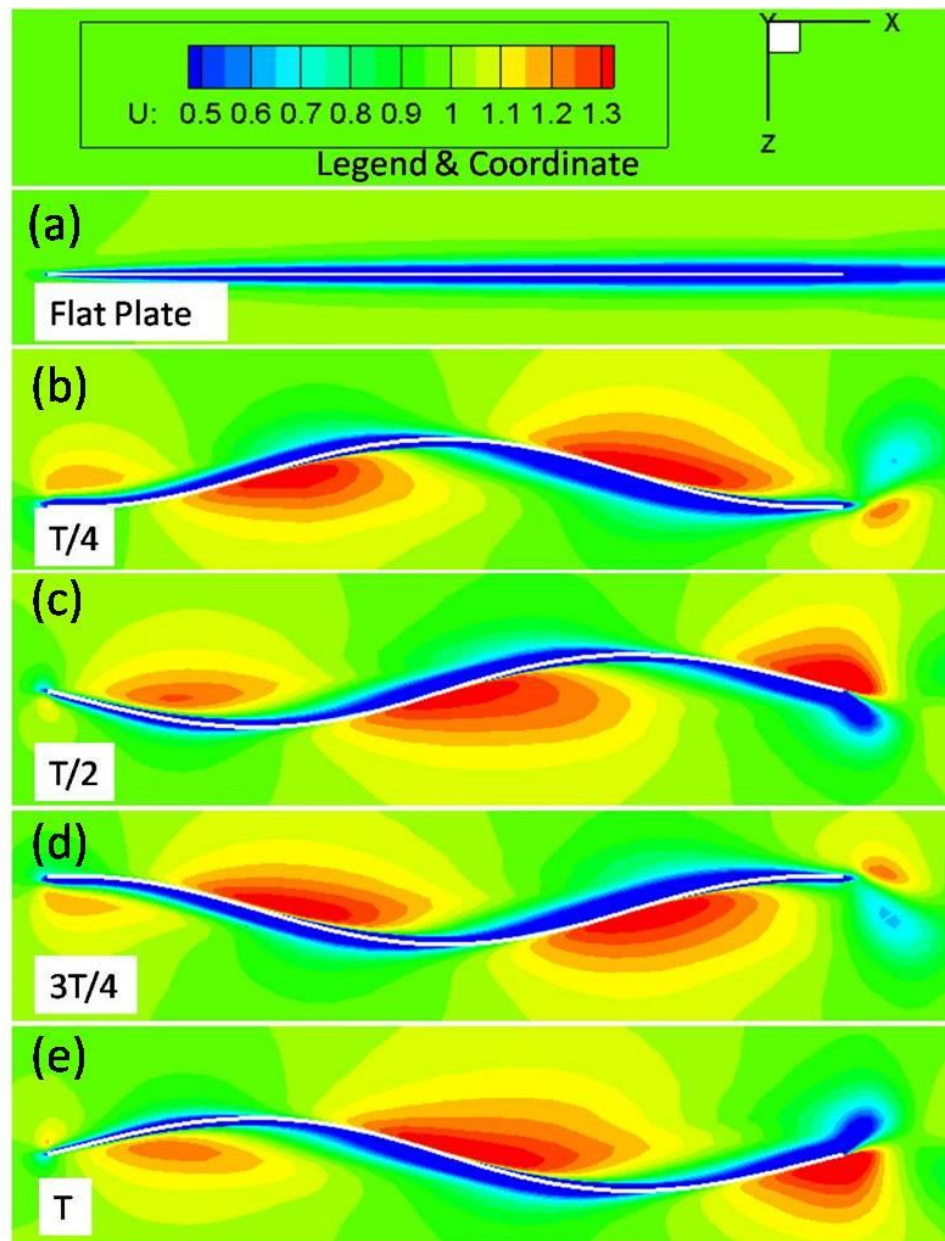


Fig. 2.11 Time history (one period) of the  $x$ -directional total force for  $n = 4$  at different aspect ratios and maximum fin angles

## 2.4.2 Contours

Different contours were drawn to visualize the surface distribution of forces and velocities. The contour of  $x$ -direction velocity distribution on a flat plate, as shown in Fig. 2.12a, shows the boundary layer very clearly around the flat plate.



**Fig. 2.12**  $u$ -velocity distribution on a flat plate and around a fin ( $AR = 0.1$ ,  $\theta = 30^\circ$ ) for  $n = 4$  at four time steps in one period

Figs. 2.12b to 2.12e also show the  $x$ -direction velocity distribution around the undulating side fins at different time steps in one period. From the figures, the velocity gradients at different positions of the fin are clearly visible. When the fin pushed the surrounding water during its movement, the velocity increased in that region. The undulations of the fins reduced the boundary layer, resulting in increase in velocity gradient and, hence, shear stress.

A vortex was formed at the edge of the fin which was clearly observed from  $yz$ -plane. The  $\omega_x$  distribution at the rear end of the fin at different time steps of similar period of previous figure was calculated (Fig. 2.13). The vortex distribution of the present time step was indicated by deep color where as the vortex shading of the previous time step was shown by the light color.

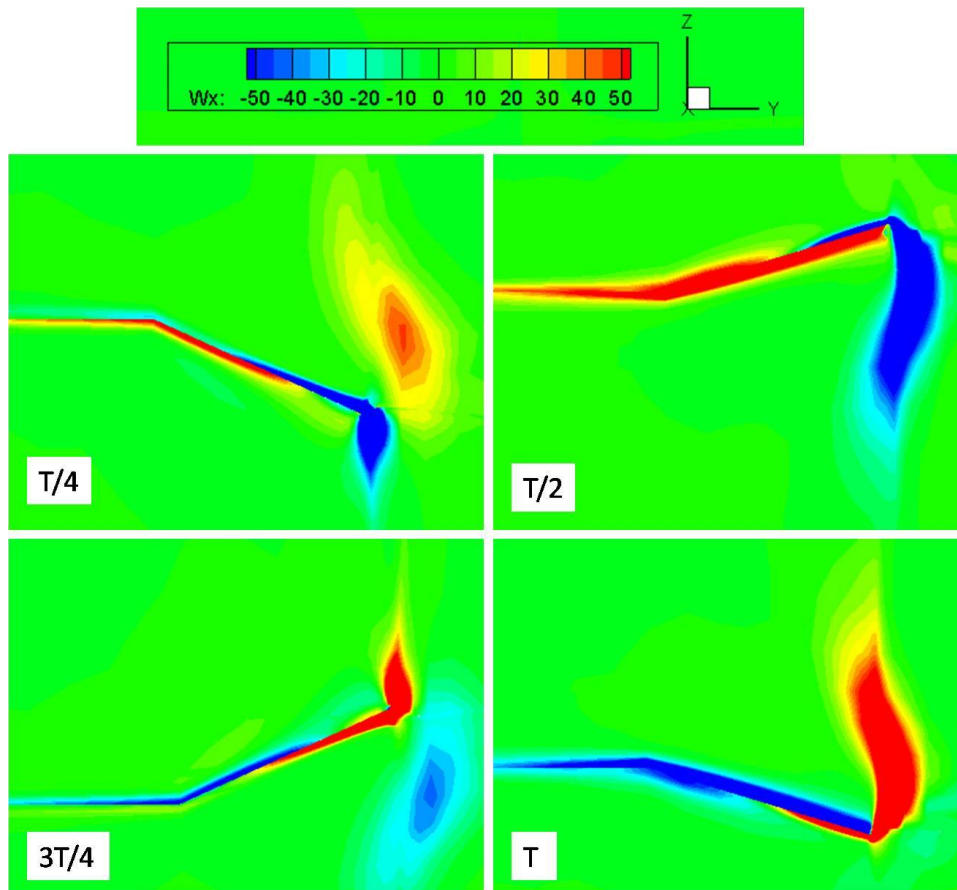


**Fig. 2.13:  $\omega_x$ -vorticity distribution at the rear end of a fin of AR = 0.1,  $n = 4$  and  $\theta = 30^\circ$  at four time steps in one period**

The contour of surface pressure distribution on the whole body of aspect ratio = 0.1 for different frequencies and fin angles were presented in Fig. 2.14. Fig. 2.14a shows the pressure distribution at frequency of 3 and maximum fin angle of  $30^\circ$ , whereas Fig. 2.14b shows the results of frequency = 6 for the same fin angle. Also, Fig. 2.14c shows the surface pressure distribution of the same frequency of Fig. 2.14a but for a different fin angle of  $45^\circ$ . The fin produced more pressure force with the increase of frequency and/or maximum fin angle that is observed by deeper color from these figures. The different pressure distribution of upper and lower surfaces is clearly observed in each case. The pressure of the lower surface became significant when the fin moved from up to down, and the corresponding upper surface had lower pressure at the same time and vice versa.

For better visualization of pressure difference between upper and lower surface of the undulating fin, we slice the fin parallel to  $xz$ -plane at  $y = 0.275$  (constant) (Fig.2.15a). The negative and positive pressure is seen in the upper and lower side of the same position of the fin during its undulations (Fig.2.15b). The prediction of pressure difference between two surfaces is important because it is the main reason behind the thrust force generation.

The thrust was computed by the product of pressure difference between upper and lower surfaces with the normal vectors in  $x$ -direction. The method of thrust calculation is shown in (Fig. 2.16). The pressure difference distribution and the thrust distribution on the body and the fin at four time steps (Fig. 2.17) reveal two important phenomena. Firstly, both for the negative and the positive pressure differences, the  $x$ -direction forces have maximum values. This confirms previous discussion on Fig. 2.5, which shows that the fin produces thrust during both of its upstroke and down stroke movements. Secondly, the pressure difference also exists on the body part, but the body could not produce thrust force because the normal vectors are zero here.

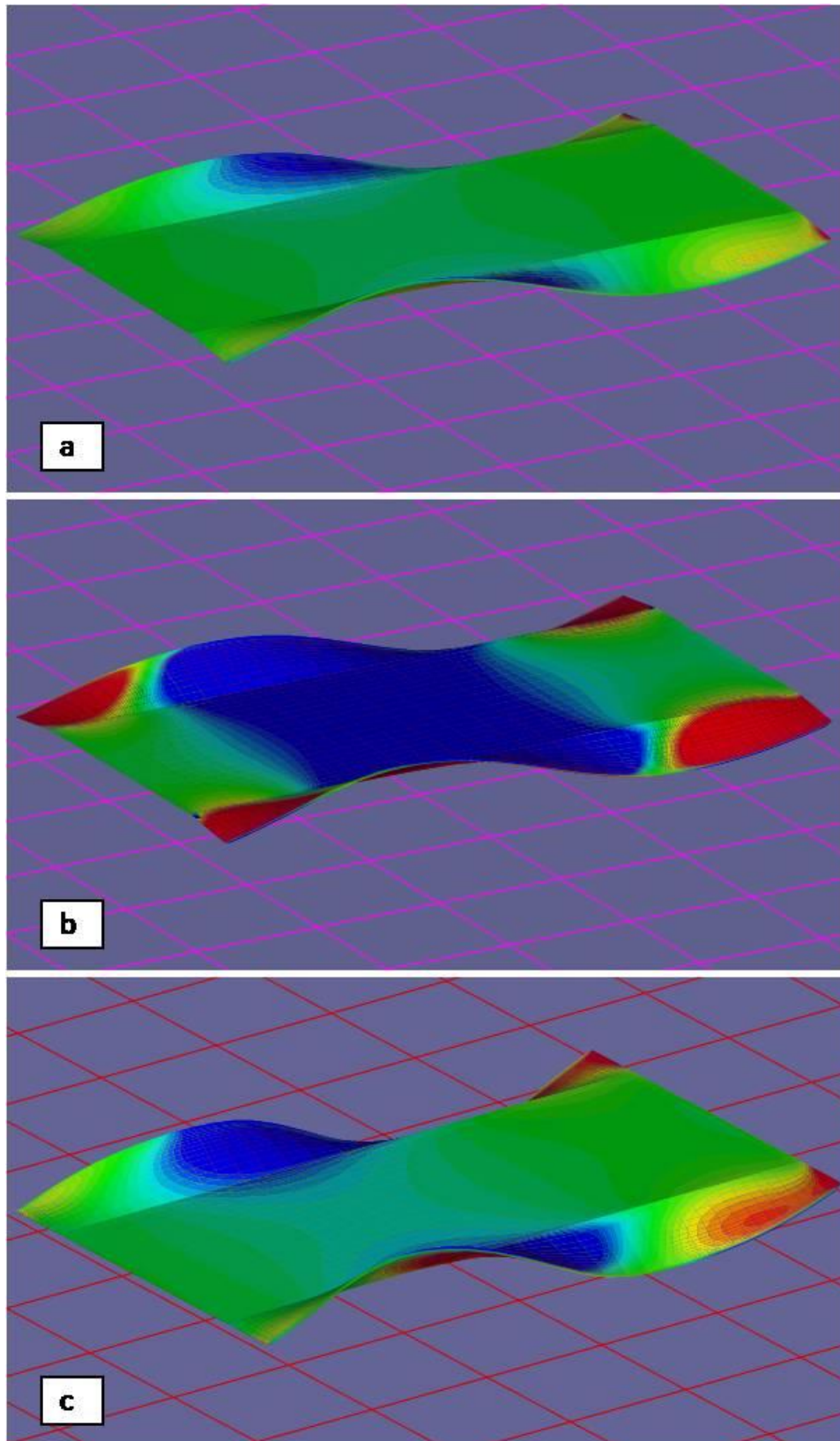


**Fig. 2.14: Pressure distribution on the upper and lower surface of the body and fins with  $AR = 0.1$  (a)  $n = 3$ ,  $\theta = 30^\circ$ ; (b)  $n = 6$ ,  $\theta = 30^\circ$  and (c)  $n = 3$ ,  $\theta = 45^\circ$**

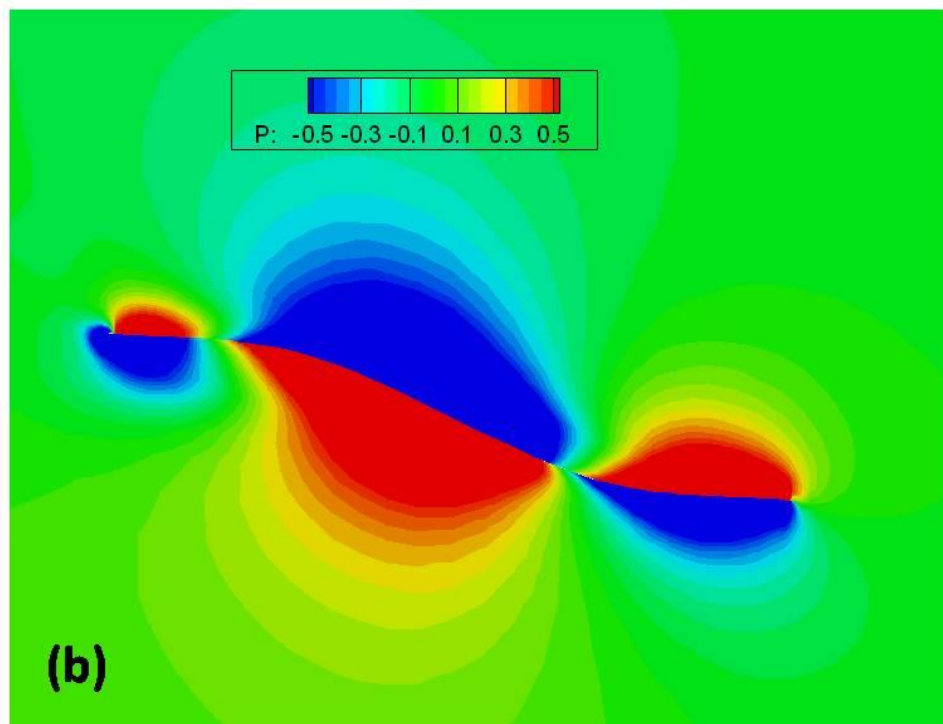
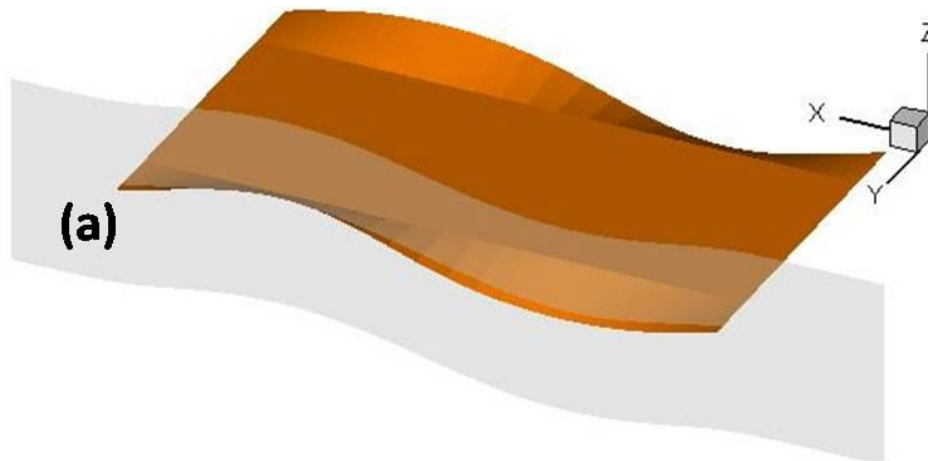


**Fig. 2.15: (a) Slicing position at  $y = 0.275$ ; (b) Pressure distribution on the upper and lower surfaces of the fin at  $y = 0.275$**

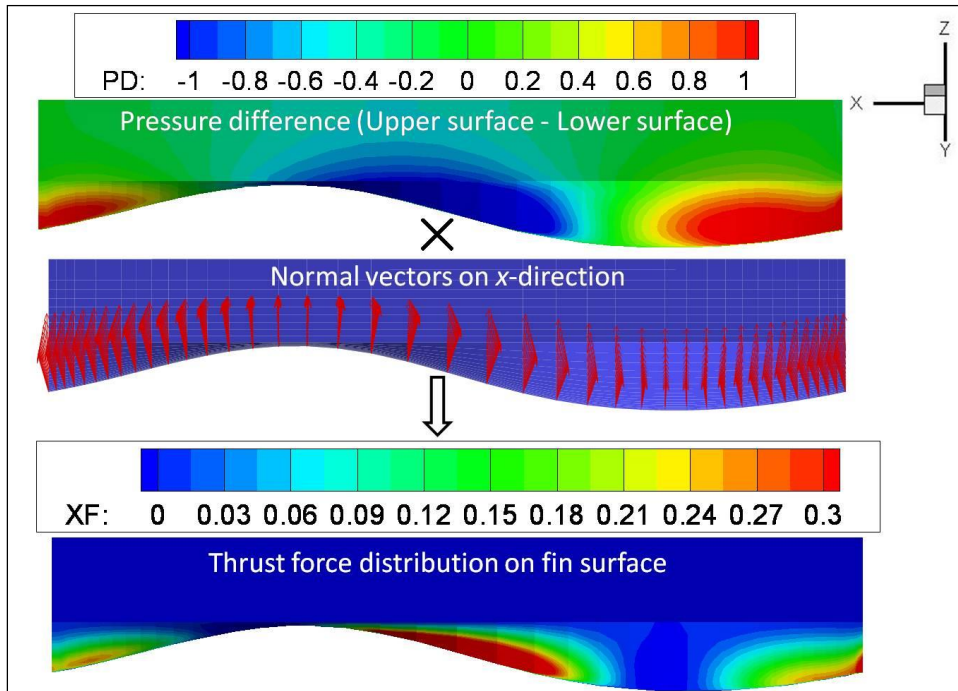


Fig. 2.16 The method of thrust calculation

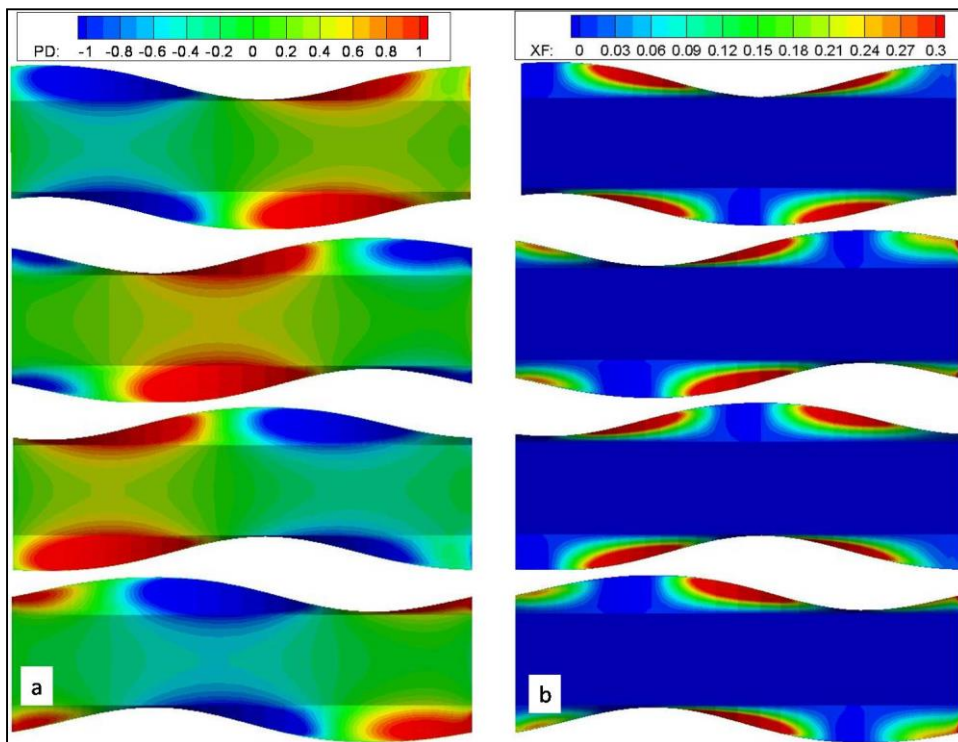


Fig. 2.17 (a) Distribution of pressure difference ( $p_{\text{upper}} - p_{\text{lower}}$ ); (b) Distribution of  $x$ -directional thrust force on the full body of  $AR = 0.1$ ,  $n = 4$  and  $\theta = 30^\circ$  at four time steps in one period

### 2.4.3 Fin Open Characteristics

The hydrodynamic force produced by the undulating side fins was computed to examine the relation between the thrust coefficient ( $K_x$ ) and advance coefficient ( $J$ ), similarly as in propeller chart. The thrust force ( $T_x$ ) was estimated by subtracting the flat plate resistance from the total  $x$ -directional force in the similar manner as the experiment. In the calculation an average value was taken from a conversed period. The thrust coefficient  $K_x$  in  $x$ -direction and advanced coefficient were computed as follows (Eq. 2.20-2.21).

$$K_x = \frac{T}{\rho n^2 L^4} = \frac{T}{\rho U^2 L^2} \times \frac{U^2}{n^2 L^2} = T_x \times J^2 \quad (2.20)$$

$$J = \frac{1}{n} \left( = \frac{U}{NL} \right) \quad (2.21)$$

- where,  $k_x$  : Thrust coefficient  
 $J_x$  : Advanced coefficient  
 $U$  : Advanced velocity  
 $L$  : Body length  
 $N$  : Dimensional frequency  
 $n$  : Non-dimensional frequency and  
 $T_x$  : Force produced by fin in  $x$ -direction (averaged)

The fin open characteristics or the fin performance chart for maximum fin angle of 30° and 45° for aspect ratios 0.05, 0.075 and 0.1 are shown in Fig. 2.18 and Fig. 2.19 respectively. Each graph apposed in the expected tendency with the change of aspect ratio and fin angle. It was also found that the thrust coefficient produced by fin at maximum angle of 45° is nearly twice compared to that of 30°.

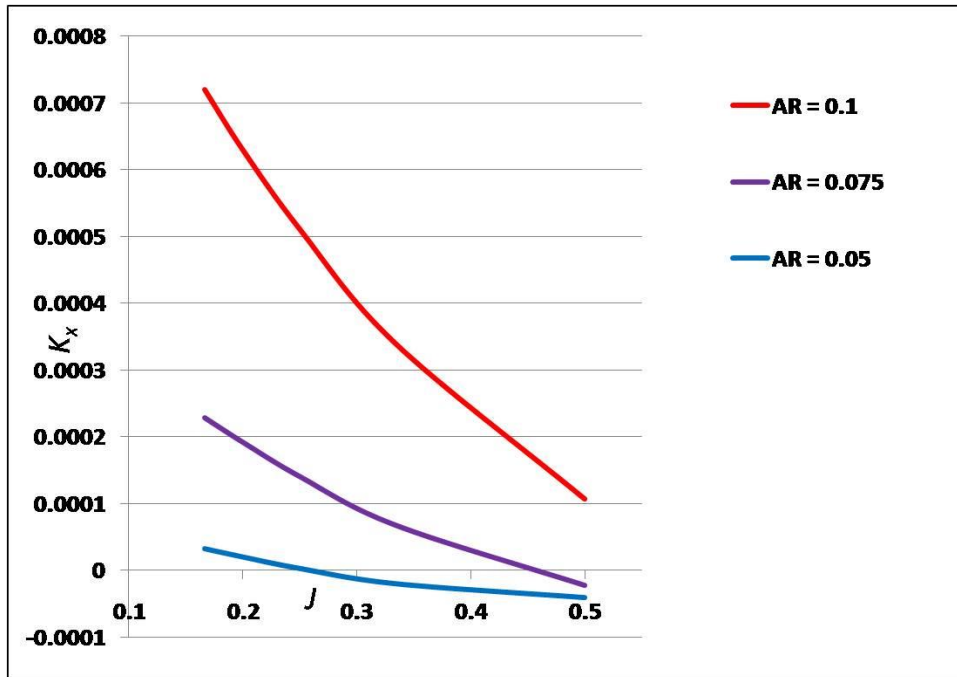


Fig. 2.18 Fin open characteristics,  $\theta = 30^\circ$

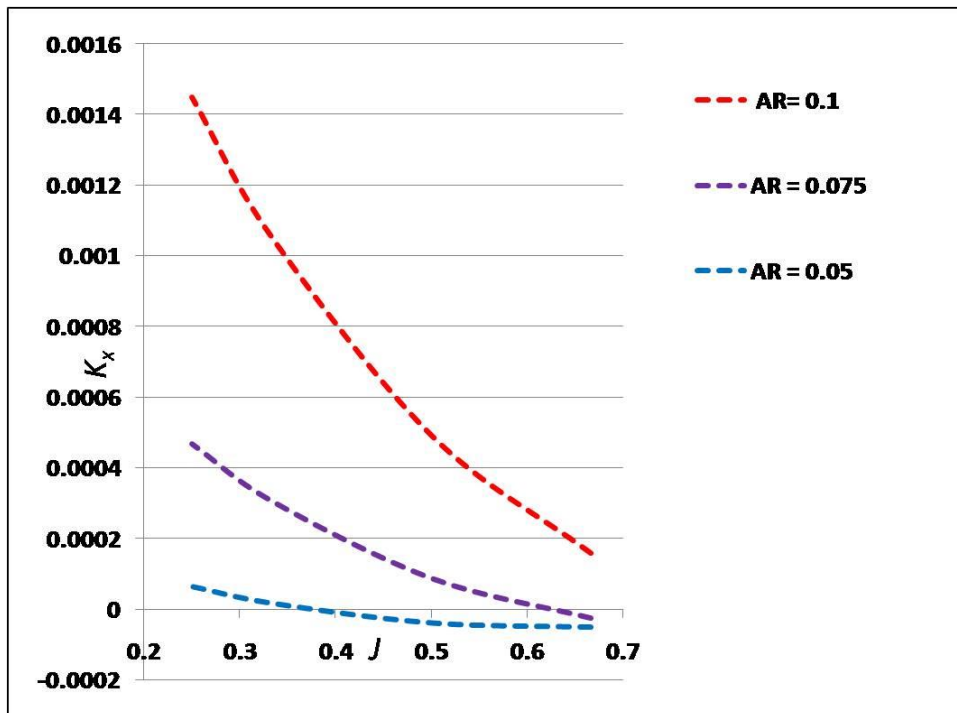


Fig. 2.19 Fin open characteristics,  $\theta = 45^\circ$

#### 2.4.4 Efficiency

The efficiency of propulsion ( $\eta$ ) is defined as the ratio of the useful power obtained,  $PE$ , to the power actually delivered to the propeller,  $PD$ , i.e.,  $\eta = PE / PD$ . In case of the model we studied, the delivered power or work ( $PD$ ) by the undulating side fins was the power yielded in  $y$  and  $z$  direction.  $PD$  was calculated by summing the products of the total force with the corresponding velocities. The obtained power ( $PE$ ) was the  $x$ -direction thrust force, as the velocity was one unit in this direction. Both the pressure force and the thrust, in accordance with our definition (total force-flat plate resistance, i.e. the  $TF-FPR$ ) were taken into consideration to analyze the trend of efficiency of our model (Fig. 2.20).

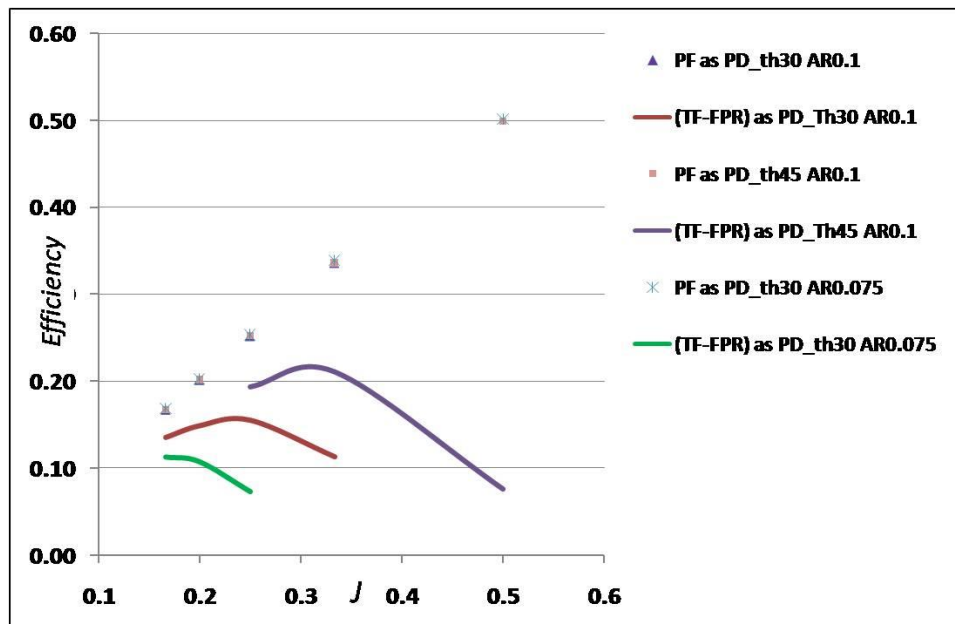


Fig. 2.20 Efficiency of the undulating side fin at different conditions

When only the pressure force was considered as the obtained power ( $PE$ ), the efficiency increases with the advance coefficient ( $J$ ), but when it accounted the frictional resistance, the efficiency drops down after certain value. This can be explained by the fact that with the increase in frequency, the frictional resistance also increases, which decreases the efficiency. The effect of changes in aspect

ratio and maximum fin angle on the efficiency of our squid-like robot was also estimated. Efficiency was not affected by the changes in aspect ratio and the maximum fin angle under the assumption that pressure force was the obtained power. In contrary, when the frictional resistance was included in the obtained power, the efficiency was affected both by changes in the aspect ratio and the maximum fin angle.

### 2.4.5 Verification

The relation among thrust coefficient, aspect ratio and fin angle was derived as follows (Eq. 2.22):

$$K_x = \Theta^2 \cdot \left(\frac{b_m}{L}\right)^3 \cdot \left(1 - \frac{U}{n\lambda}\right)^2 \cdot \int_0^1 \int_0^1 [4\pi^2 C_p b^2 \cos^2(2\pi k(s-ct))] \cdot dsdb \quad (2.22)$$

Where,  $c$  is the phase velocity of progressive wave and  $kc = n$ .

This equation indicates that the thrust coefficient is proportional to the cube of aspect ratio and square of maximum fin angle. These two relationships were established by the computation (Fig. 2.21). We know,  $(0.1/0.075)^3 = 2.37$ ; so in Fig. 2.21, if we divide the result of  $AR = 0.1$  by 2.37, we can obtain a curve very close to that  $AR = 0.075$ . In the similar manner, as  $(45/30)^2 = 2.25$ , the thrust generated by fin at maximum fin angle  $\theta = 45^\circ$  is about 2.25 times of that at  $30^\circ$  irrespective of fin's aspect ratio.

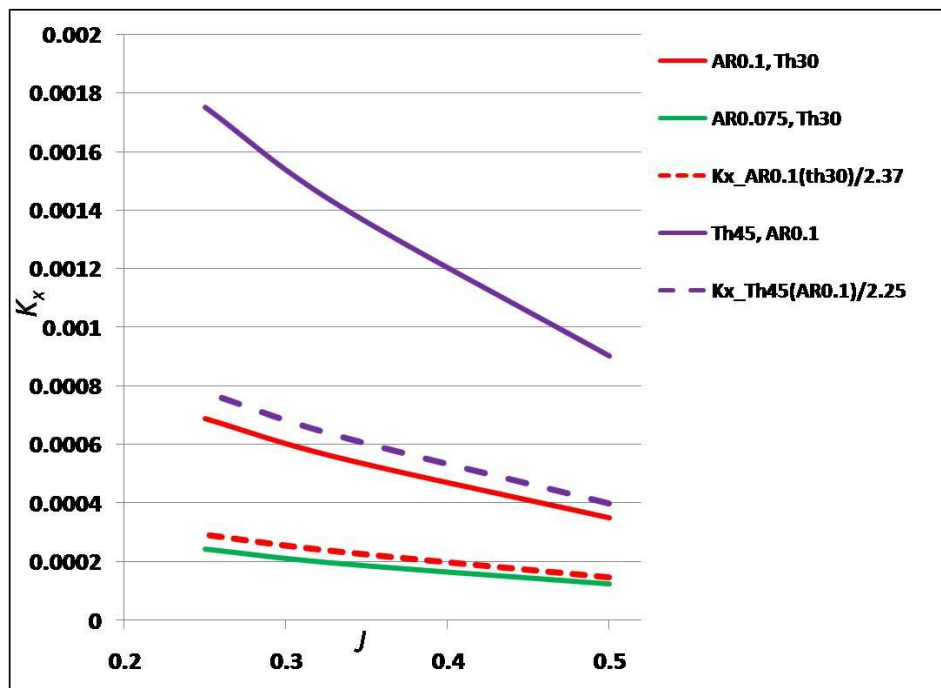


Fig. 2.21 The relation between  $k_x$  & AR and  $k_x$  &  $\theta$

### 2.4.6 Comparison

The computed and calculated results were compared with the experimental ones. The experimental results for the third and the fourth models with aspect ratios 0.136 and 0.09 are shown by dots and triangles, respectively in Fig. 2.22.

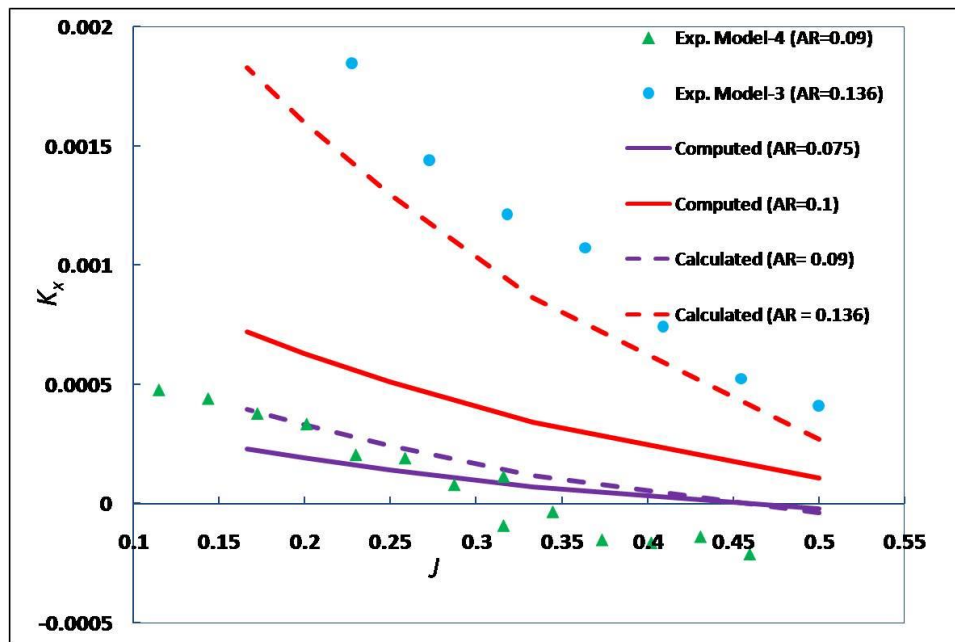


Fig. 2.22 Comparison among the computed, calculated and experimental results,  $\theta = 30^\circ$

The dot line and the solid line respectively show the computed results for  $AR = 0.075$  and  $0.1$ . As the aspect ratios of the computed and experimental models were different, for more comparison the results for  $AR$  similar to the experiments were calculated using the previous formula, as shown by dash and dash-dot lines. The calculated results show good agreement with the experimental results of corresponding aspect ratios. A little disparity was seen between the experiment and computed results at first sight. But, this was due to the dissimilarities of the models. The fin open characteristics for  $\theta = 45^\circ$  were also shown in Fig. 2.23. This result shows better conformity than that for  $\theta = 30^\circ$ . This was because the same area of the fin generated more pressure force when the maximum fin angle was

increased. This is also consistent with the previous discussion. Over all, the computed results approached the expected trend with the changes of the aspect ratio and maximum fin angle.

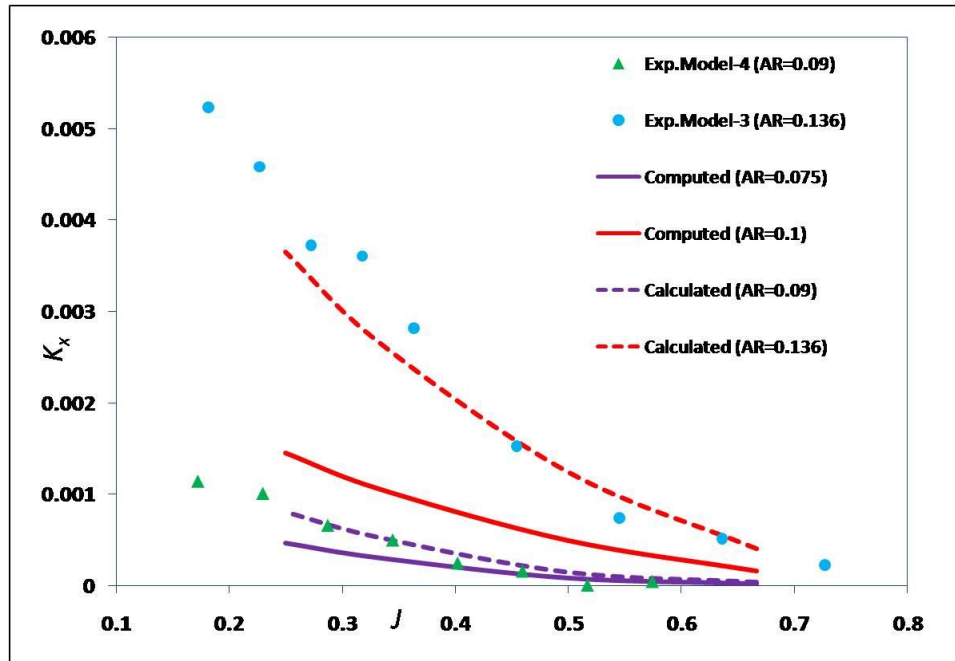


Fig. 2.23 Comparison among the computed, calculated and experimental results,  $\theta = 45^\circ$

## 2.5 Computational Results of Model-4

After verifying the CFD code for flat body with undulating side fins, the computation was extended for the real Model-4 of the Squid-robot. A numerical grid was generated on a body similar to the real Model-4; the detail of grid generation was discussed in the section 2.3.3.2. The discretization method for space and time was similar to that discussed in the previous sections, however a limiter was used to tackle the unexpected divergence of the computation. Some results of force calculation and the distribution of surface pressure, velocity and thrust force are shown and discussed in the following sections. The fin open characteristic was calculated and compared with the experiment and previous computation.

### 2.5.1 Forces

The hydrodynamic forces produced by undulating side fins were calculated at fin angle  $\theta = 30$  degree and  $\theta = 45$  degree for different frequencies. In this section, the results of non-dimensional frequencies  $n = 2.65, 3.18, 3.98, 5.3$  were discussed. The frequency was non-dimensionalized using body length  $L$ , and advance velocity  $U$ ; i.e.,  $n = NL/U$ , where  $N$  = dimensional frequency. It should be noted that the aspect ratio of the side fin of Model-4 is 0.09. Sufficient convergence was ensured in every case by running the computation for adequate iterations. Fig. 2.24 shows the total  $x$ -directional force ( $X_T$ ) produced by body with flat fin; for  $\theta = 30$ ,  $n = 3.18$  and for  $\theta = 45$ ,  $n = 3.98$  ( $\theta / Th$  stands for maximum fin of side fin angle). Sufficient convergence is seen in this figure. The computation was conducted in three steps: First, the computation was conducted for the flat fin (iteration 1-1000). Second, in one period (iteration 1000-1040), the vertical amplitude of fin was gradually increased from flat position to full undulation using the Eqs. 2.1. – 2.3. In this case the converged result of flat fin was used as initial condition.

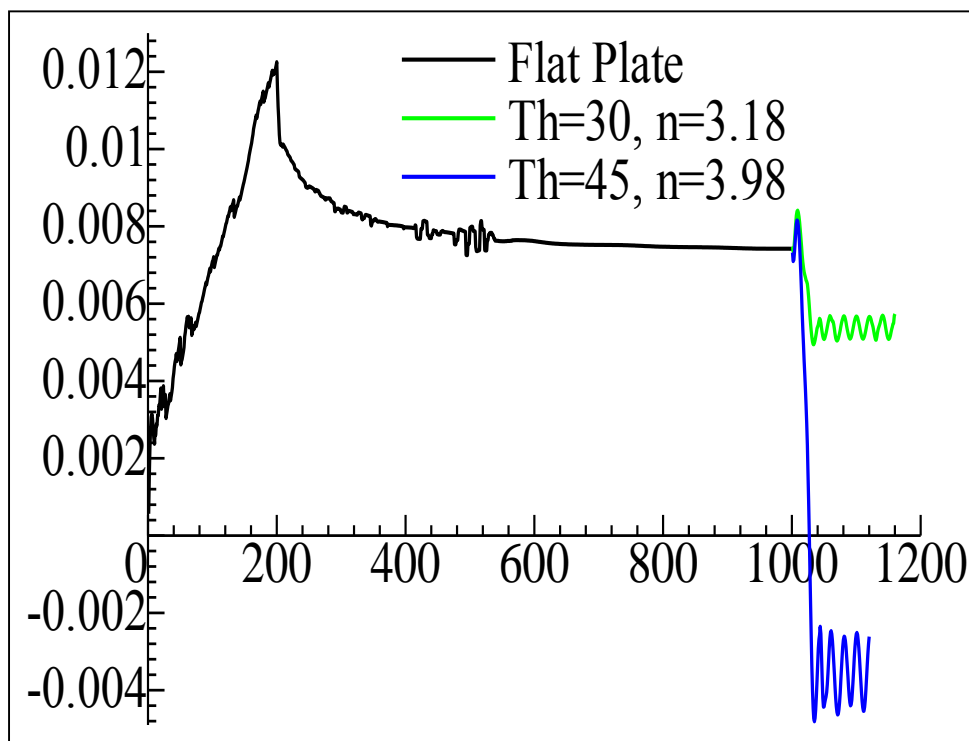
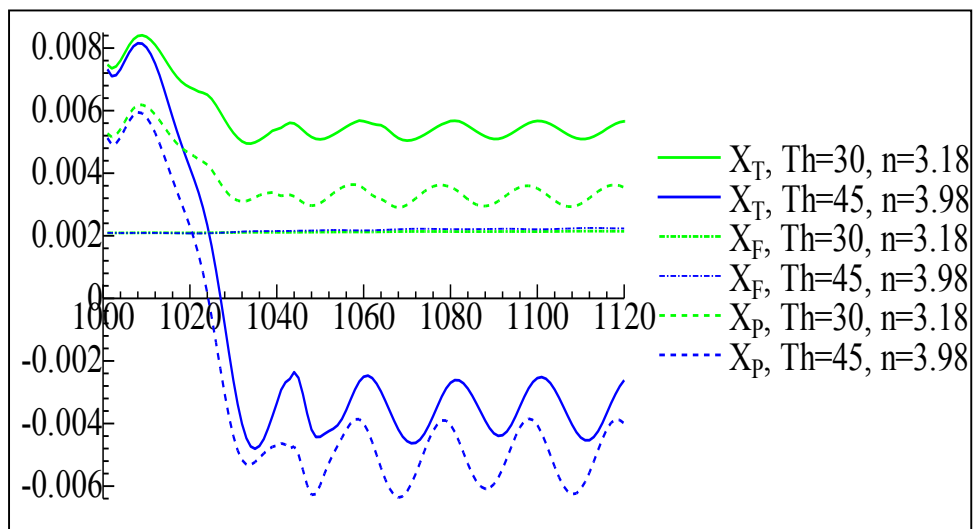


Fig. 2.24 Total  $x$ -directional force produced by body and fin

Finally, the computation was done for some preodic periods using the grid with full amplitude of fin to find the converted result. In this case the computation was conducted for three periodic periods (iteration 1040-1160). The total force ( $X_T$ ) can be found from the combination of frictional force ( $X_F$ ) and pressure force ( $X_P$ ) which is shown Fig. 2.25. In this figure the result of last two case (iteration 1000-1160), was only shown for clear observation.



**Fig. 2.25 Total force, frictional force and pressure force produced by body and fin**

It should be noted that, the positive direction indicates the resistance and negative direction indicates the thrust force. So, from this figure it is seen that the pressure force could overcome the frictional force and produced thrust in case of  $\theta = 45$ ,  $n = 3.98$ . In the graph of  $X_T$  and  $X_P$ , it is seen that the peaks are not exactly equal in lengths. This might be happened due the effect of the body; as the body is not fully symmetric w.r.to  $xy$  - plane.

The  $x$ -directional total force ( $X_T$ ) produced by body with undulating side fin including flat fin is shown in Fig. 2.26 for different frequencies and two fin angles; where the data of one converted period is only shown. From this figure it is seen that the thrust force produced by the fin is proportional to maximum fin angle and frequency.

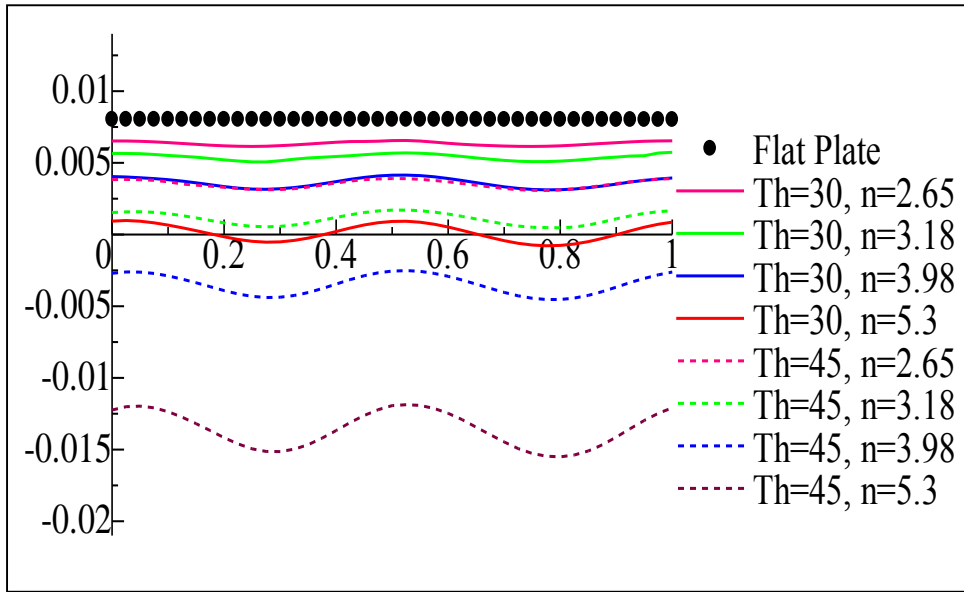


**Fig. 2.26 Total x-directional force for different frequencies and fin angles produced by body and fin (one period)**

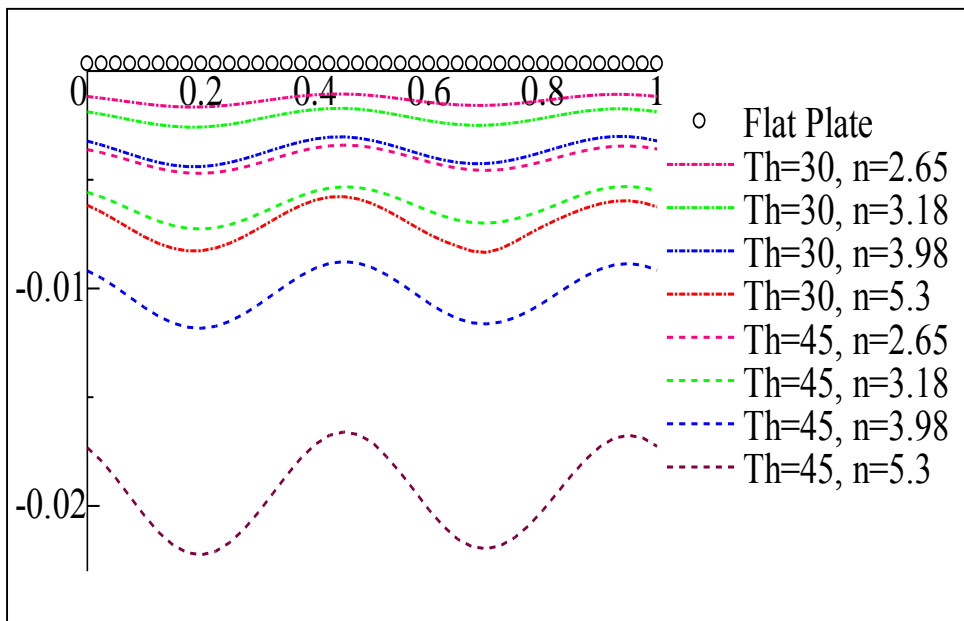


**Fig. 2.27 Total x-directional force for different frequencies and fin angles produced by fin only (one period)**

From this figure it is observed that the amount of thrust forces for  $\theta = 30$ ,  $n = 3.98$  is almost same to that produced by  $\theta = 45$ ,  $n = 2.65$ . In this case the self propulsion frequency is about 5.3 for  $\theta = 30$ ,

which is different from the previous computation. This might be because of large frictional drag of thick body of the present computation.

The similar case but considering the force produced by only fin is shown in Fig. 2.27. In this figure, all graphs except the flat plate shows the negative value; that is, the total force dominates the frictional force. This is because the frictional force of the fin is small compared to the pressure force produced by it.

### 2.5.2 Contours

In this section, the contours of velocity, pressure and thrust force distribution on the surface of Model-4 are drawn to understand the flow physics around the undulating fin. For consistency, the results are shown for the same non-dimensional frequency 3.18. Every pair of figures is shown for maximum fin angle  $\theta = 30$  degree and  $\theta = 45$  degree so that the difference of distribution can be understood easily. Fig. 2.28 shows the  $x$ -directional velocity distribution around the fin for different time steps in one period. The snaps are taken from  $xz$ - plane near the side line of the undulating fin; the procedure of cutting the slice by a  $xz$ -plane was similar to that shown in Fig. 2.15(a). Fig. 2.28(a) shows the velocity distribution at  $\theta = 30$ ,  $n = 3.18$  and the Fig. 2.28 (b) shows the case of  $\theta = 45$ ,  $n = 3.18$ . The variation in velocity distribution around the fin was occurred due to the undulation of the side fins. In both figures, the boundary layer is clearly visible near the surface of the fin (blue color).

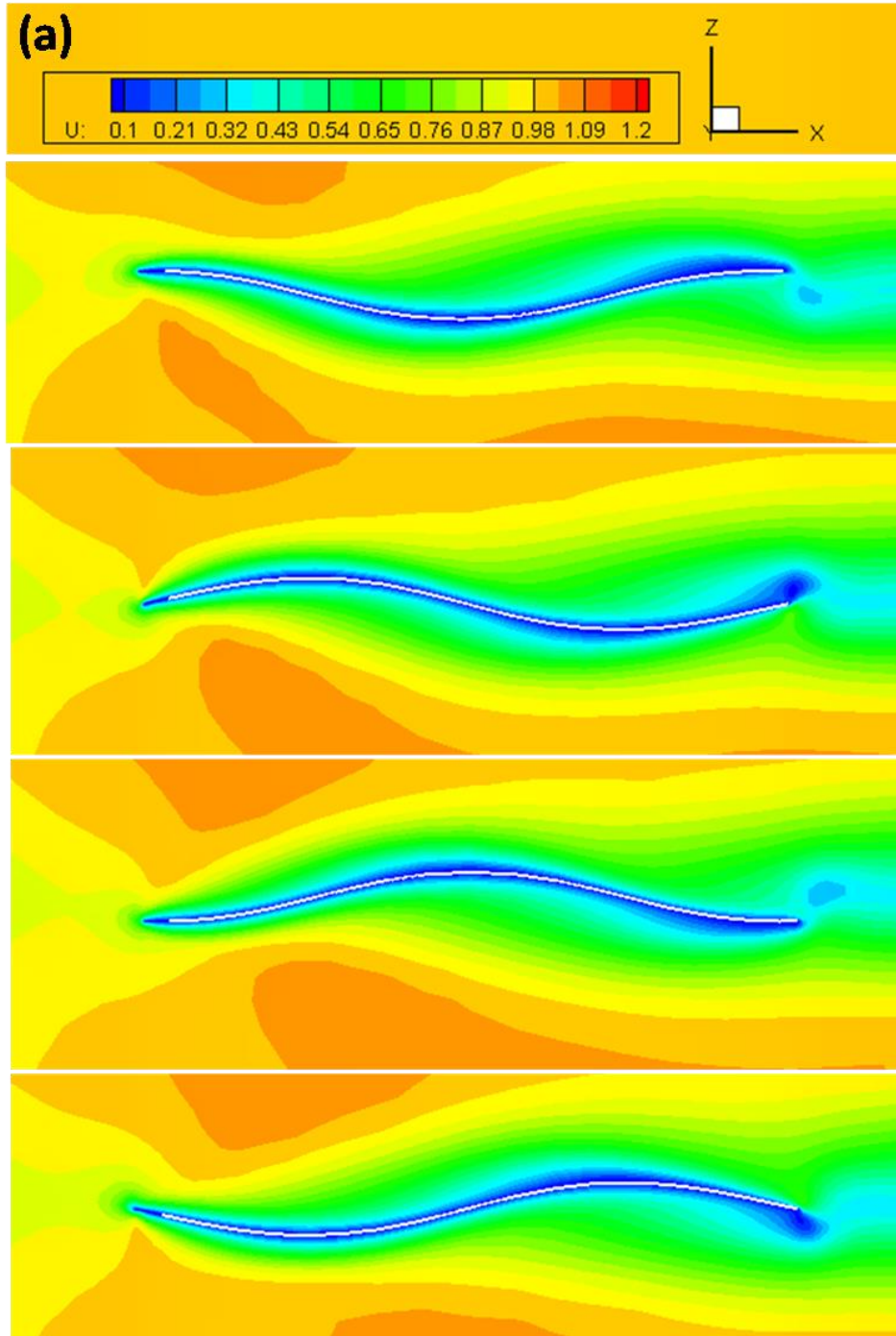


**Fig. 2.28 (a) Contours of  $x$ -directional velocity distribution at  $\theta = 30$ ,  $n = 3.18$**

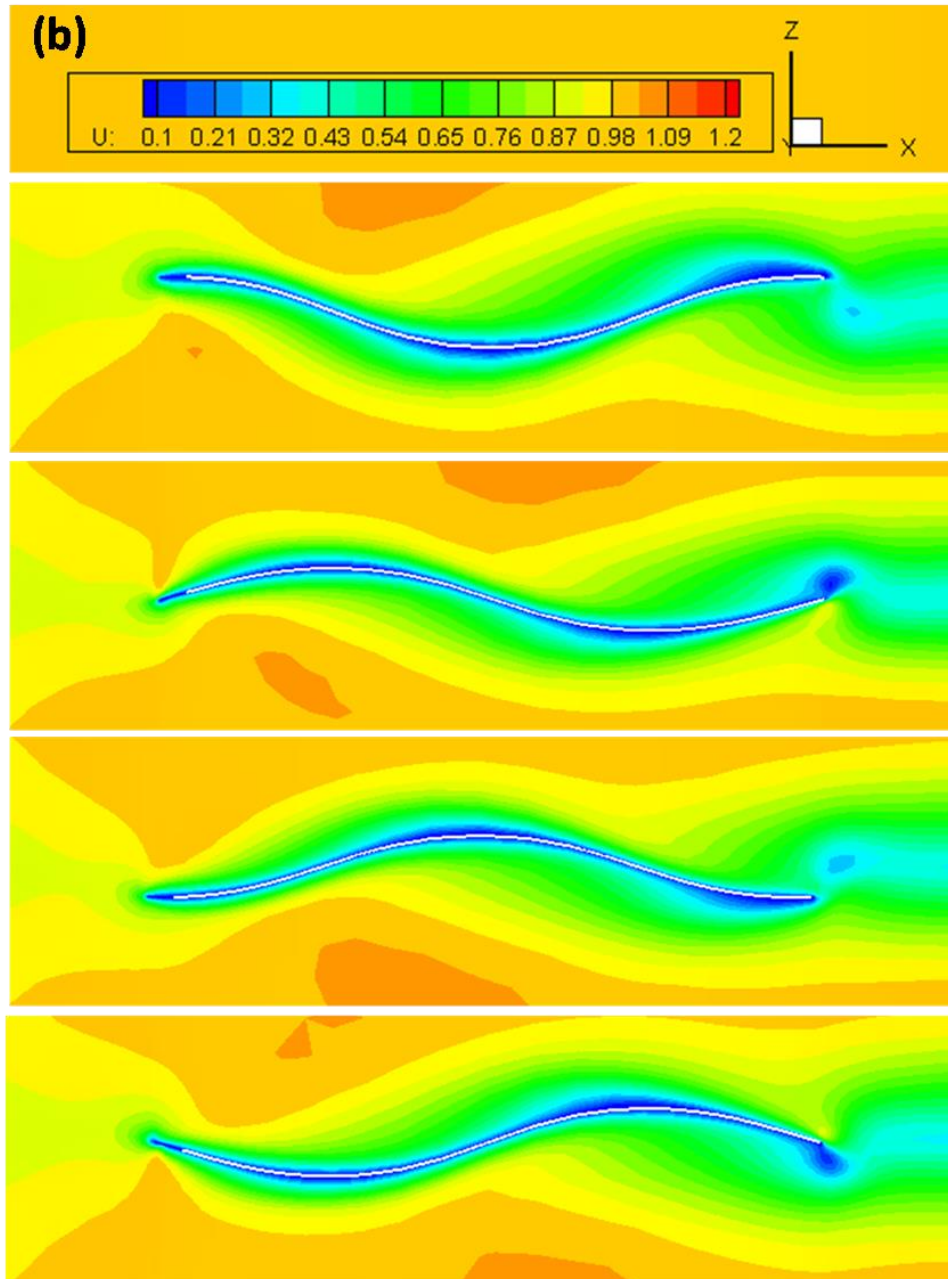


**Fig. 2.28 (b) Contours of x-directional velocity distribution at  $\theta = 45$ ,  $n = 3.18$**

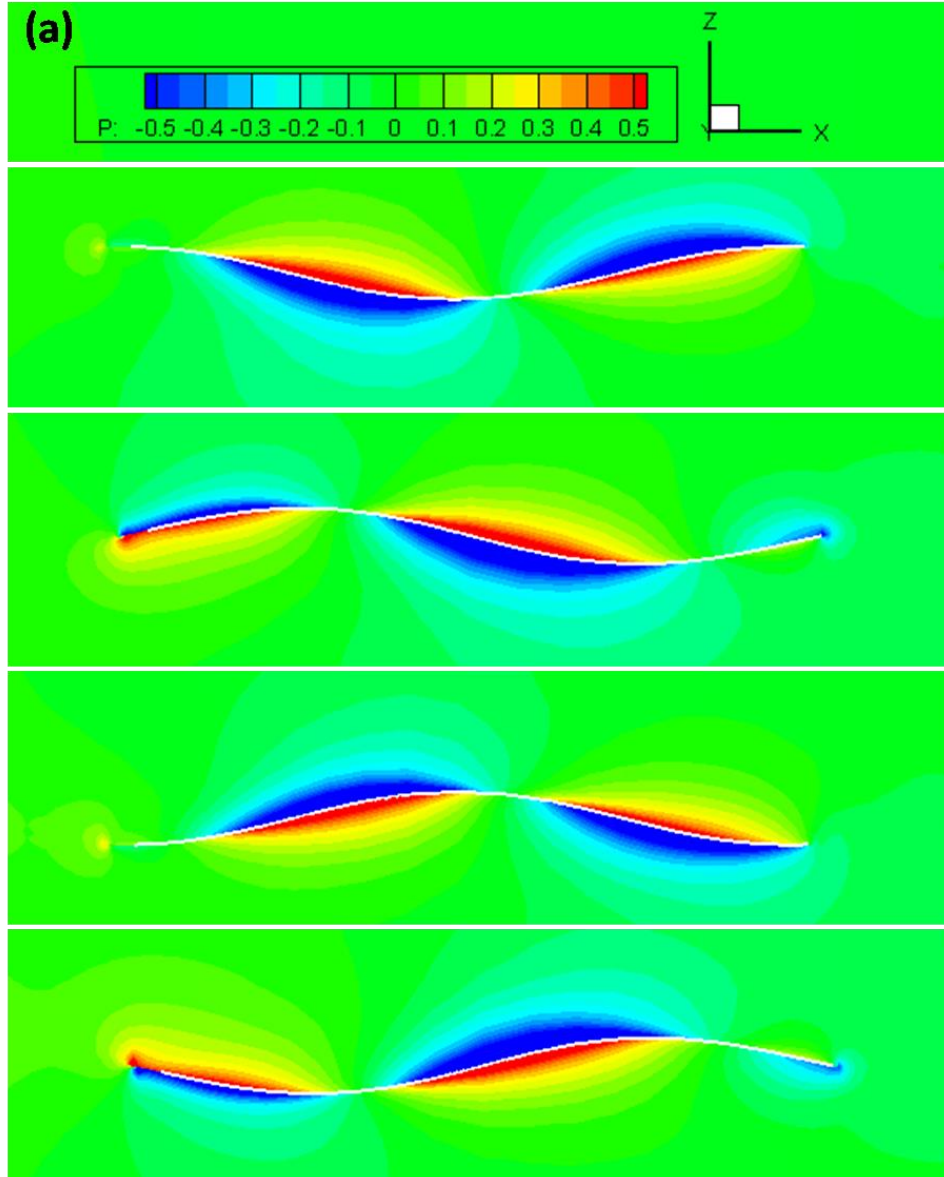


**Fig. 2.29 (a) Contours of  $x$ -directional pressure distribution at  $\theta = 30$ ,  $n = 3.18$**

The pressure distribution on the same phase and at the same condition of previous figures is shown in Fig. 2.29. Negative and positive pressures were created simultaneously due to the undulation of the fin. From this figures it is also observed that the pressure distribution on upper and lower surface is different at the same point (blue & red). Moreover, the pressure distribution on the upper and lower surface of the fin for the case  $\theta = 45$  (Fig. 2.29b) is prominent than that of the case  $\theta = 30$  (Fig. 2.29a). It is also observed that the pressure distribution on the upper and lower side of the fin at  $T/4^{\text{th}}$  &  $3T/4^{\text{th}}$  and  $T/2^{\text{th}}$  &  $T^{\text{th}}$  time steps are almost similar but opposite in sign. The pressure difference

between the upper and lower surface is very important because it is the main factor for producing the thrust force by the undulating fin propulsion system.

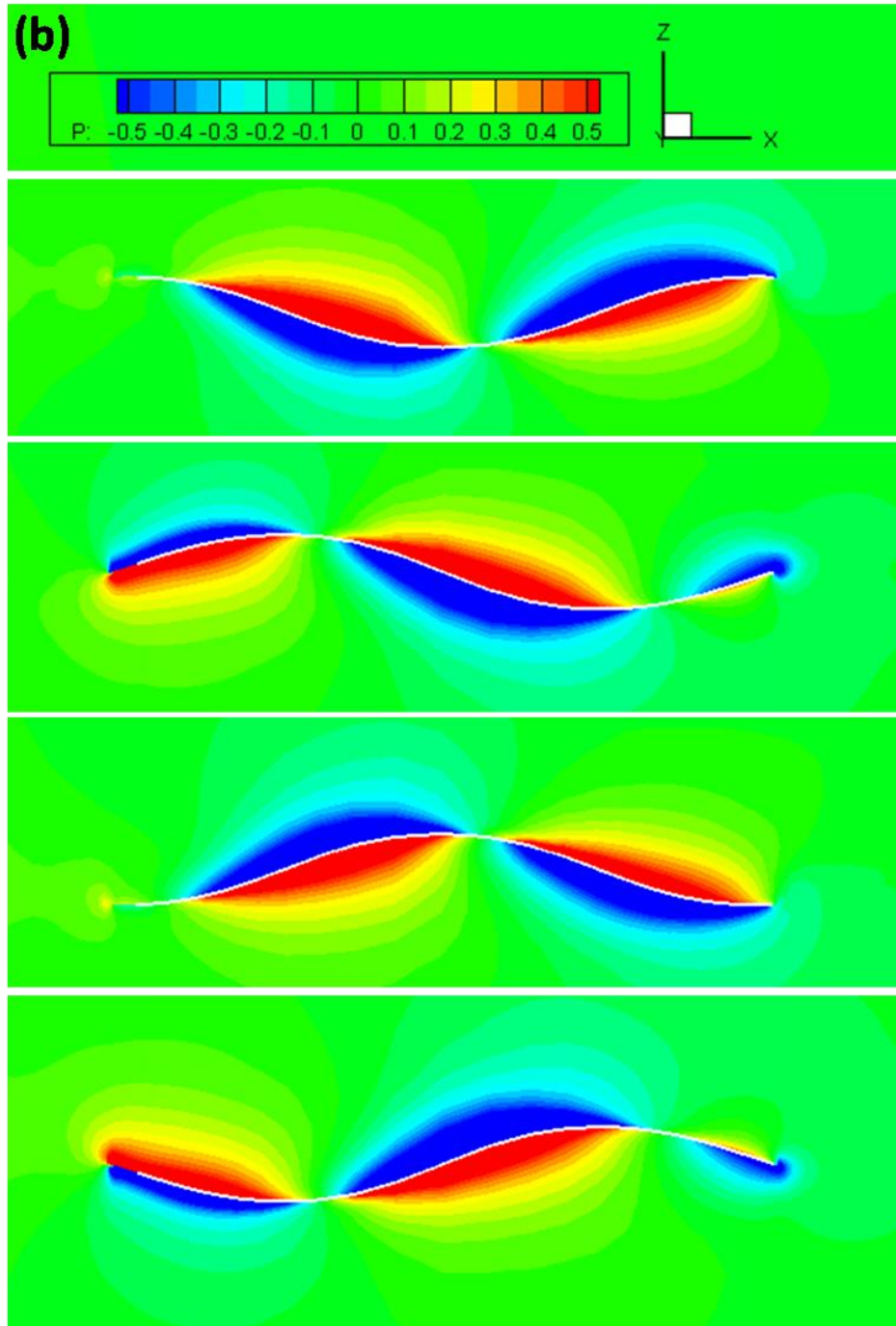
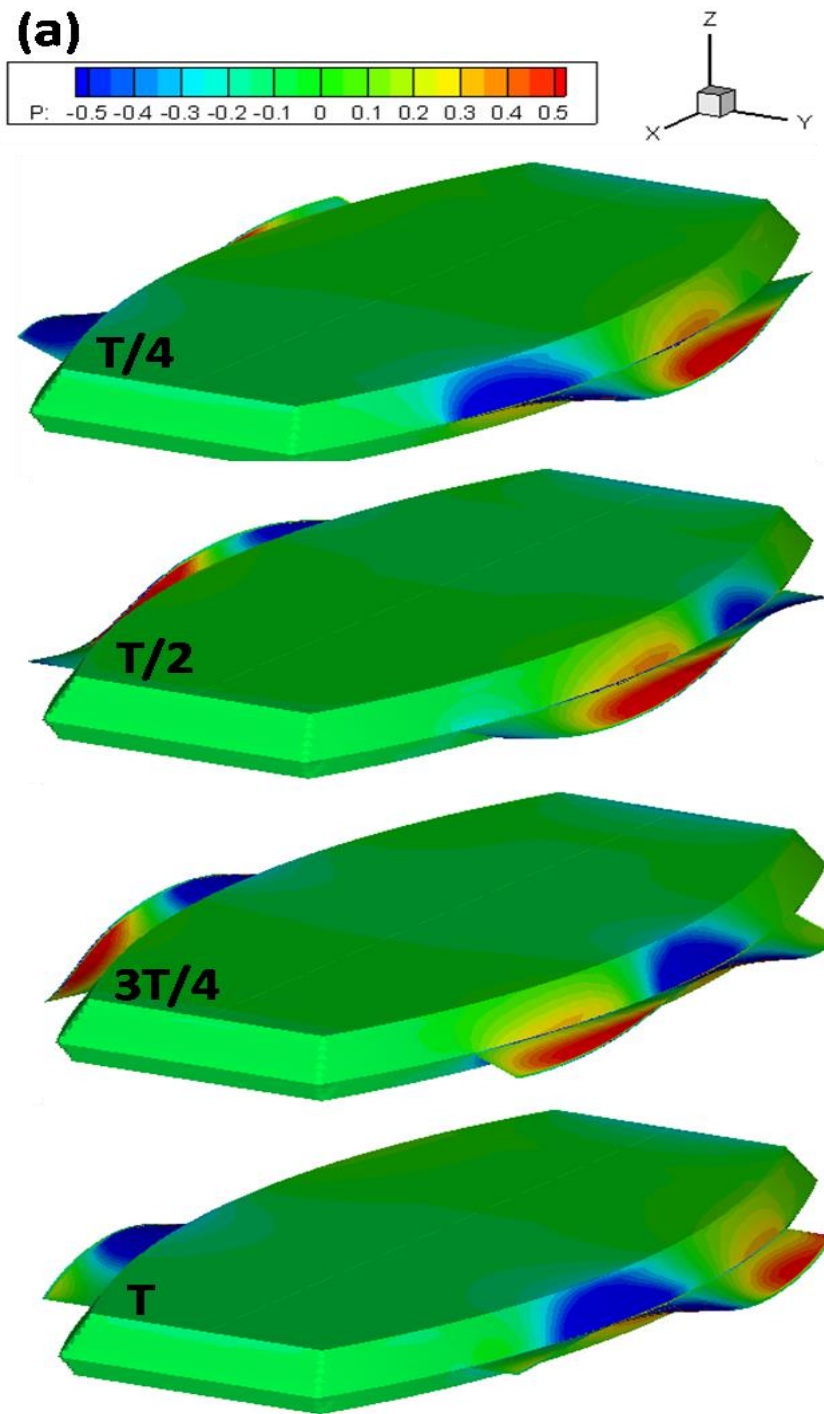


Fig. 2.29 (b) Contours of  $x$ -directional pressure distribution at  $\theta = 45$ ,  $n = 3.18$



**Fig. 2.30 (a) Pressure distribution on the Model-4 of Squid-robot at  $\theta = 30$ ,  $n = 3.18$**

The pressure distribution on the surface of the side fins and the body of Model-4 is also shown in the Fig. 2.30 for  $\theta = 30$  (Fig. 2.30a) and  $\theta = 45$  (Fig. 2.30b). . On the body, the pressure is almost zero; however negative and positive pressures are shown on the surface of the side fin. At the sides of the

body, some effects of fin's pressure can also be seen. In contrary, the body should have some effect on the pressure distribution on the fin. It is known that the upper section and the lower section of the body are not fully symmetric; so the body effect should not be same. This is also consistence with the previous graph of Fig. 2.25.

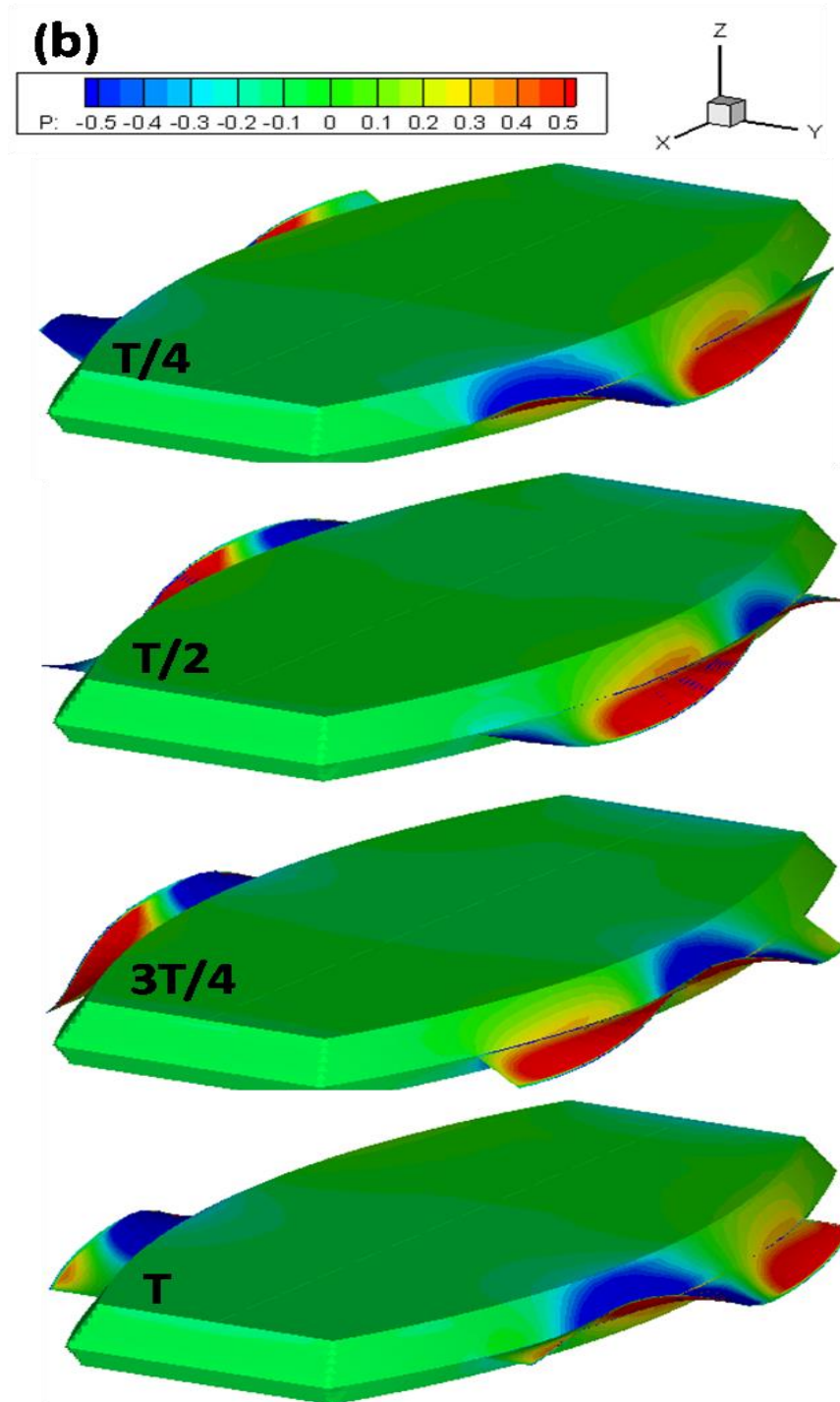
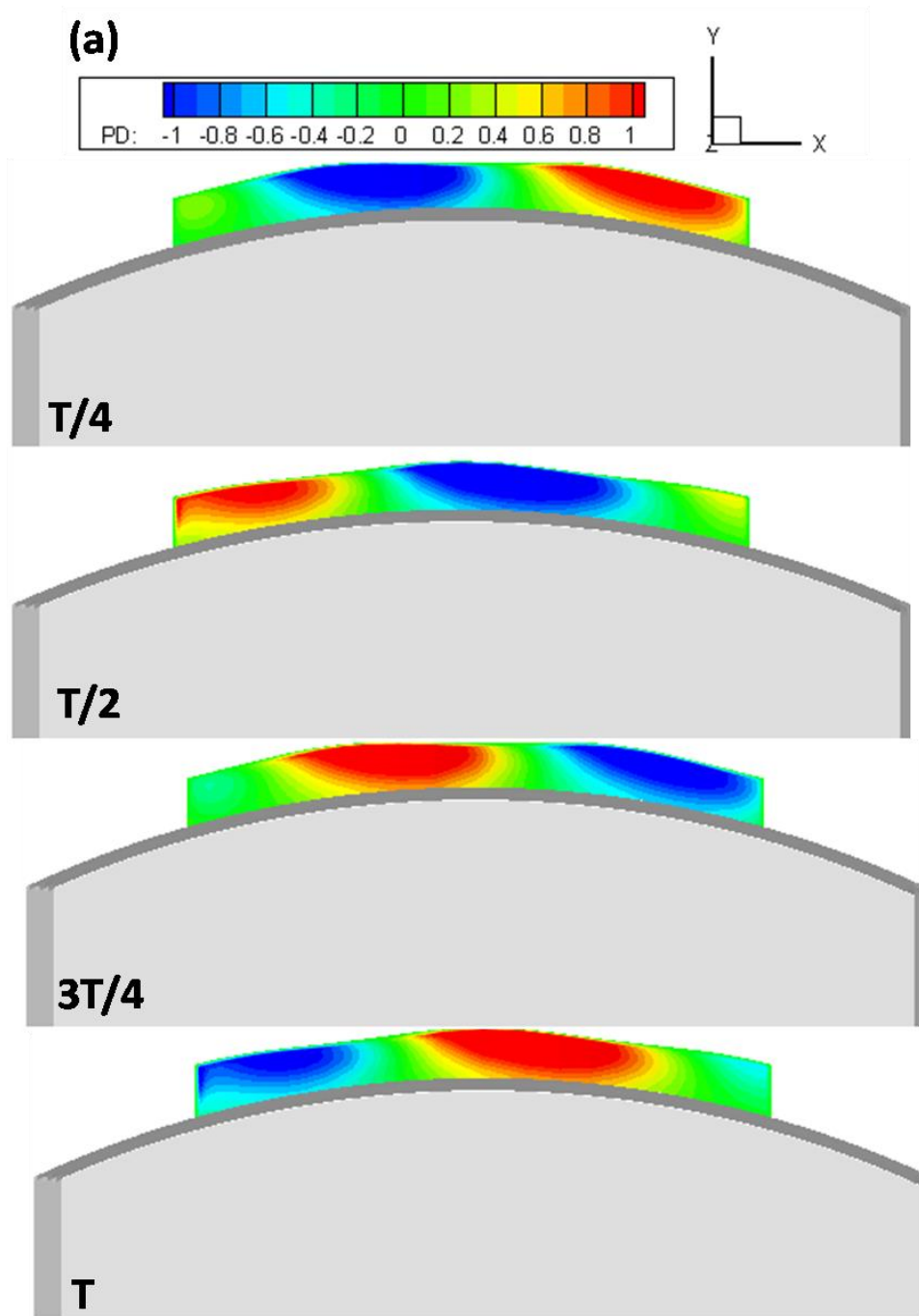


Fig. 2.30 (b) Pressure distribution on the Model-4 of Squid-robot at  $\theta = 45$ ,  $n = 3.18$



**Fig 2.31 (a) The distribution of pressure difference on the fin at  $\theta = 30$ ,  $n = 3.18$**

The top view ( $xy$ -plane) of the distribution pressure difference on the fin at different time steps of one preod for  $\theta = 30$  and  $\theta = 45$  are shown in Fig 2.31. In this case the difference was calculated by pressure of upper surface – pressure of lower surface. From this figure it is seen that the negative

pressure (blue color) and positive pressure (red color) were created simultaneously. As mentioned before, this pressure difference is mainly responsible of producing thrust force.

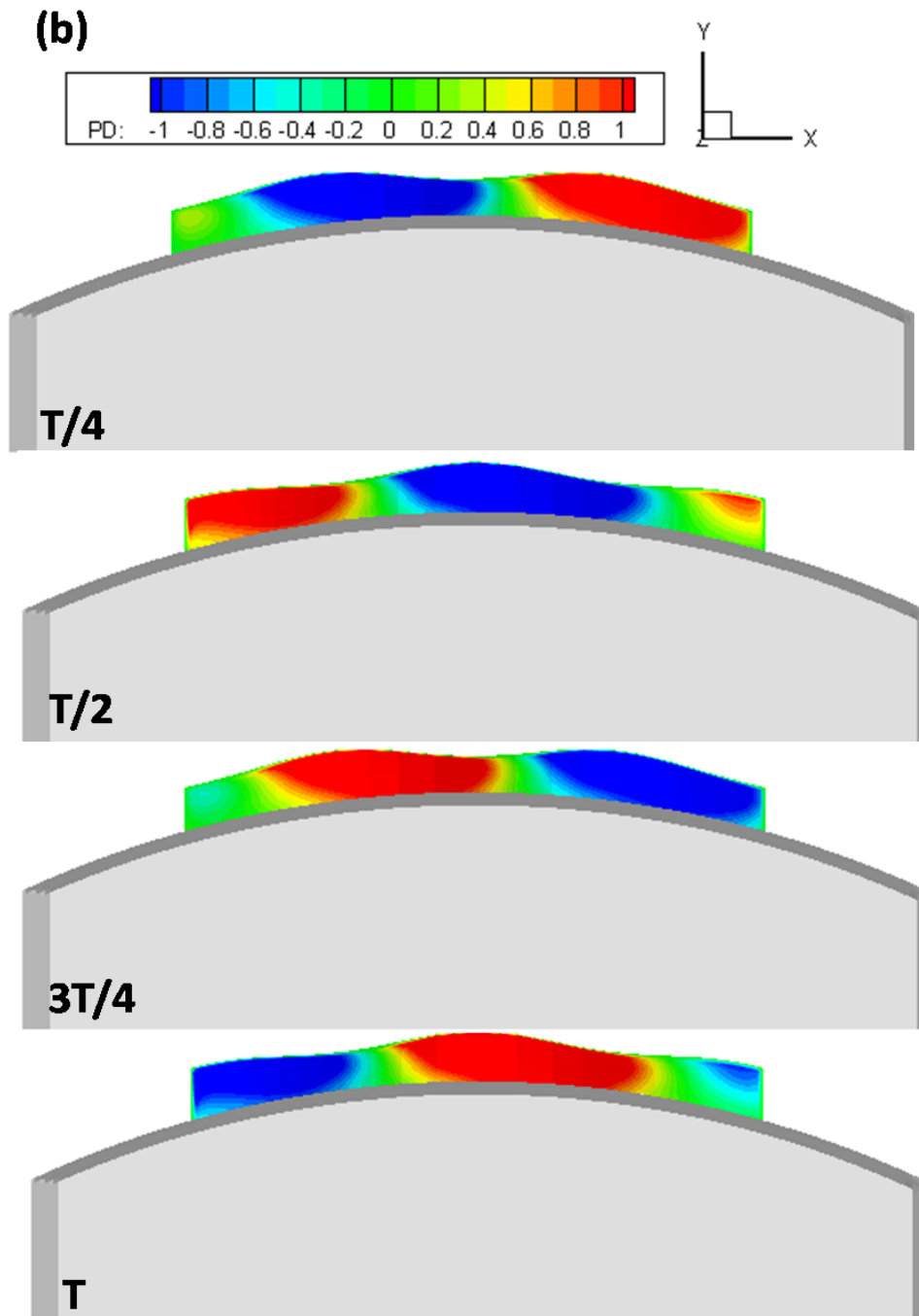


**Fig 2.31 (b) The distribution of pressure difference on the fin at  $\theta = 45$ ,  $n = 3.18$**

The  $x$ -directional thrust force is computed by the product of pressure difference between the upper and lower surface of the fin and the normal  $x$ -direction vectors, similar way as shown in Fig. 2.16.

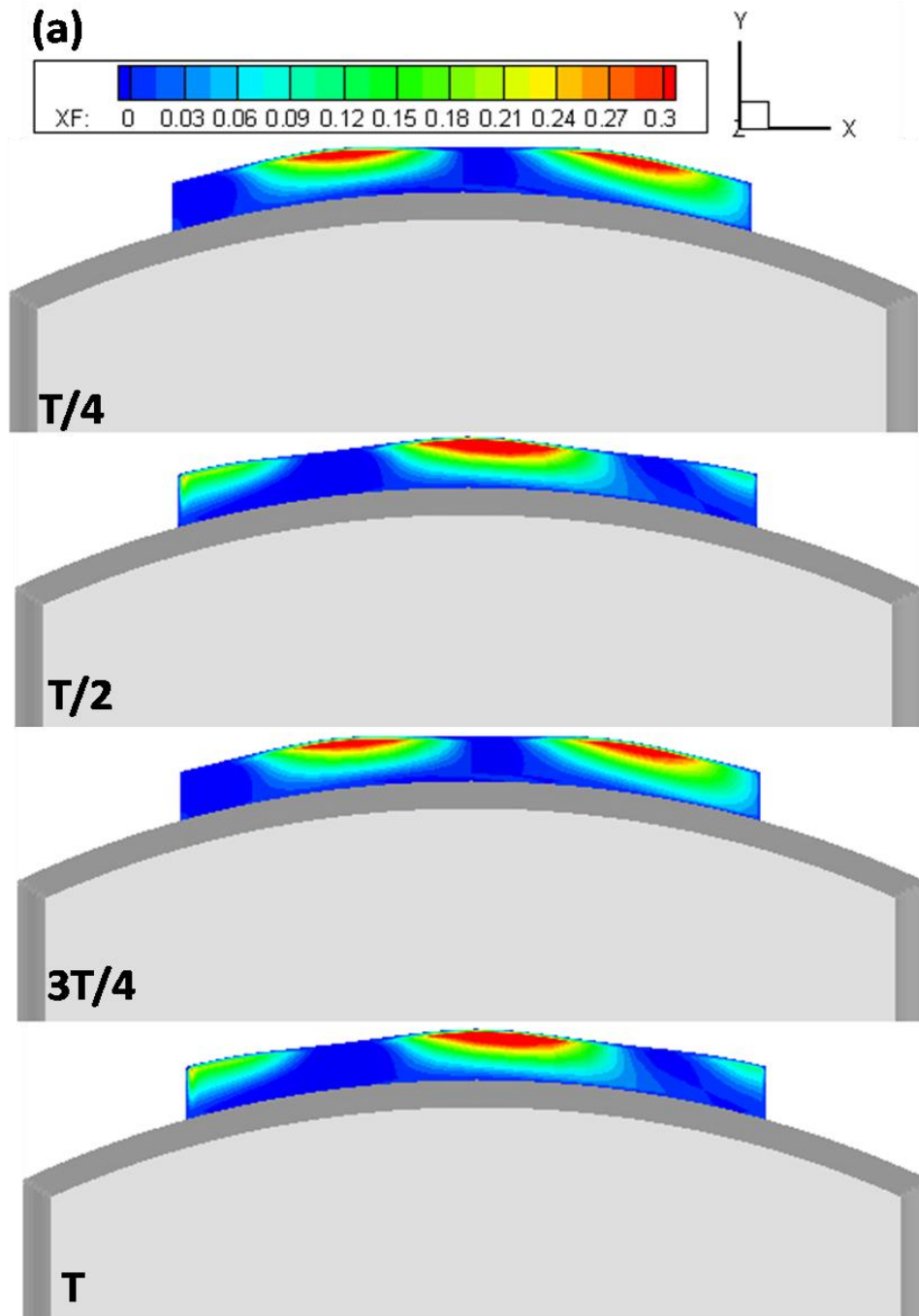


**Fig 2.32 (a) The distribution of  $x$ -directional thrust force on the fin at  $\theta = 30$ ,  $n = 3.18$**

In Fig. 2.32, the distribution of  $x$ -directional thrust force at same position of Fig. 2.31 is shown. From this figure, it is confirmed that the side fin produces  $x$ -directional thrust force during both up-stroke and down-stroke movement during its undulation. For example, at  $T/2^{\text{th}}$  and  $T^{\text{th}}$  position, the pressure distributions are different (positive & negative) but the force distribution is same (positive). These

phenomena are usual and similar to those of the computation results of the previous section 2.4. So, it can be concluded that the computation of the flow field of the real Model-4 is also accurate.

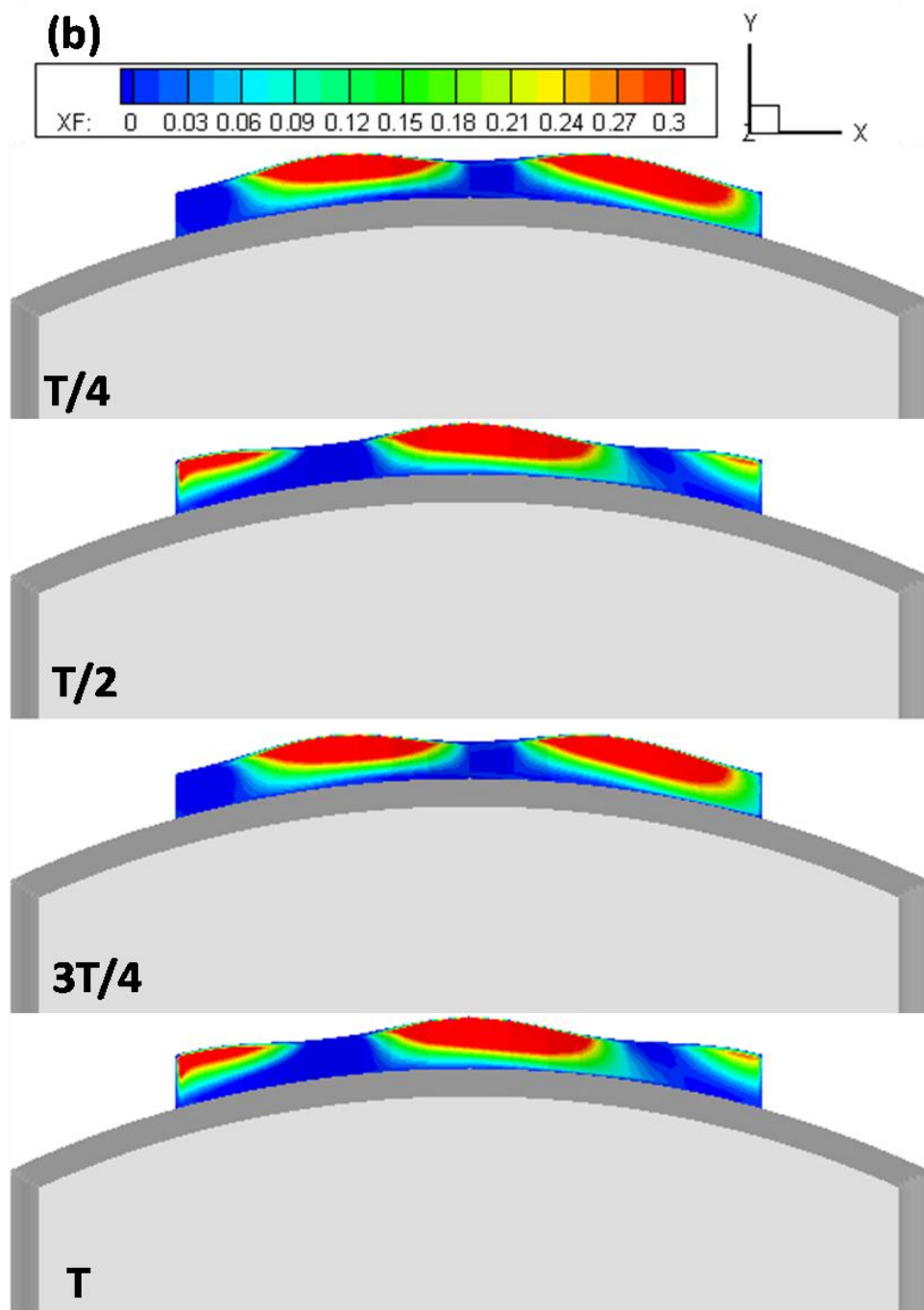


Fig 2.32 (b) The distribution of x-directional thrust force on the fin at  $\theta = 45^\circ$ ,  $n = 3.18$

### 2.5.3 Comparison of Results

For fin, the open characteristic ( $K_x - J$ ) was also calculated and compared with the experiment and previous computational results. The calculation of thrust coefficient ( $K_x$ ) and advance coefficient ( $J$ ) is similar to Eq. 2.20 and Eq. 2.21. In this case the thrust force ( $T_x$ ) was estimated by subtracting the total force of body with flat fin from the total force of body with fin. The average value was taken from a conversed period. Fig. 2.33 shows the fin open characteristic at  $\theta = 30$  and  $\theta = 45$ . From Eq. 2.22, we know that the thrust coefficient is proportional to the square of maximum fin angle; this relation was also verified by this computation. The calculated value (green dash line) of  $\theta = 30$  was found by dividing the value of  $\theta = 45$  by 2.25 (as  $(45/30)^2 = 2.25$ ); which is close to the computed value of  $\theta = 30$ .

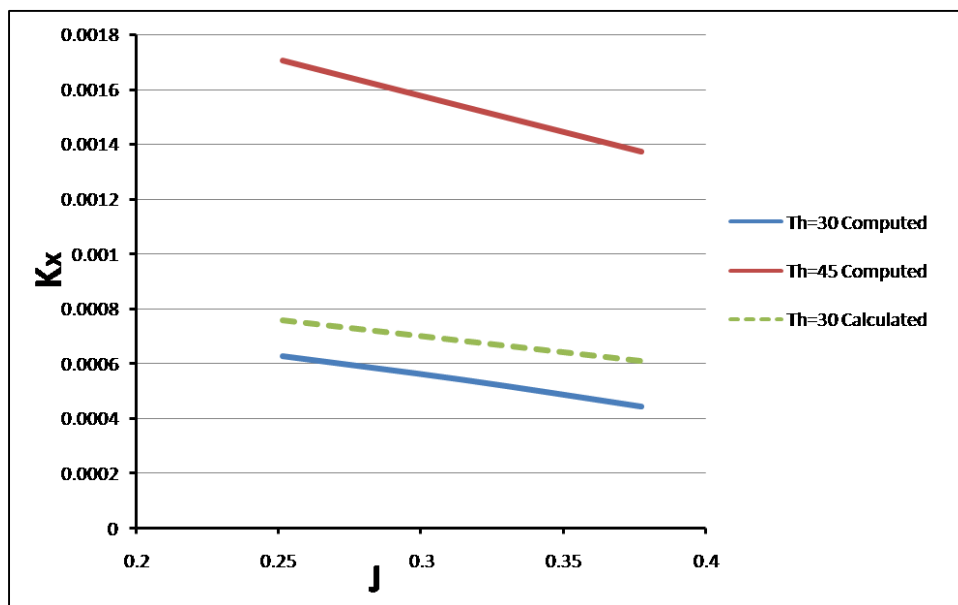
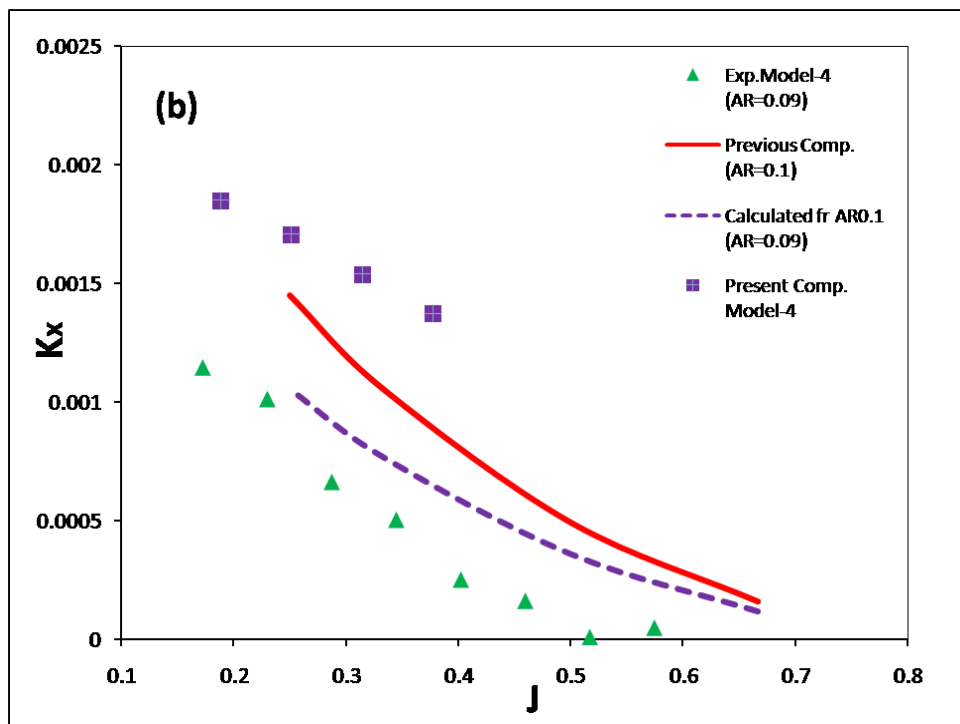
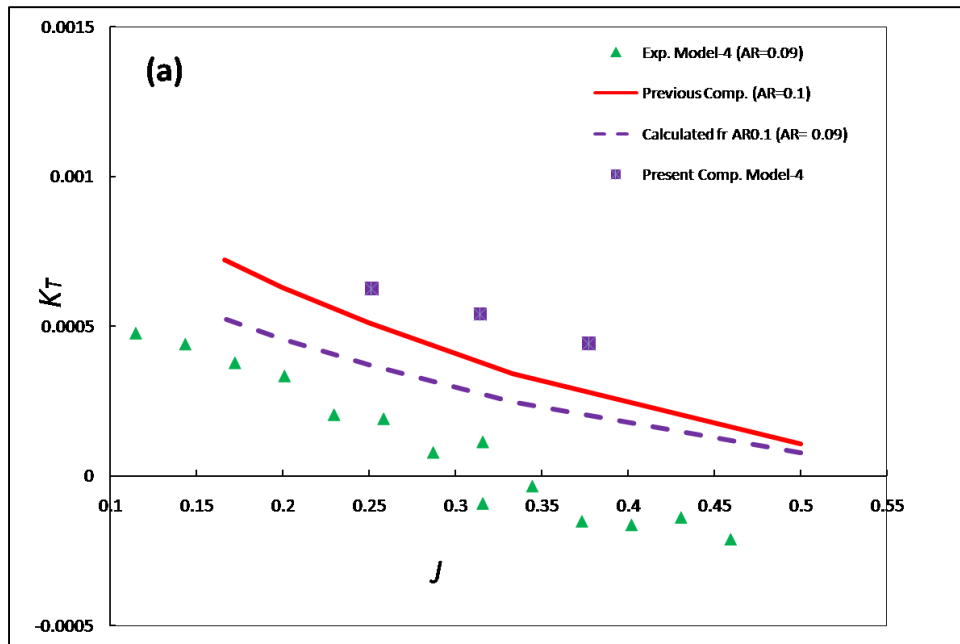


Fig. 2.33 Fin open characteristic  $\theta = 30$  and  $\theta = 45$

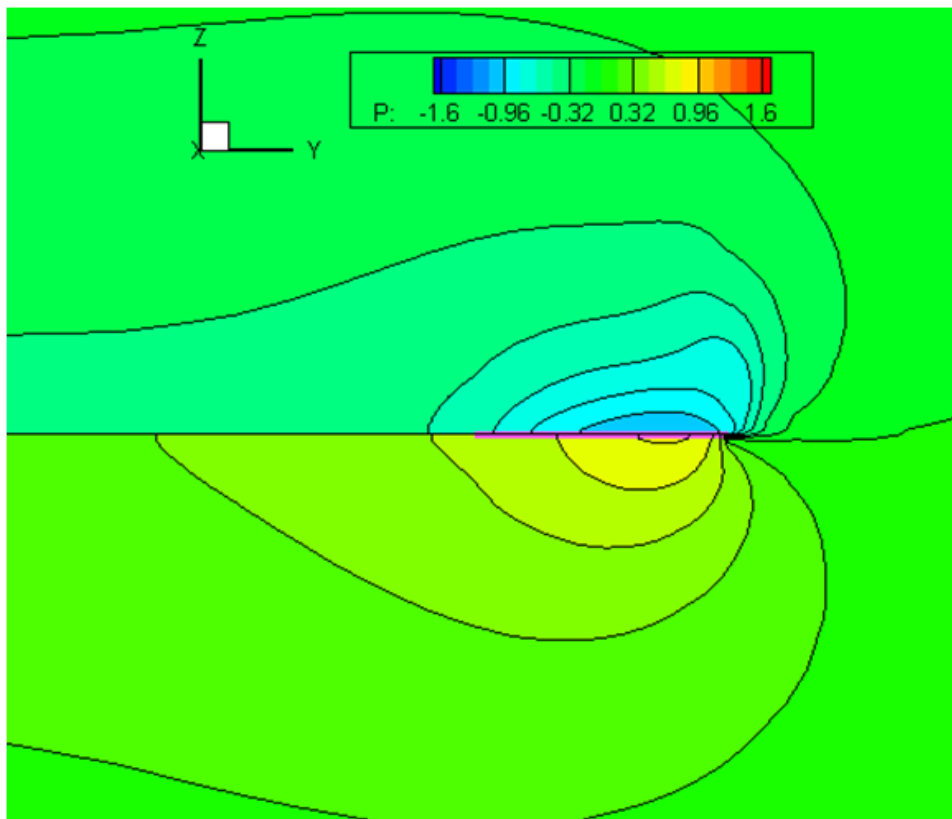
The comparison of the computed fin open characteristic with the experiment and the previous computation was shown in Fig. 2.34. Fig. 2.34(a) shows the result of  $\theta = 30$  and Fig. 2.34(b) shows the result of  $\theta = 45$ . The green triangle is the experimental result of real Model-4 with aspect ratio

0.09. In the previous section 2.4, the computation was conducted for AR=0.1, 0.07 and 0.05. However the results of same aspect ratio (AR = 0.09) was calculated from the nearest AR = 0.1. As we know from Eq. 2.22, the thrust coefficient is also proportional to the cube of aspect ratio; so the value of AR = 0.09 was found by dividing the value of AR = 0.1 by 1.37 (as  $0.1/0.09)^3 = 1.37$ ).



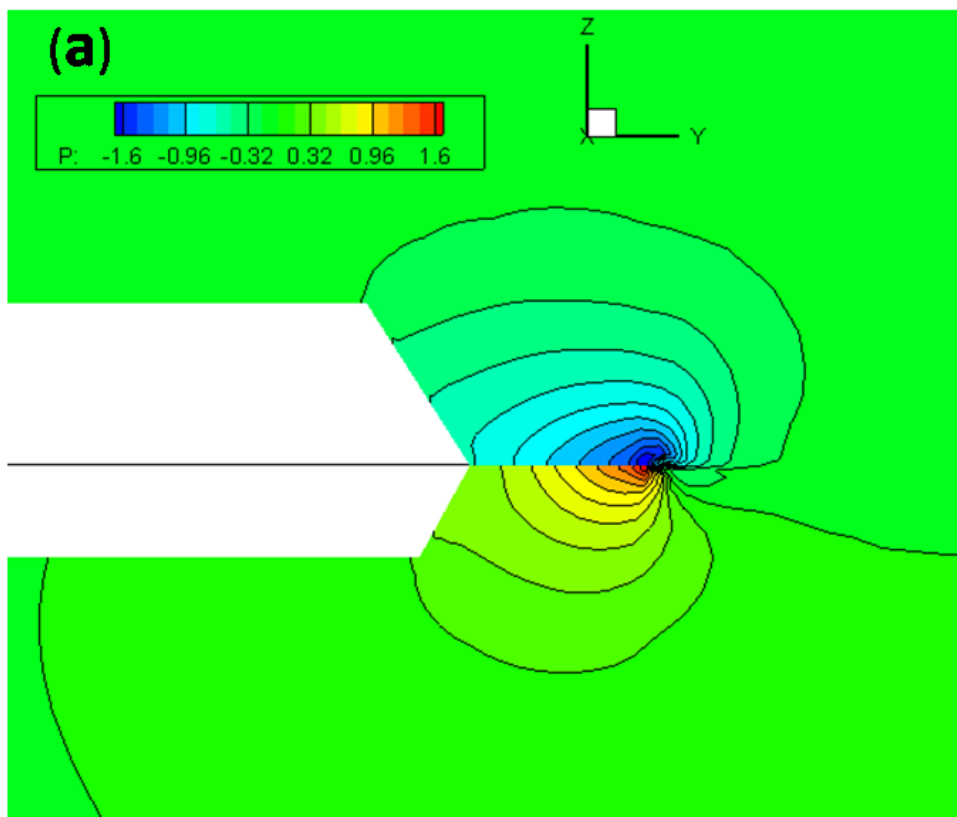
**Fig. 2.34 Comparison of fin open characteristic (a)  $\Theta = 30$ ; (b)  $\Theta = 45$**

From both of the figures, it is observed that the present computational result shows larger value of thrust coefficient than the previous computational result and also the experiment. To investigate the reason of getting different results from two computations, the computational results from both cases was examined for same condition and at same  $J$ . For this reason, the previous computation on flat body was conducted again for  $AR = 0.09$ ,  $\Theta = 45$  and  $n = 3.18$  ( $J = 0.314$ ) and compared with the present computational result of same condition. Fig. 2.35 shows the sectional view of pressure distribution on the fin and on the flat body. Also, the pressure distribution on the fin and on the thick body of Model-4 at similar condition is shown in Fig. 2.36 (a). The fin length of the present computation is shorter than the previous case; so the actual frequency of the present case was larger.



**Fig. 2.35 Pressure distribution on the flat body and on the side fin of previous computation**

For taking the result of same phase result, the data of the mid position of the fin was taken for both cases. From this figure, it is observed that the pressure distribution of Model-4 case (Fig. 2.36a) is more prominent than the flat body case (Fig. 2.35). The reason of this phenomenon might be because of the difference in body shape of two cases. In the previous case the body was considered as flat where as in the present computation the body is thick like real Model-4. It is seen that, in case of flat body (Fig. 2.35) the pressure contour lines go across the flat body but in case thick body of Model-4 (Fig.2.36a) it is hindered by (almost) vertical wall of the body. Due to the shape of Model-4 the horizontal velocity was hindered by the wall that increased the pressure force as a result the thrust force was also increased. The sectional views of pressure distribution for different  $x$ -stations are also shown in Fig. 2.36b-c. The Fig. 2.36b shows the case when the fin pushes the water down word and the Fig. 2.36c shows the fin is moving upward. Positive pressure distribution is seen at the side of fin's moving direction. In both cases, the pressure contours are also hindered by the wall of the body.



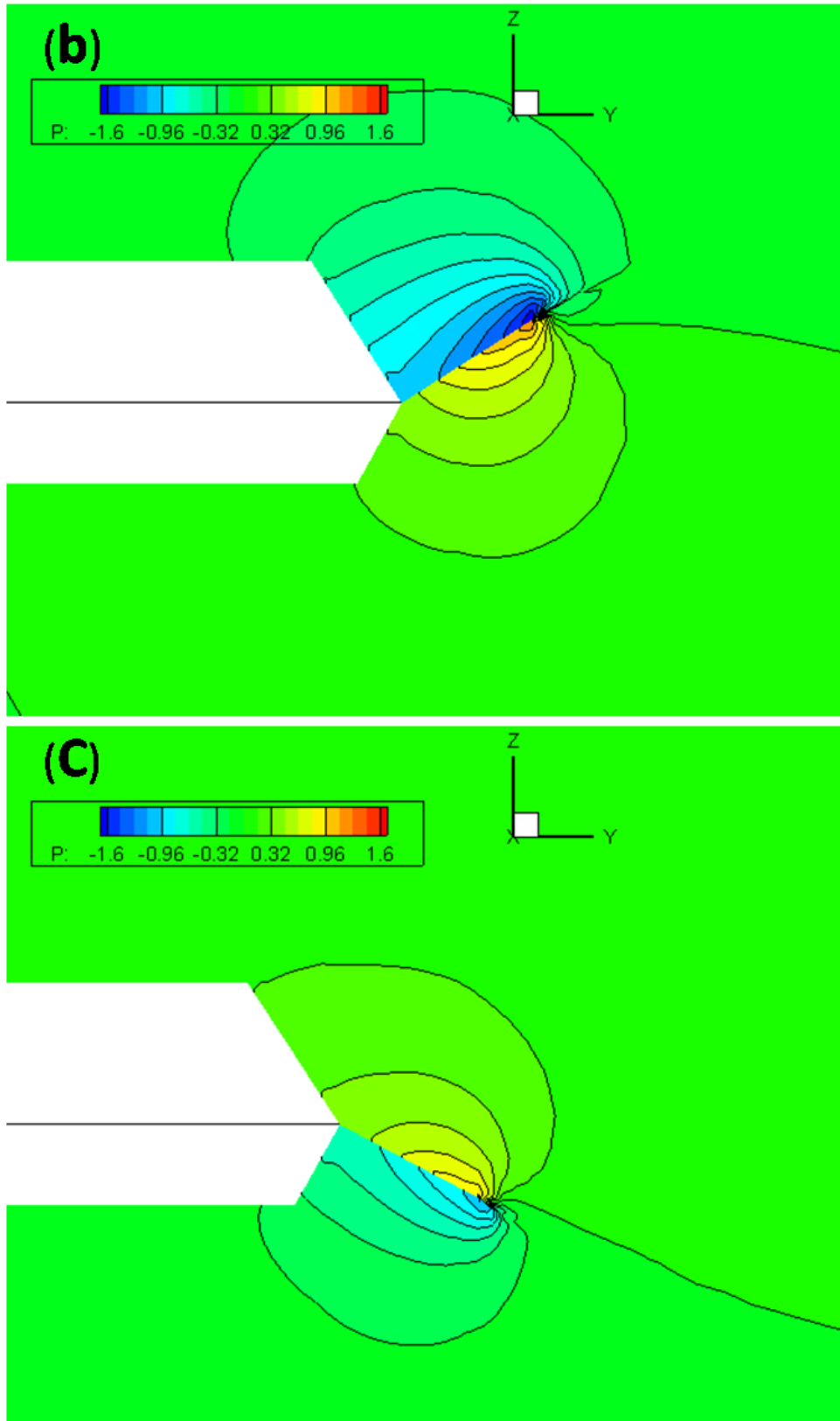


**Fig. 2.36** Sectional view of pressure distribution at different  $x$ -stations on the body and on the fin of Model-4

According to the previous discussion, the thrust coefficient from the experiment should also give the higher value like present computation; because similar bodies were considered for both cases. But in Fig. 2.34, it is seen that the computed thrust coefficient is larger than experiment. This reason might be different. In the real model, there is little gap between the body and fin (Fig. 2.37). There is no rubber sheet between the connection area of body and fin; so there might be some pressure loss due the blank space.

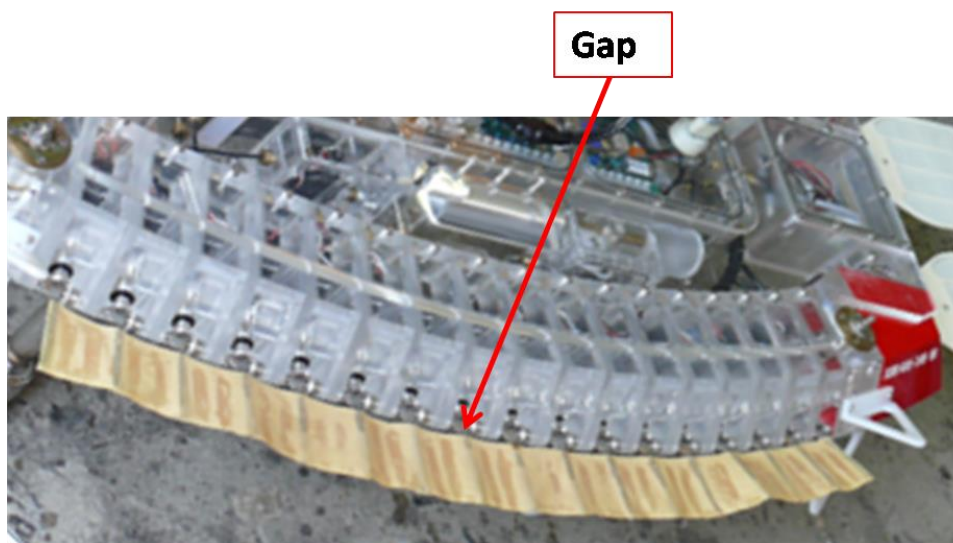


**Fig. 2.37 Picture of a side fin of Model-4 where the gap between the fin and body is indicated**

So, from the computational result it is suggested that a rubber sheet should be used to remove the gap between body and fins of the real model to get more thrust force. In this case the undulating fin would produce more thrust and the robot will swim faster. This assumption will be examined by doing the computation considering the gap and also doing experiment with the real Model – 4 by covering the gap.

## **2.6 Summery**

The CFD computation on the flow around a flat body with two undulating side fins and the real Model-4 was calculated. The relationship between the relative velocity of fluid and the dimension of the fin was investigated based on the distribution of pressure difference between upper and lower surfaces and thrust force distribution. The computational model exhibited a considerable agreement with the experimental observations. A simple relationship among the fin's principal dimensions and hydrodynamics was established using the computed results. The comparison between the force measurement and integrated force using CFD result for computed model proved that the CFD techniques can predict the hydrodynamic force produced by the undulating side fin.

### **3. Chapter 3: Braking Performance of the Undulating Fin Propulsion System of the Squid-Robot**

#### **3.1 Preamble**

In this study, the braking performance of the undulating fin propulsion system of a biomimetic squid-like underwater robot was investigated through free run experiment and simulation of the quasi-steady mathematical model. The quasi-steady equations of motion were solved using the measured and calculated hydrodynamic forces and compared with free-run test results. Various braking strategies were tested and discussed in terms of stopping ability and the forces acting on the stopping stage. The stopping performance of the undulating fin propulsion system turned out to be excellent the short stopping time and short stopping distance. This is because of the large negative thrust produced by progressive wave in opposite direction. It was confirmed that the robot can apply its braking performance effectively even in the complex underwater explorations.

#### **3.2 Introduction**

The braking of the translational and rotational motions is very important performance as well as the cruising speed, because the short term and short distance stopping after discovering the target is very important in the disturbed flow for exploration. The Squid-robot showed excellent maneuverability in swimming and it could move in any direction in the 3D space. However, for precise maneuverability, the robot should have highly capable braking capacity. So, the braking performance of the squid-like underwater robot with undulating side fins was investigated and that will be discussed in this chapter. The ability of moving along any prescribed route in calm water has already been proved by different experiments. However, the fine braking ability becomes more important in case of underwater robotic applications, since during the operation the robot has to move around an unknown geometry in the underwater region to find an untraced item or for installation or repairing activities. During the previous study (Toda et al. 2009), it was found that the robot can change the direction for translational

and rotational motions very easily due to the large negative thrust in the early stage of the change of direction. It could be predicted by equation of motion under the quasi-steady assumption. The open characteristics of side fins found in the previous study are shown in Fig. 3.1. Here the thrust coefficient ( $k_x$ ) and advanced coefficient ( $J_x$ ) are defined as  $K_x = T_x / (\rho N |N| L^4)$  and  $J_x = U / (NL)$ ; where,  $T_x$ : thrust,  $\rho$ : density,  $U$ : advanced velocity,  $N$ : frequency (negative  $N$  means that the wave direction of fin is opposite, i.e. forward direction), and  $L$ : length of the fin. From this figure, it is observed that the undulating side fin propulsion system of the robot can produce large thrust in the negative  $J_x$  region (the forward velocity and negative direction fin's motion or backward velocity and usual direction fin's motion shows negative  $J_x$ ). In the present study, the characteristics for forward and backward motions are same due to symmetric geometry. In Fig. 3.1, the characteristics in two quadrants are shown.

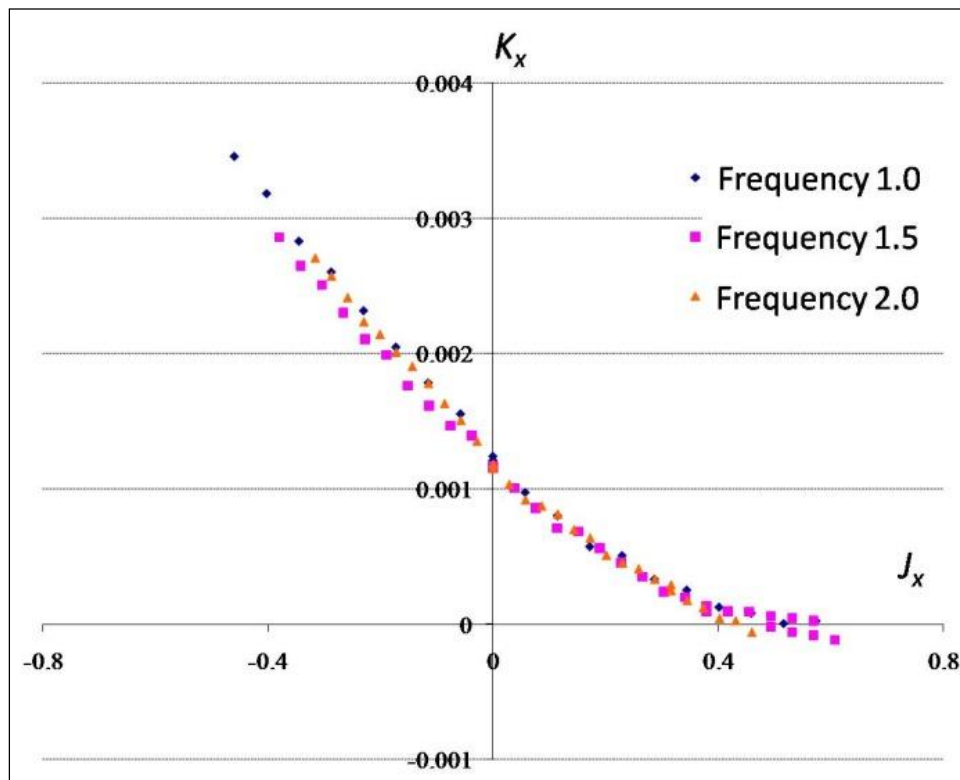


**Fig.3.1 Fin Open characteristics ( $K_x - J_x$ )**

The braking performance had not been investigated because the short term operation of negative direction is required. In this study, the model operation was first investigated by manual handling. In the tests, the operator could stop the model at desired point after a few times training. The time for braking operation was measured and the motion was predicted by solving the quasi-steady equation of motion. Although the unsteady or transient effect seems to be required because the time for negative direction operation is very short, the braking motion was predicted well for translational and rotational motion. After those tests, the various stopping maneuver strategies were tested by simulation. Considering the time and distance from the start of stopping motion to full stop position, it was confirmed that the braking performance of this robot is sufficient enough for exploring the underwater region.

### 3.3 Methodology

#### 3.3.1 Experimental Setup

In this study, the experiment was also conducted in the Towing Tank of Osaka University. The sketch of the experimental setup is shown in Fig. 3.2.

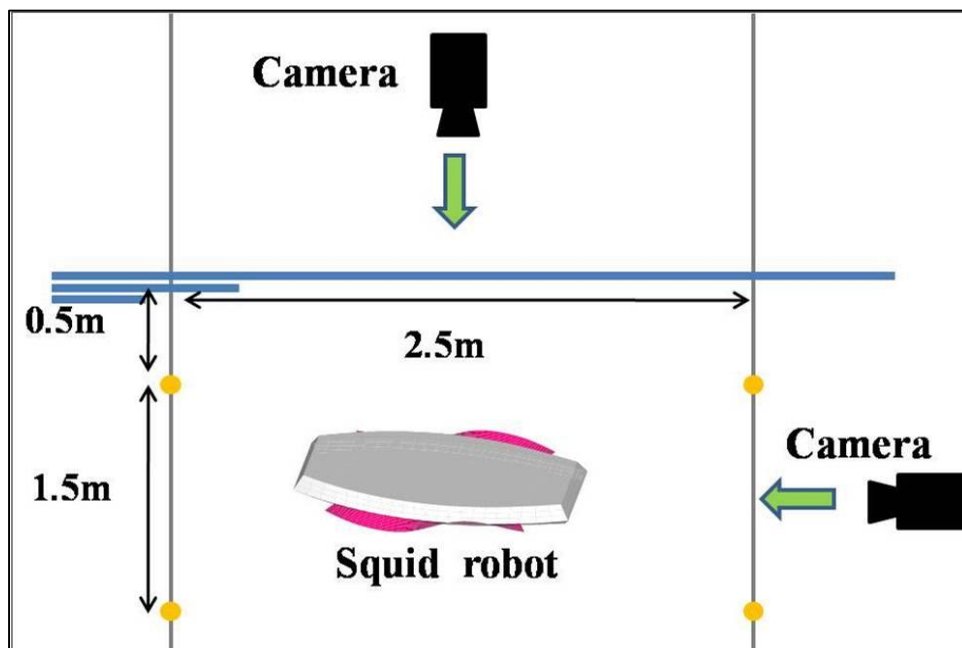


Fig. 3.2 Sketch of the experimental setup

As shown in the illustration, the range of movement of the model was 2.5 meter wide and 1.5 meter deep. Two cameras were set at the upper side and in the underwater to take the movie of upper view and side view of the robots motion respectively. 8 ping-pong balls were hanged with the rope at four corners to know the real position from the image. This method lacks high level of accuracy, but it is simple and the results can be compared with the simulation. From the movie, the motion was estimated by tracking the same point on the body of the robot. The details about experiment and the fin motion were discussed in the previous studies (Toda et al. 2009) for various motions. In this case, the fin motion in  $x$ -direction was described by Eq. 3.1-3.2. In these equations, the sign of  $N$  is considered, although the frequency is usually positive. But if the negative  $N$  is substituted, the phase velocity of progressive wave is negative, that means the wave direction is opposite. At  $N = 0$ , it is considered that the fin is flat and hydrodynamic force produced by fin is zero. It is noted that, the hydrodynamic force produced by fin is the difference between the force acting when the fin is moving and the force acting on the flat fin. The braking operation means that the negative  $N$  is applied for short period and then  $N = 0$  is applied after the steady motion using positive  $N$  for translational motion. For the rotational motion, the positive and negative  $N$  (same frequency) were applied to right and left fins, respectively for steady turning at one point. After the steady motion, the opposite wave direction motions for both sides were applied and then  $N = 0$  was applied for both fins.

$$\theta = \Theta(s) \sin(2\pi Ks - 2\pi Nt) \quad (3.1)$$

$$\Theta(s) = \sin^{-1} \left[ \left\{ 1 - 0.905 \left( \frac{s}{fL} - 0.5 \right)^2 \right\} \sin \theta_{\max} \right] \quad (3.2)$$

Where,

$\theta$ : The deflection angle of each unit (degree)

$\Theta(s)$ : The amplitude of the deflection angle; For each unit  $s$  is  $(i-1).fL/16$  ( $i=1,17$ )

$N$ : Frequency (Hz)

$K$ : Wave number (1/m)  $K.fL = 1.0$  in this study

$t$ : Time (s)

$fL$ : Fin length (m)

$s$ : Distance along the fin's root from the fin's leading edge (m)

$\theta_{max}$ : Maximum Fin's ray angle from the flat position (degree)

### 3.3.2 Simulation

The simulation study based on the equations of motion was conducted under the similar condition as that of the experiment for comparing the results. The coordinate system is sketched in Fig. 3.3; where the space fixed coordinate system  $(X,Y,Z)$  and body fixed coordinate system  $(x,y,z)$  are shown. Here  $u, v, w$  are the advanced velocity of the model in  $x, y, z$  direction respectively and  $p, q, r$  are the angular velocity. Also,  $\varphi, \theta, \psi$  are Eulerian angles.

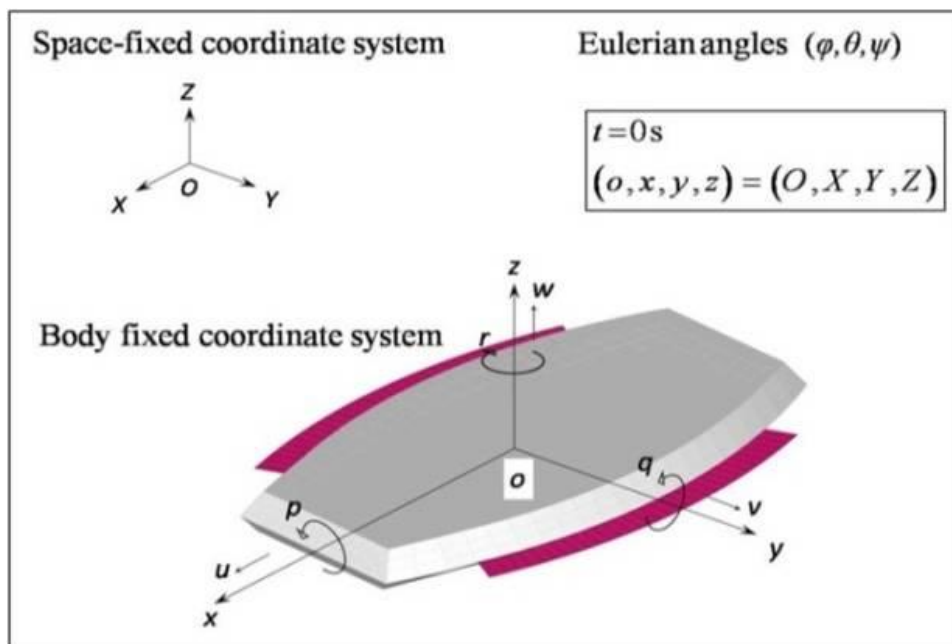


**Fig. 3.3 Sketch of the coordinate system**

In this case, the simulation was carried out for the translational motion and rotational motion. The results were found by solving the equations of motion and the hydrodynamic coefficients were obtained based on quasi-steady assumption from the towing tank captive test and the CFD

computations of fluid force around the side fins. For the following equations (Eqs. 3.3-3.5) were considered for the translational motion:

$$\frac{dx}{dt} = u \quad (3.3)$$

$$(M + M_x) \frac{du}{dt} = F_x \quad (3.4)$$

$$F_x = (f_{xpr} + f_{xpl}) - C_x \cdot u \cdot |u| \quad (3.5)$$

Where,  $M$  : Mass of the model (62.8 kg)

$M_x$  : Added mass in  $x$ -direction (5.975 kg)

$C_x$  : Constant for drag force in  $x$ -direction (47.70 kg/m)

$F_x$  : Total hydrodynamic force in  $x$ -direction (N)

$f_{xpr}, f_{xpl}$  : Thrust forces produced by right and left fin respectively (N)

In case of rotational motion, the following equations (Eqs.3. 6-3. 8) were considered:

$$\frac{d\psi}{dt} = r \quad (3.6)$$

$$(I_{zz} + J_{zz}) \frac{dr}{dt} = T_z \quad (3.7)$$

$$T_z = (f_{xpr} - f_{xpl}) \cdot \left( \frac{bB}{2} + \frac{fB}{2} \right) - C_\psi \cdot r \cdot |r| \quad (3.8)$$

Where,  $\psi$  : Heading angle (degree)

$T_z$  : Hydrodynamic moment around  $z$ -axis (N.m)

$I_{zz}$  : Moment of inertia along  $z$ -axis (10.133 kg.m<sup>2</sup>)

$J_{zz}$  : Added moment of inertia along  $z$ -axis (1.438 kg.m<sup>2</sup>)

$C_\psi$  : Constant for drag moment (6.0 kg)

$bB$  : Width of the model (0.714 m)

$fB$  : Width of the fin (0.12 m)

The advance coefficients ( $J_{xr}$ ,  $J_{xl}$ ), the thrust coefficients ( $K_{xr}$ ,  $K_{xl}$ ), and the thrust forces ( $f_{xpr}$ ,  $f_{xpl}$ ) produced by fins were calculated as follows (Eqs. 3.9-3.13):

$$J_{xr} = \frac{u+l_0 \frac{d\psi}{dt}}{N_r \cdot fL}, \quad J_{xl} = \frac{u-l_0 \frac{d\psi}{dt}}{N_l \cdot fL} \quad (3.9)$$

(Where,  $l_0 = \frac{bB}{2} + \frac{fB}{2}$ ;  $\psi = 0$  for translational motion and  $u = 0$  for rotational motion)

$$K_{xr} = (0.0312 \cdot J_{xr}^2 - 0.015J_{xr} + 0.005) \cdot \left(\theta_{mr}/30\right)^2 \quad (3.10)$$

$$K_{xl} = (0.0312 \cdot J_{xl}^2 - 0.015J_{xl} + 0.005) \cdot \left(\theta_{ml}/30\right)^2 \quad (3.11)$$

and

$$f_{xpr} = K_{xr} \cdot \rho \cdot N_r \cdot |N_r| \cdot fL^4 \quad (3.12)$$

$$f_{xpl} = K_{xl} \cdot \rho \cdot N_l \cdot |N_l| \cdot fL^4 \quad (3.13)$$

Where,  $N_r$ ,  $N_l$  : Frequency of right and left fin respectively (Hz)

$J_{xr}$ ,  $J_{xl}$  : Advance coefficients

$K_{xr}$ ,  $K_{xl}$  : Thrust coefficients

$\theta_{mr}$ ,  $\theta_{ml}$  : Maximum oscillation angles of the side fins (degree)

$fL$  : Length of the fin (0.87 m)

From Eq. 3.12-3.13, it is seen that positive frequency of the fins produces positive thrust and negative frequency (i.e. opposite wave direction of fin) produces negative thrust. The initial frequency of 1 Hz was applied to the fins in both of translational motion and rotational motion. The rotational motion was created by applying the same but opposite (positive or negative) frequency to the right and left fin. In both cases the maximum oscillation angle of the fins were considered as 45 degree.

### 3.4 Results and Discussion

#### 3.4.1 Comparison

The experimental and simulation study were conducted on the Model-4 of the squid-robot with the aim of investigating the braking performance. The performance was analyzed based on the braking capacity in translational motion and rotational motion. In both of the motions, the starting frequency of the undulating side fins of the robot was kept at 1 Hz while the maximum oscillation angles were allowed to be 45 degree.

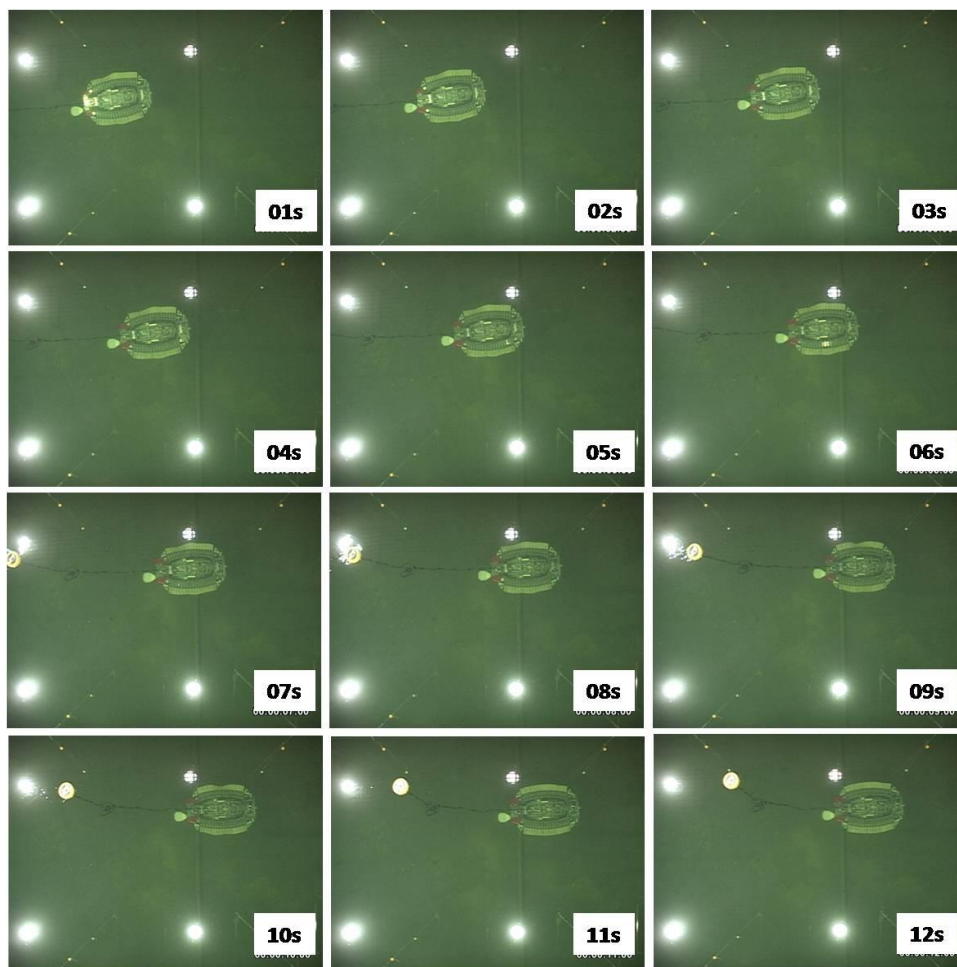


**Fig. 3.4 Images of the experimental video at different times of the translational motion before and after braking stage**

When the robot reached the stationary stage, the frequency of the fin was abruptly changed to zero; that is, no thrust condition was imposed. The robot slowed down due to the resistance by the water and finally stopped after travelling some distance. However, when the braking force was applied by adopting the same but opposite frequency to the side fins, it stopped very quickly and within very short distance. In both cases (translational motion and rotational motion), the robot showed excellent stopping capability. Fig 3.4 shows the snap shots at every second from the video of experiment of braking during translational motion. In this case the braking force was applied at 9<sup>th</sup> second; from the figure it is seen that the robot doesn't move from that point.

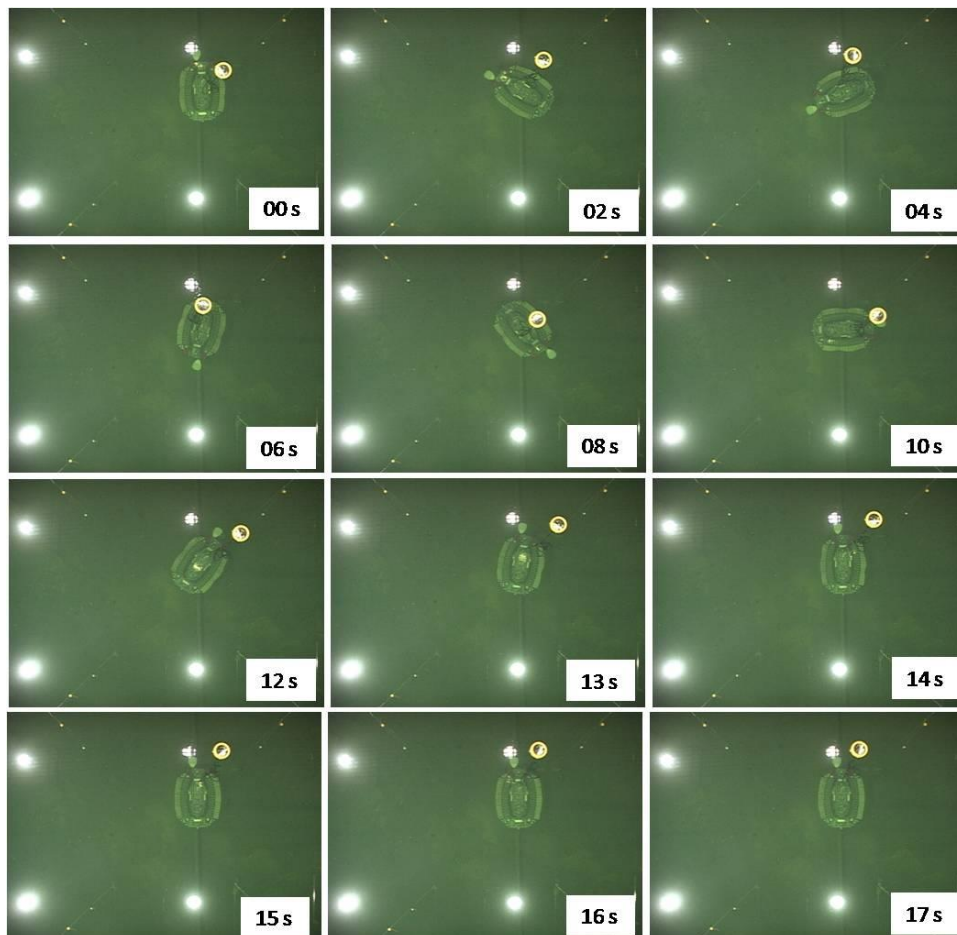


**Fig. 3.5 Images of the experimental video at different times of the rotational motion before and after braking stage**

In case of rotational motion, the snap shots were taken at 0, 2, 4, 6, 8, 10, 12, 13, 14, 15, 16 and 17 seconds, which is shown in Fig. 3.5. Here, the brake was imposed at around 14<sup>th</sup> second; in the figure it is seen that the model appears to be almost stopped at around 14<sup>th</sup> second.

The simulation study based on the equations of motion discussed in the section 3.3.2 was conducted under the similar condition as that of the experiment. Fig. 3.6 shows the comparison of experimental and simulation results in case of translational motion in terms of the  $x$ -direction movement with respect to time before braking state, under no thrust condition and after braking state. The green line represents the usual graph of frequency of 1 Hz ( $N_r = 1$  Hz,  $N_l = 1$  Hz) in translational motion. The no thrust condition ( $N_r = 0$  Hz,  $N_l = 0$  Hz) and the braking condition ( $N_r = -1$  Hz,  $N_l = -1$  Hz) were applied on 20<sup>th</sup> second. Though the data of the simulation and experiment were minimally edited for maintaining the similar condition, the results showed nice consistency in all cases.

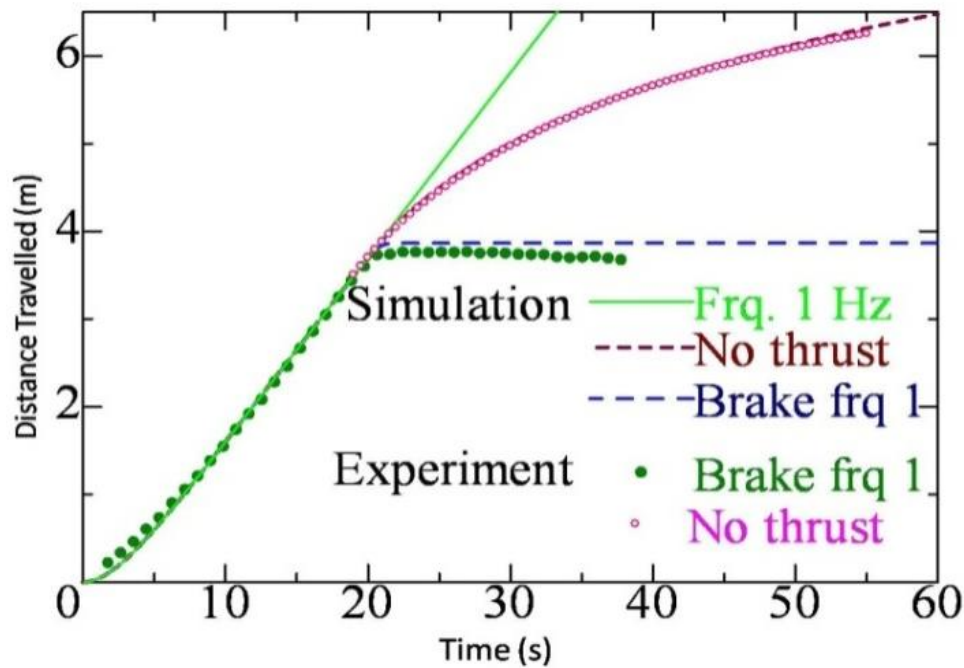


**Fig. 3.6 Comparison of experimental and simulation results in case of translational motion with and without brake**

Similar study was also conducted for rotational motion; however in this case the change in frequency was done on 10<sup>th</sup> second. Fig. 3.7 shows the comparison of experimental and simulation results of changing in heading angle of the robot for frequency 1 Hz ( $N_r = 1$  Hz,  $N_l = -1$  Hz), under thrust-less condition ( $N_r = 0$  Hz,  $N_l = 0$  Hz) and after braking condition ( $N_r = -1$  Hz,  $N_l = +1$  Hz). In this case also, the simulation and experiment results show good conformity. So, it is confirmed that the simulation result agrees well with the experimental observations for both motions.

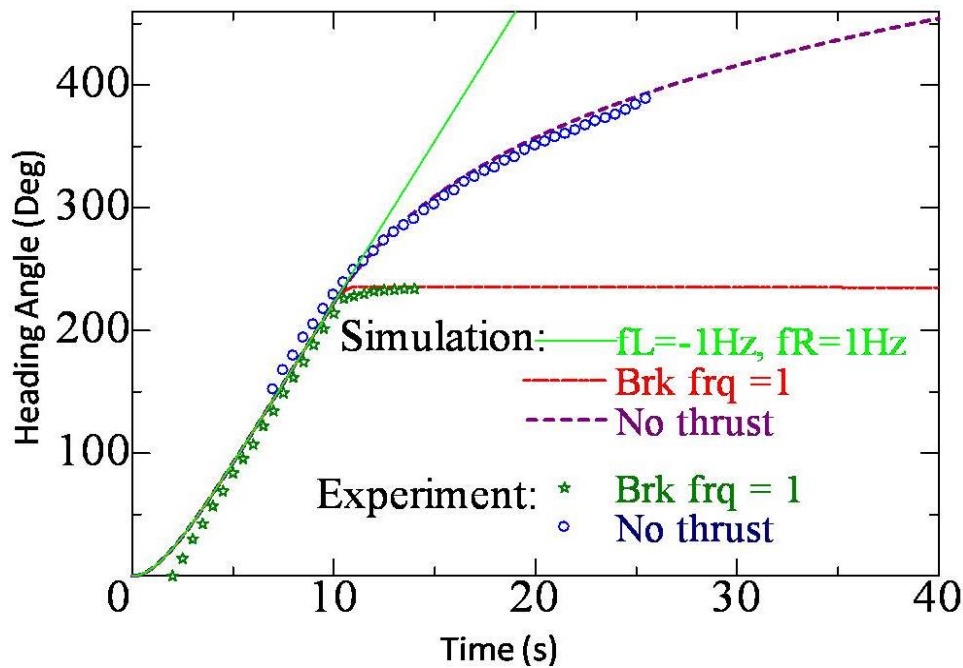


**Fig. 3.7 Comparison of experimental and simulation results of heading angle in case of rotational motion with and without brake**

From the above discussion, it can be concluded that the program could simulate the braking motion accurately for translational motion as well as rotational motion. For more investigation on the braking performance of the undulating fin propulsion system of the robot, the simulation study was extended for different braking frequencies which will be discussed in the next two sections.

### 3.4.2 Braking in Translational Motion

At first, the braking analysis of the translational motion is discussed based on the simulation results for different frequencies. For all the cases, the thrusting frequency of 1 Hz was applied in the starting stage. Higher starting frequency may need higher braking frequency to stop the robot.

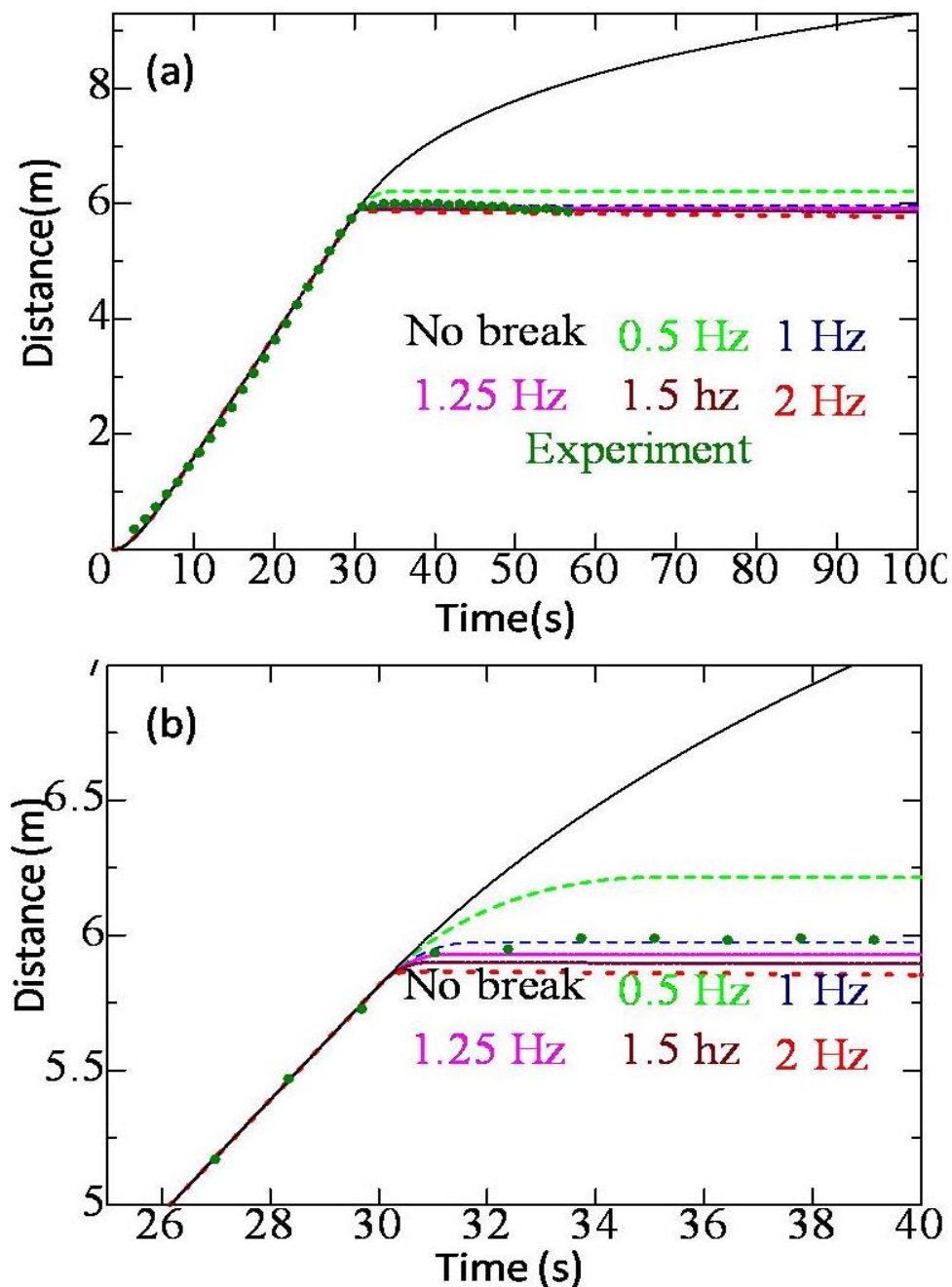


Fig. 3.8 (a) Travelled distance in translational motion with respect to time; (b) Enlarged view near the stopping point

After certain time (about 30 s in this case), the motion reached steady state (constant velocity), the braking frequencies, 0.5 Hz, 1.0 Hz, 1.25 Hz, 1.5 Hz and 2.0 Hz, were applied, respectively. When the velocity approached zero the braking frequency was switched off. Braking force was produced by imposing the reversed frequency of the corresponding undulating side fins. The travelled distance of the model in  $x$ -direction with respect to time is drawn in Fig. 3.8a. As the magnitude of the frequency before braking state was same (1 Hz) in all cases, the graph is also same in that area. The black solid line represents the no thrust condition where the frequency of zero was given from 30<sup>th</sup> second. The other graphs show the braking conditions by different braking frequencies applied at  $t = 30$  seconds. The changes of the trajectory in the  $x$ -direction due to brakes are clearly shown in the enlarged view near the stopping point (Fig. 3.8b).

From this figure, it is observed that the higher braking frequency can stop the model quickly, which is usual. For quantitative analysis, the numerical data of the stopping time and the travelled distance during the stopping motion were measured and shown in Table 3.1. The non-dimensional distance with respect to the length (140 cm) of the robot is also given. The higher frequencies needed lower time to stop the model and in those cases the robot also travelled shorter distances to stop. As for example, the model needs 5.17 seconds and it travelled 40.2 cm before stopping when the braking frequency of 0.5 was applied, on the other hand in case of braking frequency 2 the model took only 0.55 seconds and it moved only 5.34 cm from the brake application point to full-stop point. The braking performance of the squid-robot can be easily understood if its body length is considered. The actual length of the model is 140 cm; so it travelled only 1/26<sup>th</sup> of the body length to stop when the braking frequency of 2 Hz was applied. When the same braking frequency was applied, *i.e.* the starting frequency of 1 Hz up to the stopping point followed by -1 Hz braking frequency at the stopping point, then the model travelled 1/8.5<sup>th</sup> of its body length to stop. It was also confirmed that these data were consistent with the experimental results.

**Table 3.1 The braking frequency, the stopping time and the travelled distance before stop in case of translation motion**

Braking Frequency	Stopping Time(s)	Advanced distance(cm)	Non-dimensional*
0.5	5.169981	40.21835	0.287274
1.0	1.794836	16.20572	0.115730
1.25	1.239141	11.55574	0.082541
1.5	0.9073238	8.642387	0.061731
2.0	0.5460224	5.343938	0.038171

*\*distance was non-dimensionalized by the length of the robot (140 cm.)*

The  $x$ -direction velocity with respect to time is shown in Fig. 3.9 at no thrust condition and also under different braking conditions. When no thrust was applied, that is after a certain time (30 seconds) the zero frequency was given to the fins then the model slowed down unhurriedly because of the resistance of the body.

But, when the brake with some frequency was applied it stopped quickly; of course, higher braking frequencies stopped the model more quickly. The distribution of thrust and the drag of the model was also investigated which are shown in Fig. 3.10 and Fig. 3.11, respectively. In both the cases, the graphs of the simulation result moved along the expected way.

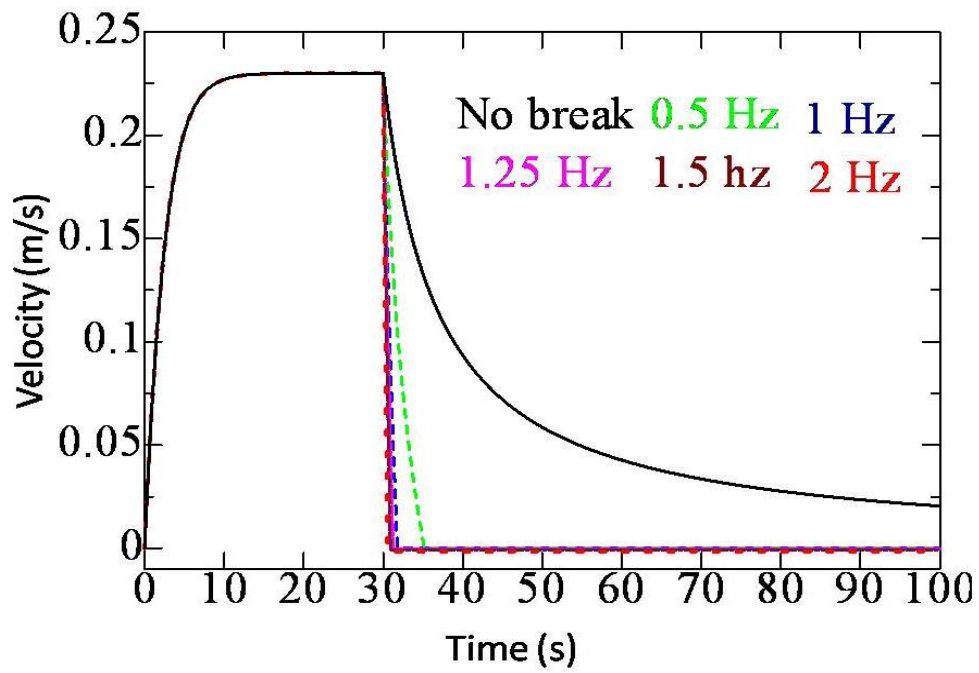


Fig. 3.9 Velocity with respect to time in translational motion

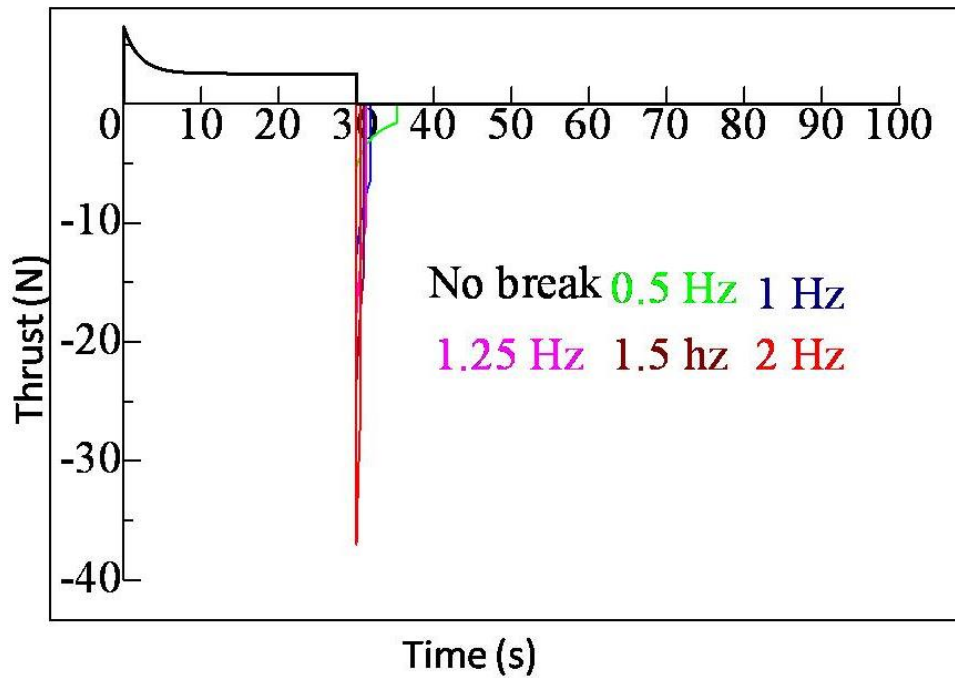
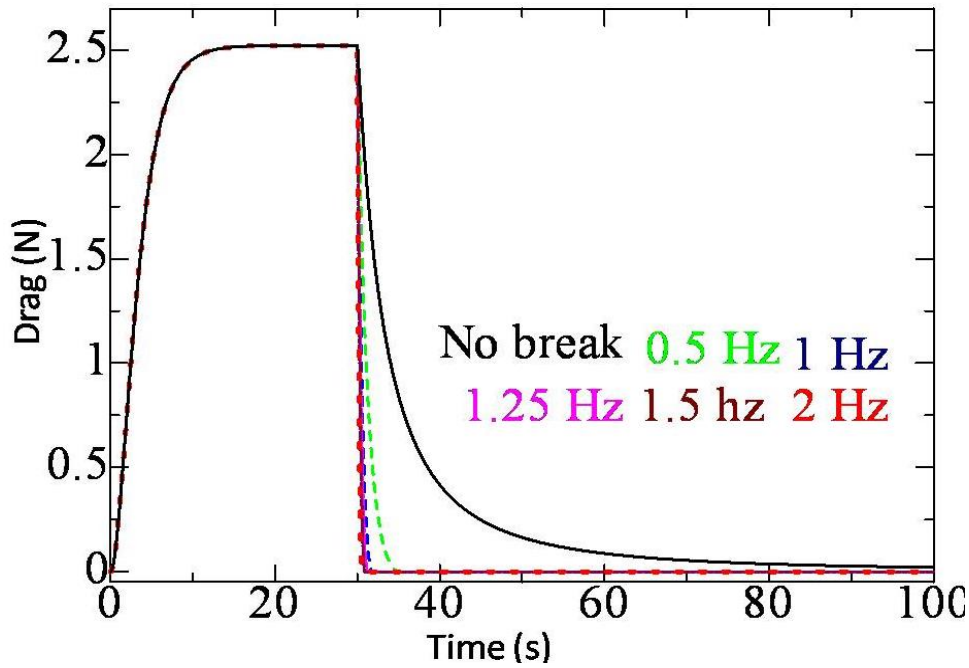


Fig.3.10 Thrust at different braking frequency in translational motion



**Fig.3.11 Drag at different braking frequency in translational motion**

### 3.4.3 Braking in Rotational Motion

Alike the translational motion, the ability of braking of the robot in rotational motion was also studied. The braking frequencies of 0.5 Hz, 1.0 Hz, 1.25 Hz, 1.5 Hz and 2.0 Hz were checked based on the theoretical discussion of the section (3.3.2). To make the rotational motion with respect to  $z$ -axis the frequency of +1 Hz and -1 Hz were given in the right and left fin respectively. For braking, the reversed frequencies were applied in the corresponding fins. For example, while applying the braking force of the frequency of 1.5 Hz, the frequency of -1.5 Hz and +1.5 Hz were given to the right and left fins respectively. In the rotational motion the model rotated with respect to  $z$ - axis without moving in  $x$  or  $y$  direction. After certain time (30 seconds) when the model became stable, the braking force of different frequencies were applied. The change in heading angle with respect to time is shown Fig. 3.12a. When no thrust was applied, *i.e.* the frequency of zero was maintained at 30 seconds, the rotation of the model became slower and stopped after long time. However when the brake forces were applied, the model stopped instantly. The enlarged view (Fig. 3.12b) near the braking point shows the clear change in angular position due to brake for different frequencies.

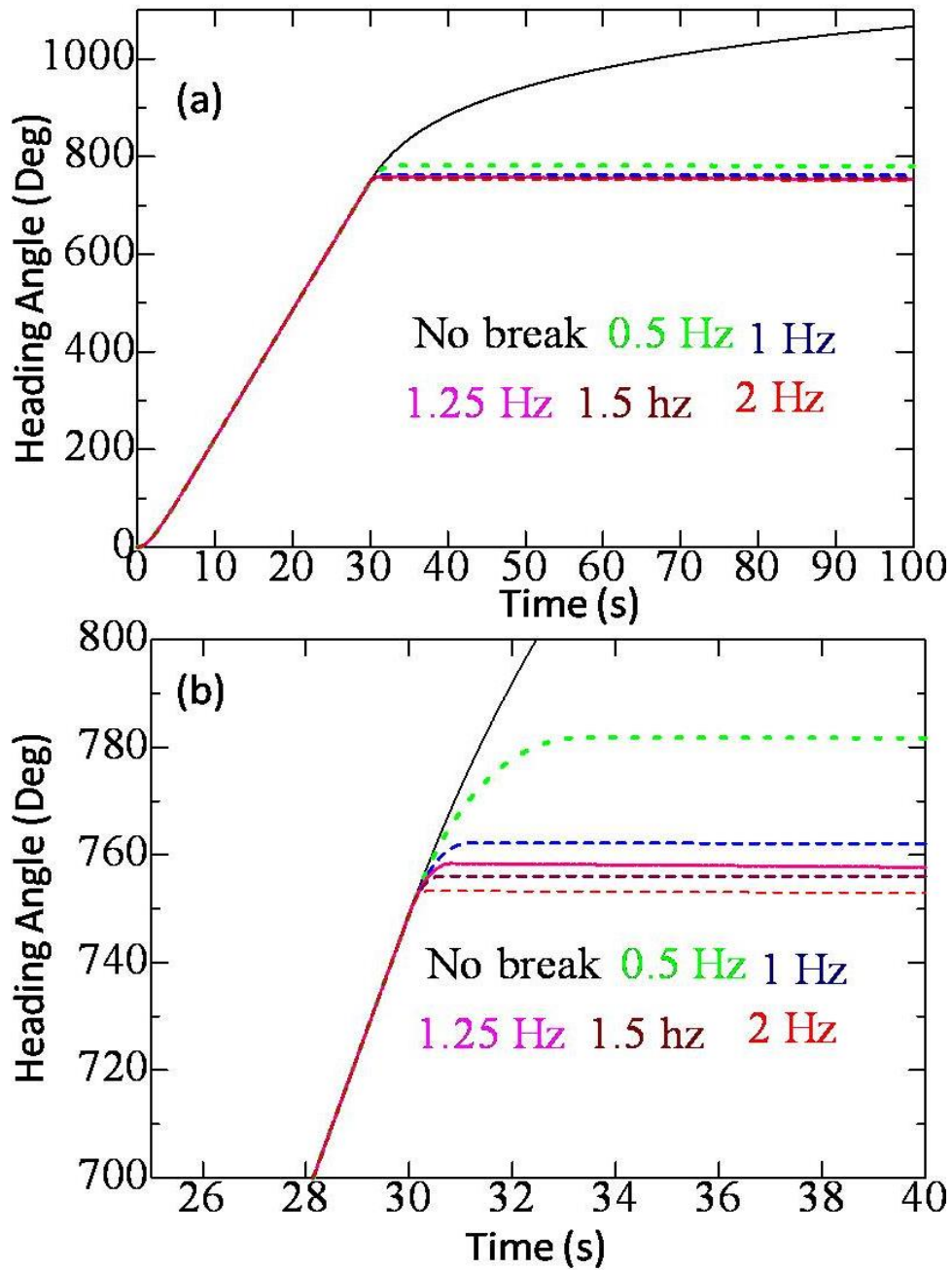


**Fig. 3.12 (a) Heading angle in rotational motion with respect to time; (b) Enlarged view near the stopping point**

For more observation, the numerical data of the stopping frequency, the stopping time and the change in heading angle during the brake are shown in Table 3.2. The non-dimensional values by 360 degree of the heading angle are also written. From this table it is also observed that the higher braking frequencies stopped the robot more quickly for rotational motion also. The experiment was conducted

for the braking frequency of 1 Hz; in that case the model took 13 seconds to stop after brake, which agrees well with the simulation result shown in the table. From these observations, it can be concluded that the braking efficiency of the robot is very high in case of rotation as well. In most of the cases, the robot took less than one second to stop and it travelled at best 10 degrees. Another point should be noted that the robot took less time to stop in rotational motion than in translational motion; this might be due to the difference in shape of the robot at front-tail and sides direction.

**Table 3.2. The braking frequency, the stopping time and the change in heading angle due to brake in case of the rotational motion**

Braking Frequency	Stopping Time	Change in heading angle due to brake (degree)	Change in heading angle due to brake (Non-dimensional*)
0.5	3.376776	32.79260	0.0910905
1.0	1.170884	12.66049	0.035168
1.25	0.8077374	8.851536	0.0245876
1.5	0.5906496	6.997125	0.0194364
2.0	0.3555546	3.501827	0.0097272

*\*Angle was non-dimensionalized by  $360^{\circ}$ .*

The change in angular velocity ( $r$ ) with respect to time due to different braking frequency is shown in Fig. 3.13. The zero velocity indicates the stopping condition of the model after applying brake. The moment in angular motion and the moment of inertia of the corresponding cases are also shown in Fig. 3.14 and Fig. 3.15 respectively. In these figures (Fig. 3.13-3.15), only the enlarged views are drawn for clear observation of the changes in graphs near the stopping point. The effect of braking in velocity and moment are clearly understood from the graphs. From the above discussion it is confirmed that the braking ability of the robot is outstanding in rotational motion also.

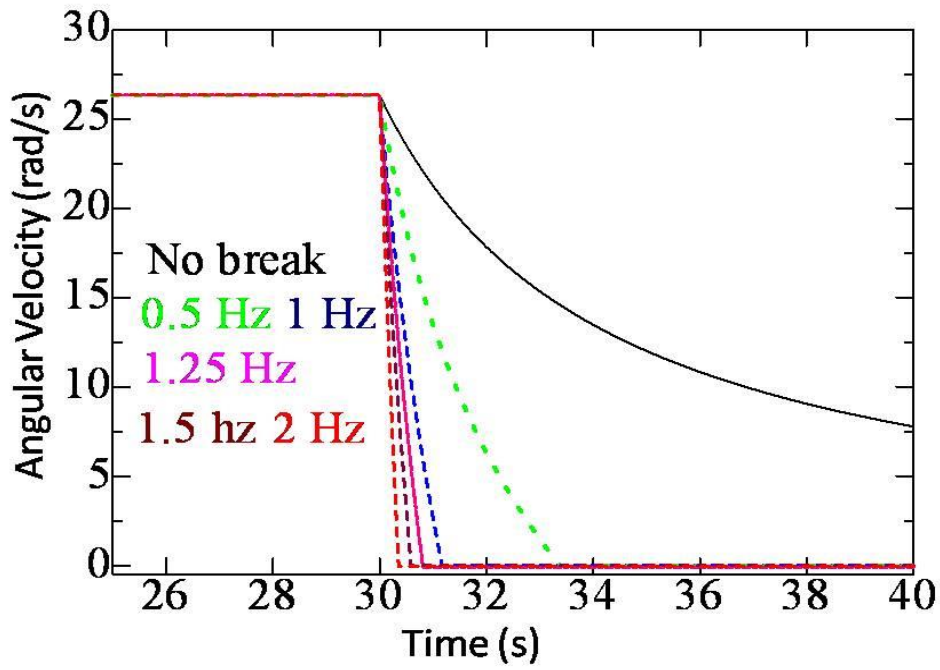


Fig. 3.13: The angular velocity with respect to time (enlarged view)

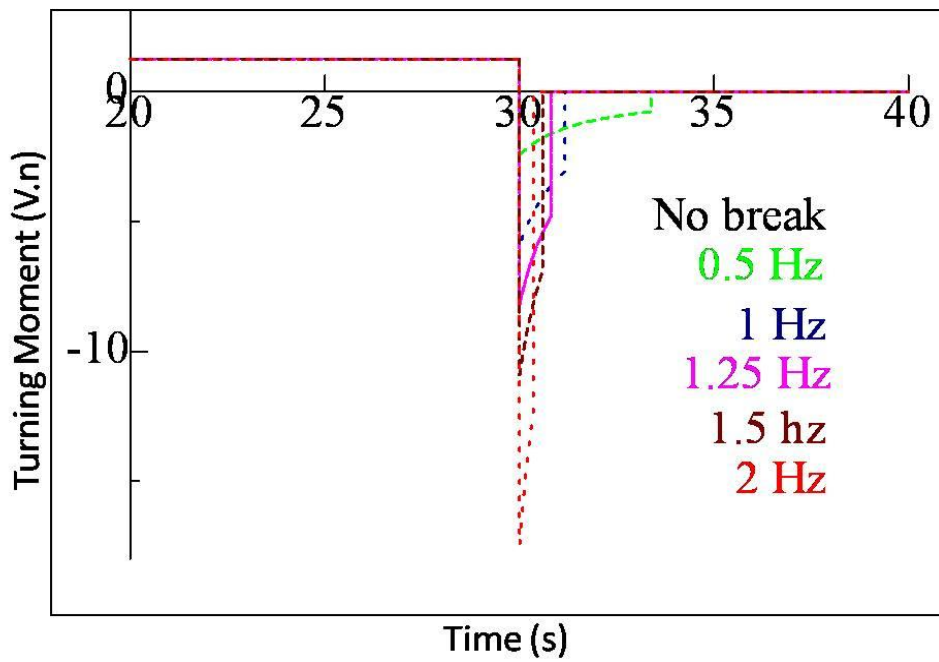
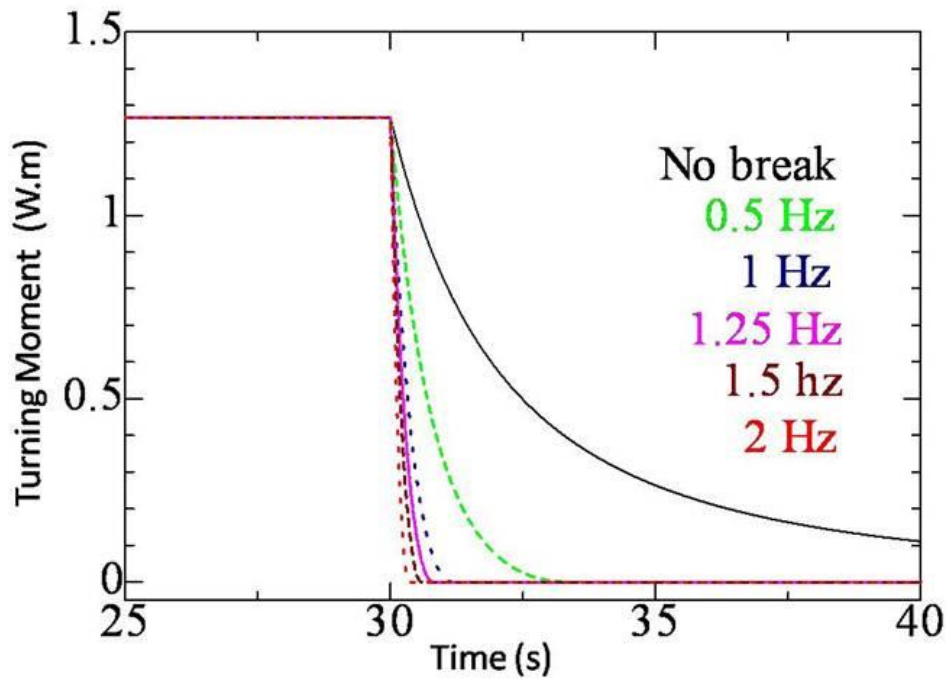


Fig. 3.14 The moment in angular motion with respect to time (enlarged view)



**Fig. 3.15 The moment of inertia with respect to time (enlarged view)**

Braking performance is very important issue in case of moving in an untraced topology and searching submersed item in the underwater area. From this study it is clear that the squid-robot is able to move in any direction on a 2D plane by combining the 1 DOF translational motion and rotational motion with the help of its highly capable braking system. If the braking ability is not so proficient then this work becomes difficult or somehow impossible. It should be noted that the robot can change the depth using caudal fins and also side fins (Rahman et al. 2013). Finally, from the above discussion it can be concluded that the braking ability of the undulating fin propulsion system of the squid-robot is sufficient enough for precise maneuverability in the underwater region.

### 3.5 Summery

The braking ability, an important benchmark of the propeller performance was investigated for a Biomimetic squid-like robot with two undulating side fins through experiment and simulation. In the free run experiment, the stopping motion by fin's stopping force and no thrust force for the

translational and rotational motions were investigated. The equation of motion was solved with the quasi-steady assumption and using the hydrodynamic forces found from the previous experiment and CFD computation. The simulation for different cases was carried out to observe the stopping ability of the undulating fin propulsion system. Good agreement between the experimental and simulation results was confirmed. From the results, it is confidently concluded that the undulating fins of the robot are capable of producing very large negative (stopping) thrust to stop itself instantly and within a very short distance. The braking performance undoubtedly proves the applicability of this underwater propulsion system in the exploration of complicated areas of oceans with unprecedented control and minimal disturbances to the underwater environment.

## **4. Chapter 4: Development of a Real Time Simulator Based on the Analysis of 6-DOF Motion of the Squid-Robot (Model-4)**

### **4.1 Preamble**

In this study, the motion of a squid-like underwater robot with two undulating side fins has been investigated through towing tank experiment and simulation of 6-DOF mathematical model in 3D space with the aim of developing a real time simulator. The comparison between simulation results and experimental results confirmed the accuracy of the simulation. The real time handling simulator was developed based on the mathematical model by using Open Dynamic Engine (ODE). It was confirmed that the robot in this simulator can move in the similar way as real robot's motion by the same control.

### **4.2 Introduction**

The swimming performance of Model-4 was demonstrated at Suma Aqua-Life Park with the real fishes (Fig. 1.6) and in Underwater Robot Festivals in Kobe (Fig. 1.7). The undulating side fins of the robot have been successfully used to make the straight line motions in surge, sway and heave directions and also to make the rotating motions in roll, pitch and yaw directions by changing the frequency and progressive wave direction or the vertical center of standing wave motion on the fin. Our robot swam freely in the environment similar to real coastal water with tidal current. Interestingly, the robot did not annoy the fishes – fishes were not scared swimming together with it and they did not attack it. It proved the environment friendliness of the robot. The robot also showed excellent maneuverability in swimming which is a fundamental ability of a robot in the underwater exploration. Because, during the operation the robot has to move around an unknown geometry in the underwater region to find some untraced items. The Model-4 could move in any direction in the 3D space and could stop suddenly upon braking and coming back by tracing same route. However, the precise maneuverability not only depends on the robot's capacity but also the ability of the operator. During

the experiments, due to operator's incompetence, at times difficulties arose in controlling the motion of the robot. Training for operators is required for real operation in the real coastal area. But the real model cannot be used always for training purpose. So the development of a real-time simulator was conducted in this study.

In this chapter, at first the 3-DOF circular motion and 3-DOF vertical motion using only side fins in addition to the motions used in usual operation (using caudal fins) were discussed using experiment and simulation results. Then as an example of 6-DOF motion, the spiral motion which is the combination of these two 3-DOF motions was discussed to check the 6-DOF mathematical model. Finally, using the equation of motion the real time simulator was developed with the help of Open Dynamic Engine (ODE).

### 4.3 Methodology

#### 4.3.1 Simulation

The study aimed to develop a real time simulator for the Model-4. 6-DOF equations of motion were solved using the mathematical model. The Hydrodynamic coefficients were obtained from the towing tank captive test and the numerical computation of fluid flow around the fins under the quasi steady assumption. The coordinate system is similar to that of sketched in Fig. 3.2 in Chapter 3. The body fixed coordinate system has its origin at the center of gravity and the body was symmetric with respect to  $xz$  and  $yz$  planes due to the neutral buoyancy of the tail fin. With respect to the  $xy$  plane, the body is a little bit asymmetric due to the small distance between gravity and buoyancy center and the shape of the servo motor unit of the real model. The relationship between space fixed coordinate system and body fixed coordinate system can be expressed as follows (Eq. 4.1 - Eq. 4.6) (Azuma and Nasu, 1977):

$$\frac{dX}{dt} = u \cdot \cos \theta \cos \psi + v \cdot (\sin \varphi \sin \theta \cos \psi - \cos \varphi \sin \psi) + w \cdot (\cos \varphi \sin \theta \cos \psi + \sin \varphi \sin \psi) \quad (4.1)$$

$$\frac{dY}{dt} = u \cdot \cos \theta \sin \psi + v \cdot (\sin \varphi \sin \theta \sin \psi + \cos \varphi \cos \psi) + w \cdot (\cos \varphi \sin \theta \sin \psi - \sin \varphi \cos \psi) \quad (4.2)$$

$$\frac{dZ}{dt} = -u \cdot \sin \theta + v \cdot \sin \varphi \cos \theta + w \cdot \cos \varphi \cos \theta \quad (4.3)$$

$$\frac{d\varphi}{dt} = p + q \cdot \sin \varphi \tan \theta + r \cdot \cos \varphi \tan \theta \quad (4.4)$$

$$\frac{d\theta}{dt} = q \cdot \cos \varphi - r \cdot \sin \varphi \quad (4.5)$$

$$\frac{d\psi}{dt} = q \cdot \sin \varphi / \cos \theta + r \cdot \cos \varphi / \cos \theta \quad (4.6)$$

Eq. 4.7 - Eq. 4.12 represent the 6-DOF equations of motion in body fixed coordinate system (Harvald, 1983). The first three equations represent the translation in  $x$ ,  $y$  and  $z$  directions respectively and the latter three represent the gyration around  $x$ ,  $y$  and  $z$  axes respectively. By solving these equations (Eq. 4.7-Eq. 4.12), the new gravity center position in space fixed coordinate system and Eulerian angles were found from the previous equations (Eq. 4.1-Eq. 4.6). The hydrodynamic forces were obtained based on quasi-steady assumption (similar as MMG model in ship maneuvering field (Bulletin of the Society of Naval Architects of Japan, 1985, Eng. 1986) from the model experiment and the CFD computation. More terms seem to be required for detailed consideration; but the following equations using state variables were used in this study for simplicity. The results were compared with experiment and validated in the section 4.4.

Equations of motion for translation:

$$x\text{-direction} \quad : (M + M_x) \frac{du}{dt} = F_x - (M + M_z) \cdot q \cdot w + (M + M_y) \cdot r \cdot v \quad (4.7)$$

$$y\text{-direction} : (M + M_y) \frac{dv}{dt} = F_y - (M + M_x) \cdot r \cdot u + (M + M_z) \cdot p \cdot w \quad (4.8)$$

$$z\text{-direction} : (M + M_z) \frac{dw}{dt} = F_z - (M + M_y) \cdot p \cdot v + (M + M_x) \cdot q \cdot u \quad (4.9)$$

Equation of motion for gyration:

$$\text{Around } x\text{-axis} : (I_{xx} + J_{xx}) \frac{dp}{dt} = T_x - ((I_{zz} + J_{zz}) - (I_{yy} + J_{yy})) \cdot q \cdot r \quad (4.10)$$

$$\text{Around } y\text{-axis} : (I_{yy} + J_{yy}) \frac{dq}{dt} = T_y - ((I_{xx} + J_{xx}) - (I_{zz} + J_{zz})) \cdot r \cdot p \quad (4.11)$$

$$\text{Around } z\text{-axis} : (I_{zz} + J_{zz}) \frac{dr}{dt} = T_z - ((I_{yy} + J_{yy}) - (I_{xx} + J_{xx})) \cdot p \cdot q \quad (4.12)$$

Since the body fixed coordinate system had its origin at the center of gravity and the shape of the body was symmetric then products of inertia were zero (Harvald, 1983) and some added products of inertia are ignored due to the small effect compared with other terms because the thickness in  $z$  direction was very small and almost symmetric with  $xy$  plane.

The forces,  $F_x$ ,  $F_y$ , and  $F_z$  and the moments  $T_x$ ,  $T_y$  and  $T_z$  were expressed as follows (Eq. 4.13 – Eq. 4.19):

$$F_x = f_{xpr} + f_{xpl} - C_x \cdot u \cdot |u| - |F_{tail}| \cdot \tan(\text{ang} \cdot \pi/180) \quad (4.13)$$

$$F_y = (f_{ypr} \cdot \cos(\theta_{cr} \cdot \pi/180) + f_{ypl} \cdot \cos(\theta_{cl} \cdot \pi/180)) - C_y \cdot v \cdot |v| - C_{yuv} |u|v \quad (4.14)$$

$$F_z = (|f_{ypr}| \cdot \sin(-\theta_{cr} \cdot \pi/180) + |f_{ypl}| \cdot \sin(-\theta_{cl} \cdot \pi/180)) + F_{tail} - C_z \cdot w \cdot |w| - C_{zuv} \cdot |u|w \quad (4.15)$$

$$T_x = (|f_{ypr}| \cdot \sin(-\theta_{cr} \cdot \pi/180) - |f_{ypl}| \cdot \sin(-\theta_{cl} \cdot \pi/180)) \cdot (bB/2) - C_{Mx} \cdot p \cdot |p| - BG \cdot \sin \varphi \cdot M \cdot g \quad (4.16)$$

$$T_y = F_{tail} \cdot (bL/2 + tL/4) + C_{zuw} u w \cdot (bL/4) - C_{My} \cdot q \cdot |q| - BG \cdot \sin \theta \cdot M \cdot g \quad (4.17)$$

$$T_z = (f_{xpr} - f_{xpl}) \cdot (bB/2 + fB) - C_{Mx} \cdot r \cdot |r| + 0.2 \cdot bL \cdot C_{yuv} u v \quad (4.18)$$

$$F_{tail} = -0.161 \cdot u^2 \cdot (\text{ang} + (180/\pi) \cdot \tan^{-1}(w/u)) \quad (4.19)$$

- Here,  $M$  : weight of the model (kg)
- $M_x, M_y, M_z$  : added mass in  $x, y, z$  directions (kg)
- $I_{xx}, I_{yy}, I_{zz}$  : moment of inertia along  $x, y, z$  ( $\text{kg} \cdot \text{m}^2$ )
- $J_{xx}, J_{yy}, J_{zz}$  : added moment of inertia along  $x, y, z$  ( $\text{kg} \cdot \text{m}^2$ )
- $F_x, F_y, F_z$  : total hydrodynamic force in  $x, y, z$  (N)
- $T_x, T_y, T_z$  : total hydrodynamic moment around  $x, y, z$  (N.m)
- $C_x, C_y, C_z$  : constant for drag force in  $x, y, z$  directions (Kg/m)
- $C_{Mx}, C_{My}, C_{Mz}$  : constant for drag moment (Kg)
- $C_{yuv}, C_{zuw}$  : coefficient for lift force due to drift angle and trim angle
- $BG$  : vertical distance between the center of buoyancy and the center of gravity (m)
- $\theta_{cr}, \theta_{cl}$  : center position of fin's angle
- $bB$  : body breadth (m)
- $fB$  : fin breadth (m)
- $bL$  : body length (m)
- $tL$  : tail length (m)
- $\text{ang}$  : tail fin angle (degree)

In this paper, the progressive wave motion of fin was used. The shape of the fin was expressed by the Eq. 4.20.

$$\theta = \theta_c + \theta_m \sin(2\pi kx - 2\pi Nt) \quad k = 1/\lambda, \lambda = fL \quad (4.20)$$

Here  $\theta_m$  is angle amplitude ( $0 < x < 1$ ), usually frequency  $N$  is positive; but in this paper,  $N$  was positive when the phase velocity of fin was in tail direction (making thrust in  $x$  positive direction).  $N = 0$  meant that the fin was flat without producing thrust.

The moments of inertia were calculated by using mass distribution. The added masses and added moments of inertia were obtained by using Hess-Smith method (Cebeci, 1999). The values are summarized in the Table 4.1.

**Table 4.1: Added mass, moment of inertia and added moment of inertia**

$M_x$	5.957	$I_{xx}$	2.278	$J_{xx}$	8.78
$M_y$	14.552	$I_{yy}$	7.996	$J_{yy}$	27.988
$M_z$	397.6	$I_{zz}$	10.133	$J_{zz}$	1.438

When the  $x$ -direction advance velocity at fin's representative point was obtained, the thrust of  $x$ -direction could be calculated from the  $J_x - K_x$  relations of the previous experimental and numerical studies. The advance coefficient and the  $x$ -direction thrust produced by the left and right side fins can be found from the following formulas (Eq. 4.21 - Eq. 4.23):

$$J_{xS} = \frac{\left(u \pm \left(\frac{bB}{2} + fB\right) \cdot r\right)}{(N_S \cdot fL)} \quad (4.21)$$

$$K_{xS} = 0.5 \left(0.0132J_{xS}^2 - 0.015J_{xS} + 0.005\right) \cdot \left(\frac{\theta_{mS}}{30}\right)^2 \quad (4.22)$$

$$f_{xpS} = \rho \cdot K_{xS} \cdot N_S^2 \cdot fL^4 \quad (4.23)$$

The y-directional forces were calculated in similar way by using the following formulas (Eq. 4.24 – Eq. 4.25):

$$K_{yS} = 2.67 \cdot (\mp 0.0009365 J_{xS}^2 \mp 0.0003031 J_{xS} \pm 0.0008275) \cdot \left( \frac{\theta_{ms}}{30} \right)^2 \quad (4.24)$$

$$f_{ypS} = \rho \cdot K_{yS} \cdot N_s^2 \cdot fL^4 \quad (4.25)$$

(Note: In Eq. 4.21- Eq.4. 25, the letter *S* in the suffix was replaced by *r* or *l* for right or left fin respectively. Also the upper and lower sign of the double sign was considered for right fin and left fin respectively)

Here,  $J_{xl}, J_{xr}$  : Advance coefficient for left and right fin respectively

$K_{xl}, k_{xr}$  and  $k_{yl}, k_{yr}$  : Thrust coefficients in *x* and *y* direction respectively

$f_{xpl}, f_{xpr}$  and  $f_{ypl}, f_{ypr}$  : Thrust forces in *x* and *y* direction respectively

$N_l, N_r$  : Frequencies

$\theta_{ml}, \theta_{mr}$  : Maximum fin angle of left and right fin respectively

The coefficient in case of translational and the rotational motion were considered as follows:

$$\left. \begin{aligned} C_x &= 47.70 \\ C_y &= 43.86 \\ C_z &= 2.11 \times 100 \\ C_\phi &= 14 \times 2.11 \times bB^2 \\ C_\theta &= 40 \times 2.11 \times bL^2 \\ C_\psi &= 6.00 \end{aligned} \right\} \quad (4.26)$$

The equations of motion were solved by the fourth order Runge-Kutta Method.

### 4.3.2 Formation of Circular and Vertical Motions

The circular motion was attained by applying variable thrusts into two undulating side fins of the robot. This can be done by controlling the phase difference of undulations between both side fins or by setting the same frequency and variable fin angles to the side fins or by applying variable

frequencies to the side fins and keeping same fin angle to both fins. In this study, the latter case was considered for convenience. The frequency of 1 Hz and 0.5 Hz were applied to the right and left fins respectively and the maximum fin angle was kept at 45 degree for both fins (Fig. 4.1)

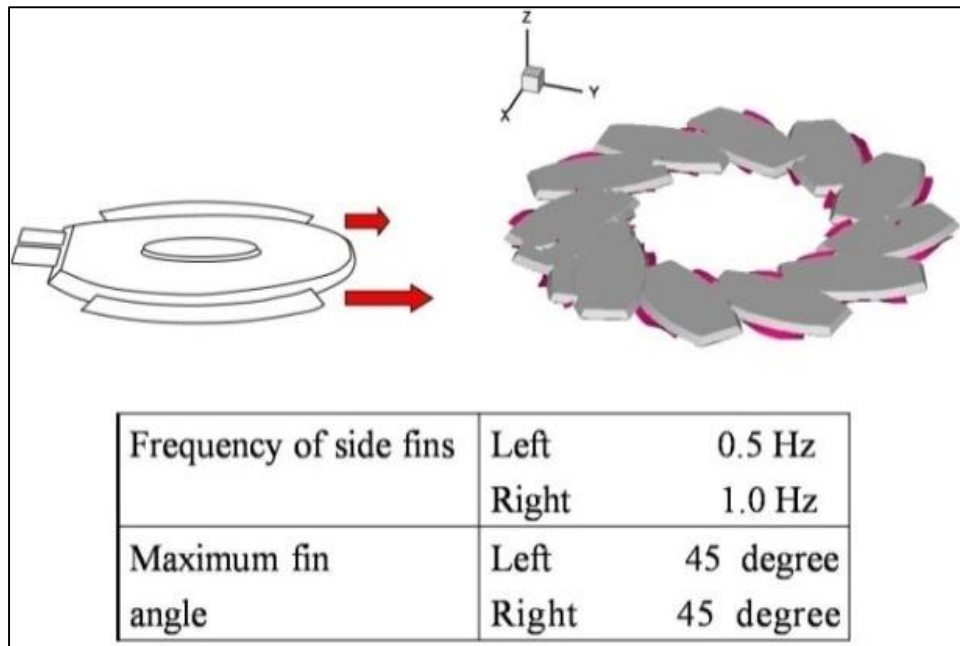


**Fig. 4.1 Sketch of the principal of circular motion**

For simplicity, only the positive frequency was applied for moving the robot in forward direction and the negative frequency for moving the robot in reverse direction. A simulation was also conducted under the same conditions.

On the other hand, the vertical motion can be achieved by using caudal fins and/or side fins. In this study, the side fins were used to change the depth of the model. The center of oscillation of the side fins was shifted up or down from the horizontal position to move the model down or up respectively. The center of oscillation was shifted to 30 degree up and 30 degree down and the frequency of 1 Hz was applied to both the fins. The technique of shifting the center of oscillation of the side fins is clearly sketched in Fig. 4.2.

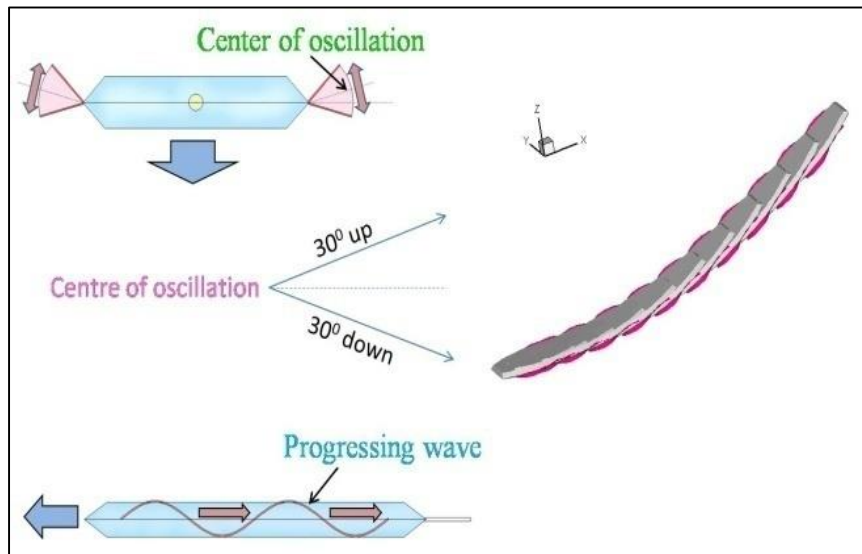


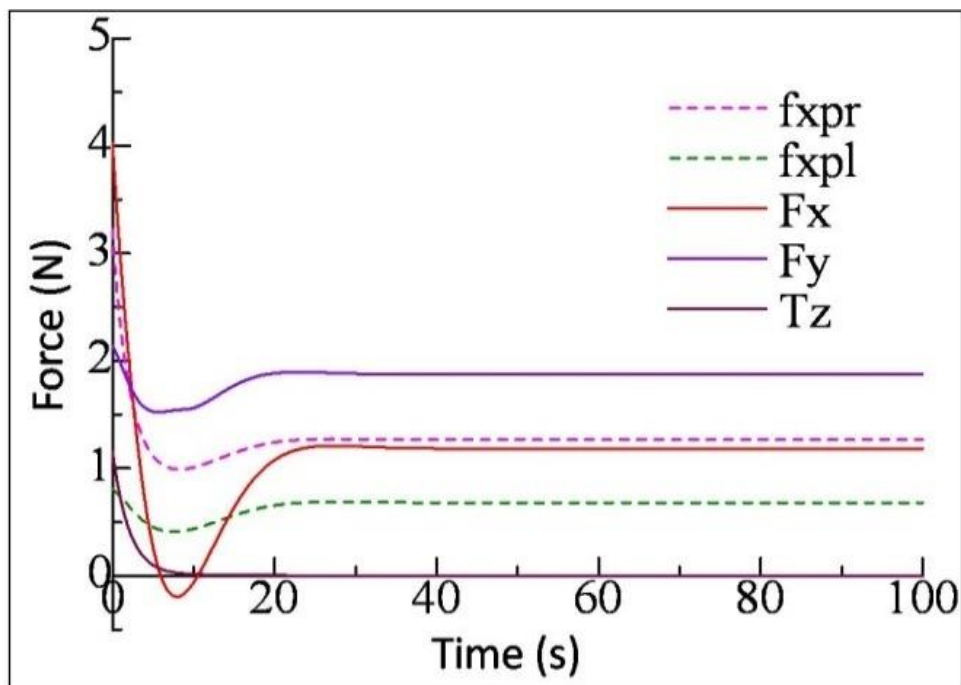
**Fig. 4.2 Sketch of the principal of vertical motion by shifting the center of oscillation of the side fins**

#### **4.4 Results and Discussion**

The main goal of this study was to investigate the 6-DOF motion of a squid-like robot in order to develop the real time simulator. In the previous chapter, the 1-DOF translational motion in  $x$  direction and rotational motion at one point were studied for investigating the braking ability of the undulating fin propulsion system of the robot. In this study, to investigate the more complex mathematical model, the 6-DOF model was tested and compared with experiment. At first, the 3-DOF circular motion in  $XY$  plane and the 3-DOF vertical motion in  $XZ$  plane were investigated through experiment and simulation. Then the result of spiral motion, which was found by combining the circular motion and vertical motion was discussed as an instance of 6-DOF motion. In the following sections, the 3-DOF circular motion, the vertical motion, the 6-DOF spiral motion and finally the development of real time simulator will be discussed simultaneously by means of experimental and simulation results.

#### 4.4.1 3-DOF Circular Motion

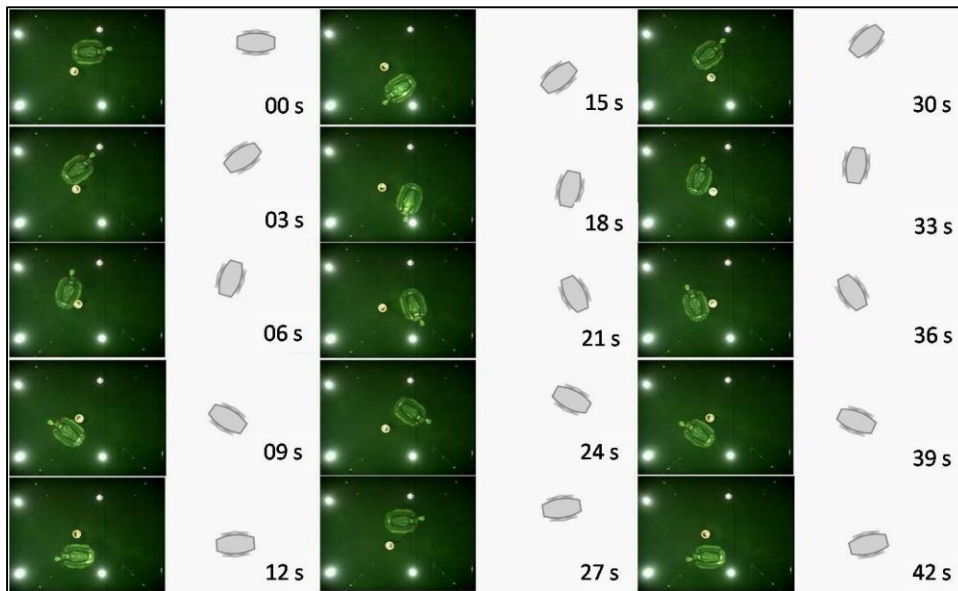
As discussed in the Section 4.3.2, in this study the circular motion was attained by applying the frequency of 1 Hz and 0.5 Hz to the right and left fins respectively and keeping the fin angle 45 degree to both fins. The robot took some times to make static circular movement after application of variable frequencies to the fins. The robot attained steady state motion when centrifugal acceleration force was balanced by the hydrodynamic force.



**Fig. 4.3 Time history of the forces in circular motion**

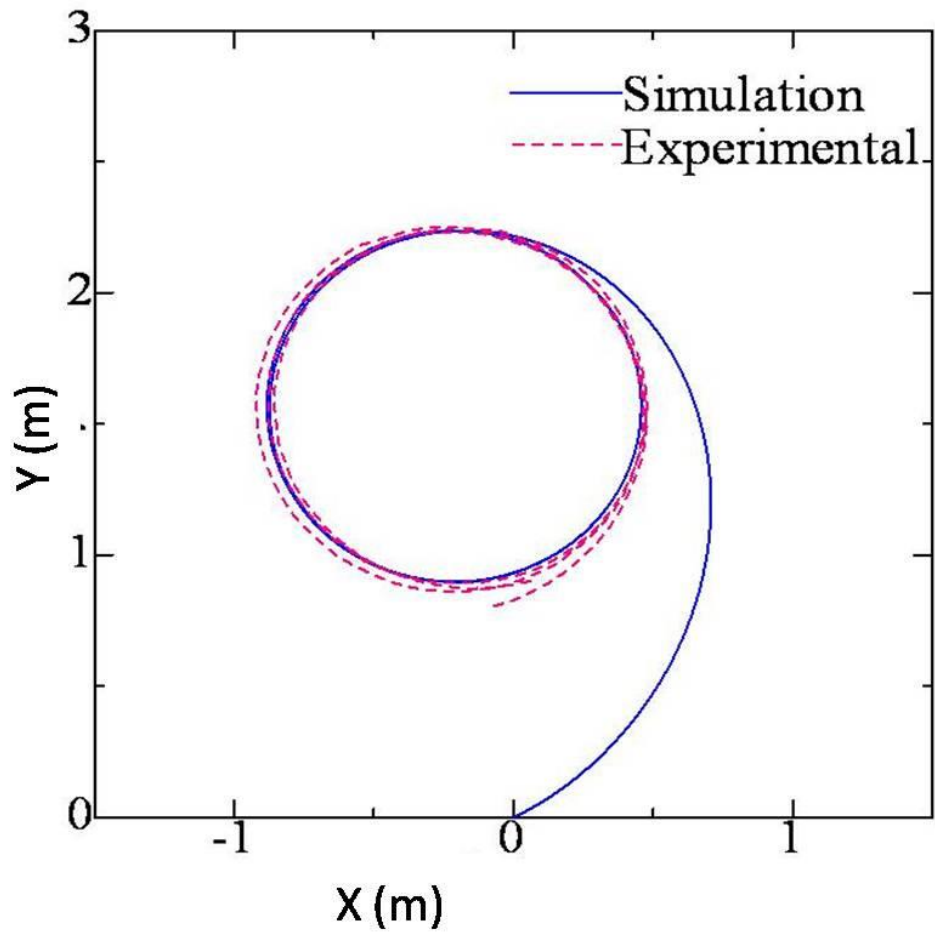
Fig. 4.3 shows the graph of time history of the forces. The thrust force produced by left and right fin and the total hydrodynamic forces in x and y direction are shown. In this figure, it is seen that  $F_x$  gives some negative value before the steady state region; this has happened because of the large drag that had originated in that region. The total hydrodynamic moment around z-axis is also shown, which is zero in the steady state region.

Fig. 4.4 shows snap shots of the video at every 3 seconds intervals of the experiment as well as the simulation for the circular motion. From this figure it is observed that the robots in the movie are in similar motion which verified the accuracy of the simulation.



**Fig. 4.4 Comparison of simulation result and experimental film in case of circular motion**

The top view of the trajectory of the center of gravity is shown in Fig.4.5. The simulation result is drawn from the initial stage whereas the experimental result is drawn only at the steady state condition due to limited camera range. It is noted that in this particular case the diameter of the circle is 1.34m, which is almost similar to the body length of the robot. Fig. 4.6 shows the graph of time history of heading angle; In this case also the simulation result agrees well with the experimental data. From the above figures, it can be noticed that our simulation could predict the 3-DOF circular motion accurately.



**Fig. 4.5 Trace of the centre of gravity of the models in circular motion**

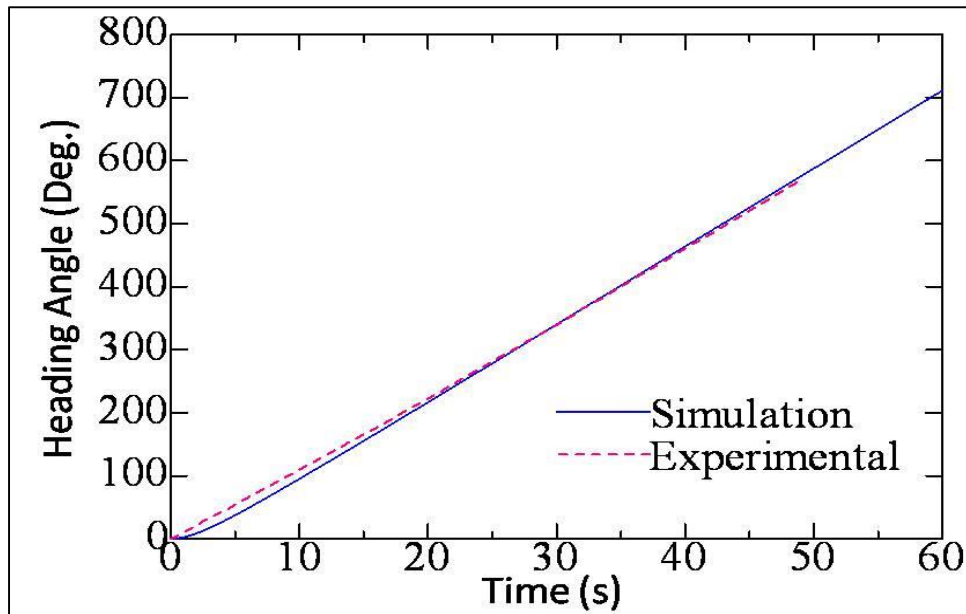


**Fig. 4.6 Time history of the heading angle in circular motion**

#### **4.4.2 3-DOF Vertical Motion**

The 3-DOF vertical motion in  $XZ$  plane leading to the change of depth was also investigated. Usually caudal fins are used for this purpose, and it works well when the robot is only in vertical motion. However, in the experiment of spiral motion, it was observed that when the robot had to move along a small circle then it made some unexpected movement. This had happened because of the flat-shape of the caudal fin, which will be discussed in detail in the next section.

The experimental and simulation results of the trajectories of the center of gravity of the robot in case of shifting the center of oscillation 30 degree up and 30 degree down are shown in Fig. 4.7. The time series of nose down angle of the body in case of 30 degree down is also shown in Fig. 4.8. In both of the figures, the simulation results agree well with the experimental data. From the above discussion, it can be concluded that our program is able to simulate 3-DOF circular and vertical motions accurately.

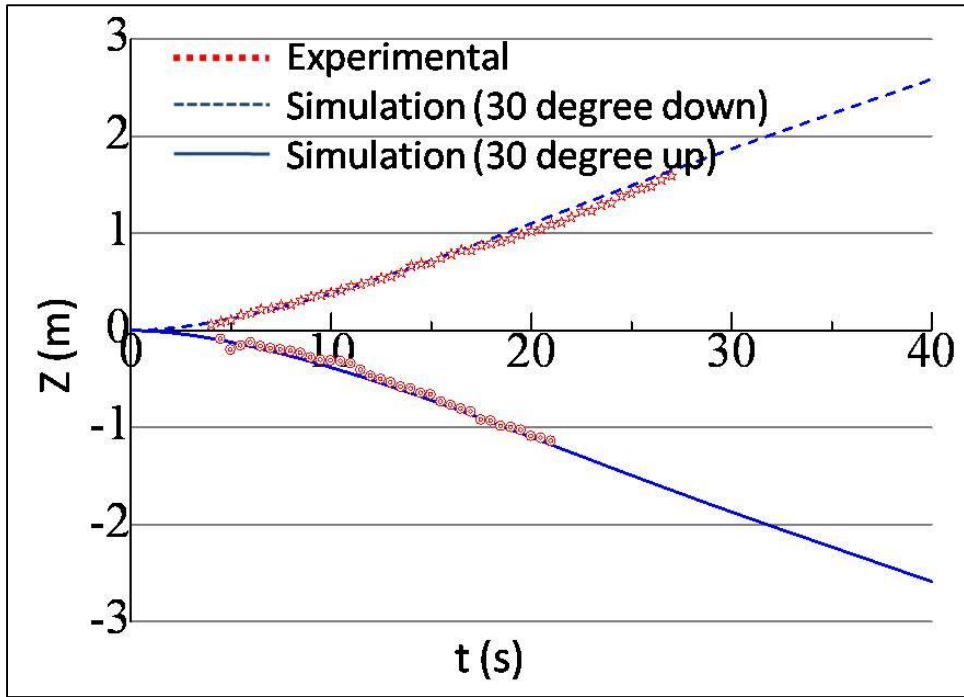


Fig. 4.7 Time history of the models in  $z$ -direction for vertical motion at +30 degree and -30 degree change of center of oscillation

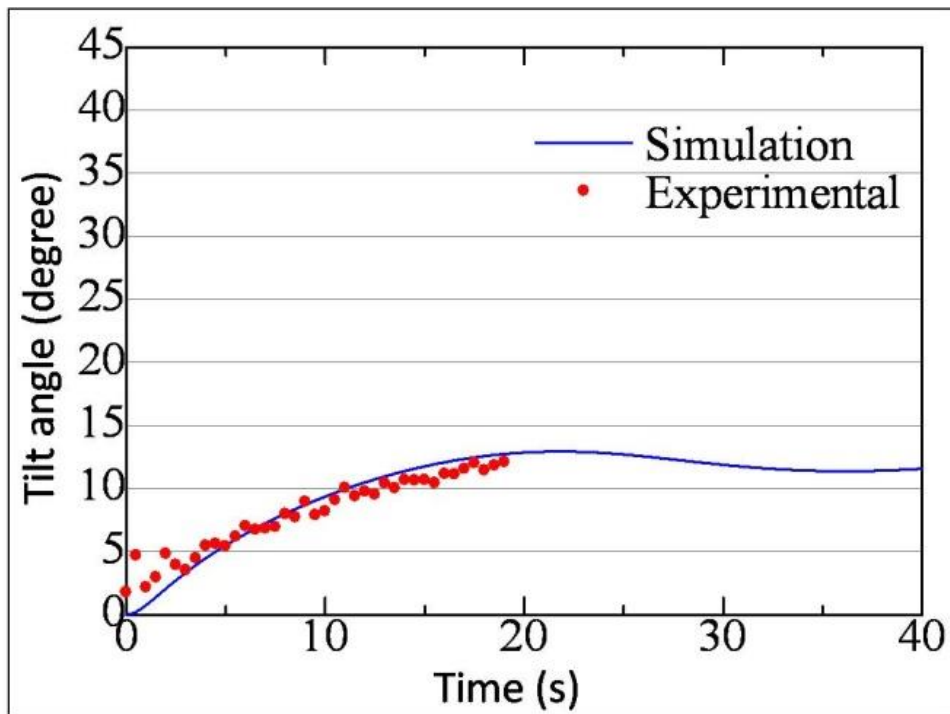
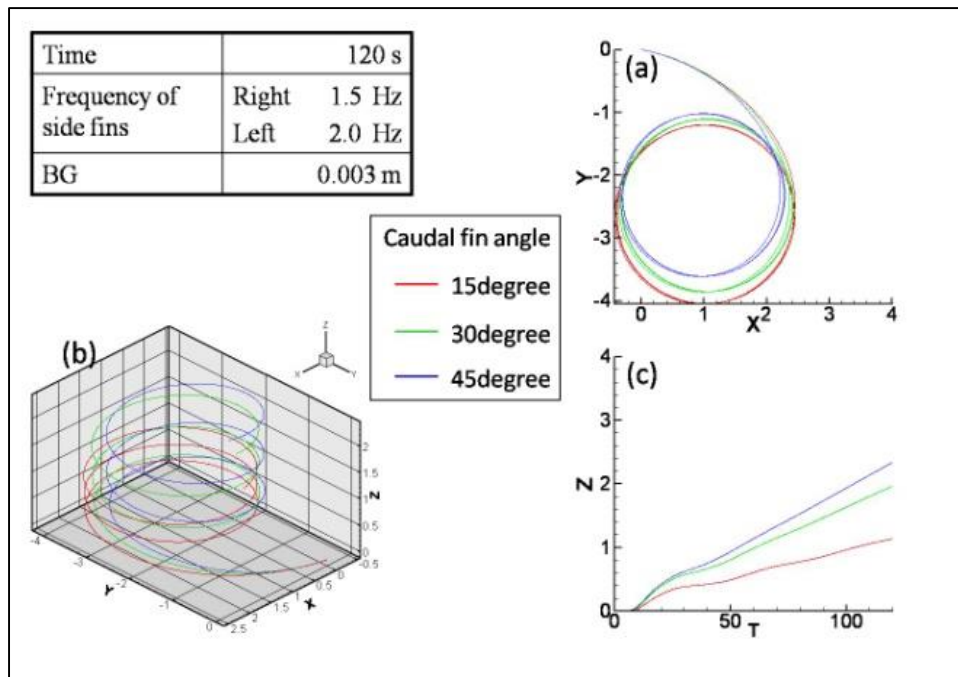


Fig. 4.8 Time history of the tilt angle for vertical motion

#### 4.4.3 Spiral Motion using Side Fin and Caudal Fin

After successful completion of the 3-DOF motions in two dimensional space, the computation was extended to 6-DOF motion in three dimensional space. In this case, the spiral motion was investigated as an example of 6-DOF motion. This motion is a combination of  $x$  direction movement (surge),  $y$  direction movement (sway),  $z$  direction movement (heave), rotation about  $x$ - axis (roll), rotation about  $y$ - axis (pitch) and rotation about  $z$ - axis (yaw). So it was treated as a good example to verify the accuracy of simulation result for 6-DOF motion. Spiral motion was obtained by combining the circular and vertical motions.



**Fig. 4.9 Spiral motion where caudal fins were used to change of depth**

As mentioned in the previous sections, the circular motion was created by giving dissimilar frequencies in the side fins; on the other hand the vertical motion can be found by two ways: using caudal fins and by shifting the center of oscillation of the side fins. In this section, the first case was considered for vertical motion. Fig. 4.9 shows some simulation results of spiral motion where the

caudal fins were used for changing the depth. The table tells about the parameters used in the particular computation. The Fig. 4.9a shows the trajectory of the center of gravity in the  $XY$ - plane, Fig. 4.9b shows the trajectory in the 3D space and Fig. 4.9c shows the time series of the distance of  $z$ -direction.

The study was also done in different conditions by changing the parameters and the caudal fin angles. It was observed that when the caudal fin angle increases, the circle drawn by the model became smaller and the distance in the  $z$ -direction increased. The distance in the  $z$ -direction was also increased when the value on  $BG$  decreases keeping the other parameter same.

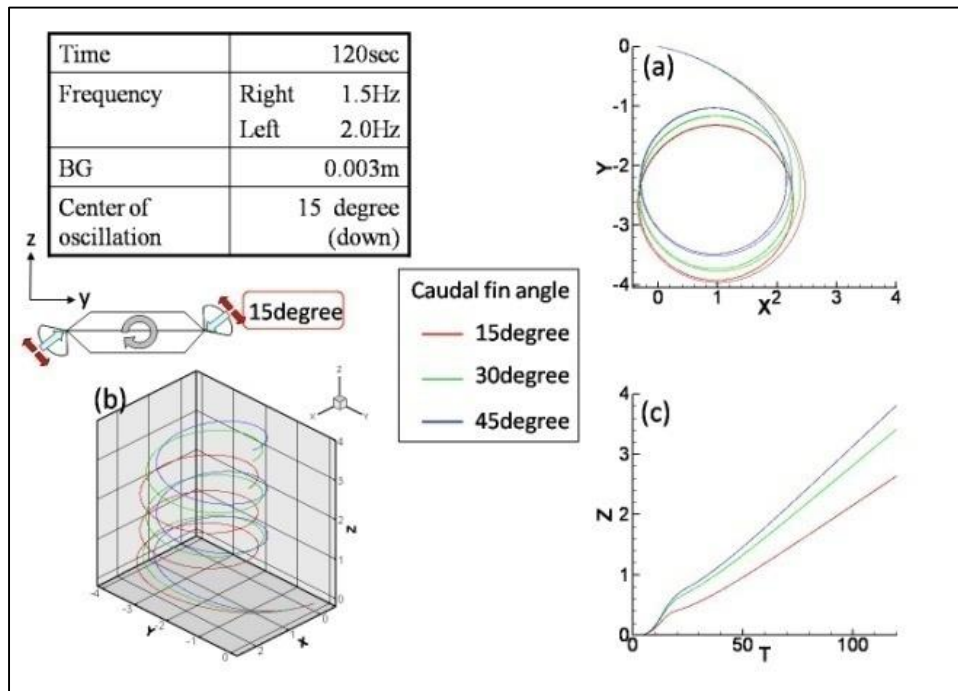


**Fig. 4.10 Spiral motion where caudal fins and the side fins were used to change of depth**

During the experiment it was found that when the frequency 1 Hz and 2 Hz were applied in the left and right fins and the caudal fin was rotated to 30 degree then the robot made an unexpected movement. The model couldn't go up in spite of attempting to go up. It was realized that, the caudal fin couldn't work properly when the diameter of the trace of the center of gravity was less than the

body length (like the case drawn in Fig. 4.5) of the robot. Actually, when the difference of the frequencies of the side fins increased the robot moved along small circle. In that case, the drift angle at the stern also increased and the tail of the robot moved very fast than its head. As a result in that case the caudal fins couldn't do its duty properly in moving the robot up or down because of its flat shape. This phenomenon was also predicted by the present simulation. Better result was found when the center of oscillation of the side fins was shifted to change the depth (Fig. 4.10). It was also confirmed that the simulation results were qualitatively corresponding to the movie of free run test.

#### 4.4.4 Spiral Motion using Only Side Fin

To overcome this limitation of caudal fin the second technique, shifting the center of oscillation of the side fins was used for changing the depth of the robot. In the rest part of this study, this technique will be considered in changing the depth. The spiral motion without caudal fins was created by combining the circular motion and vertical motion which is described in Fig. 4.11.

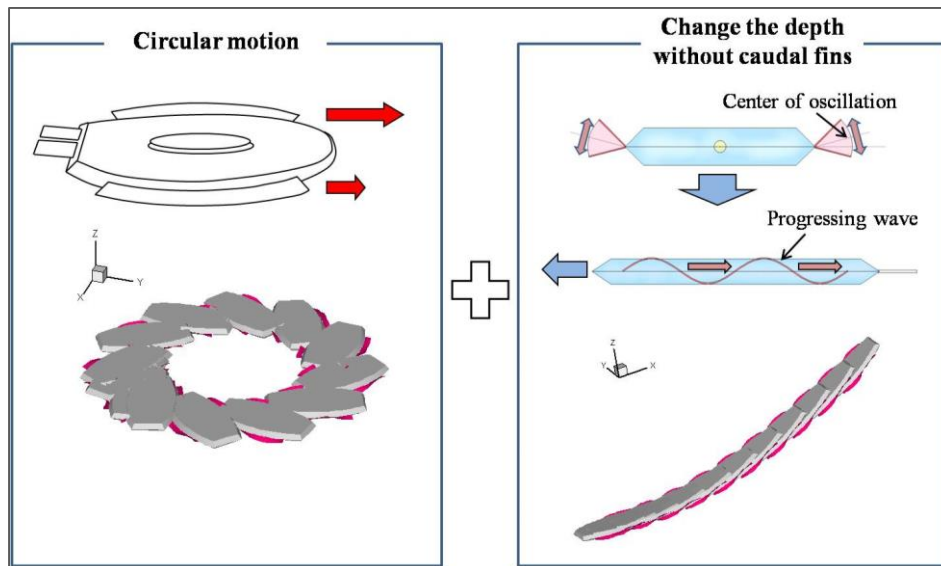


**Fig. 4.11 Formation of spiral motion without caudal fins**

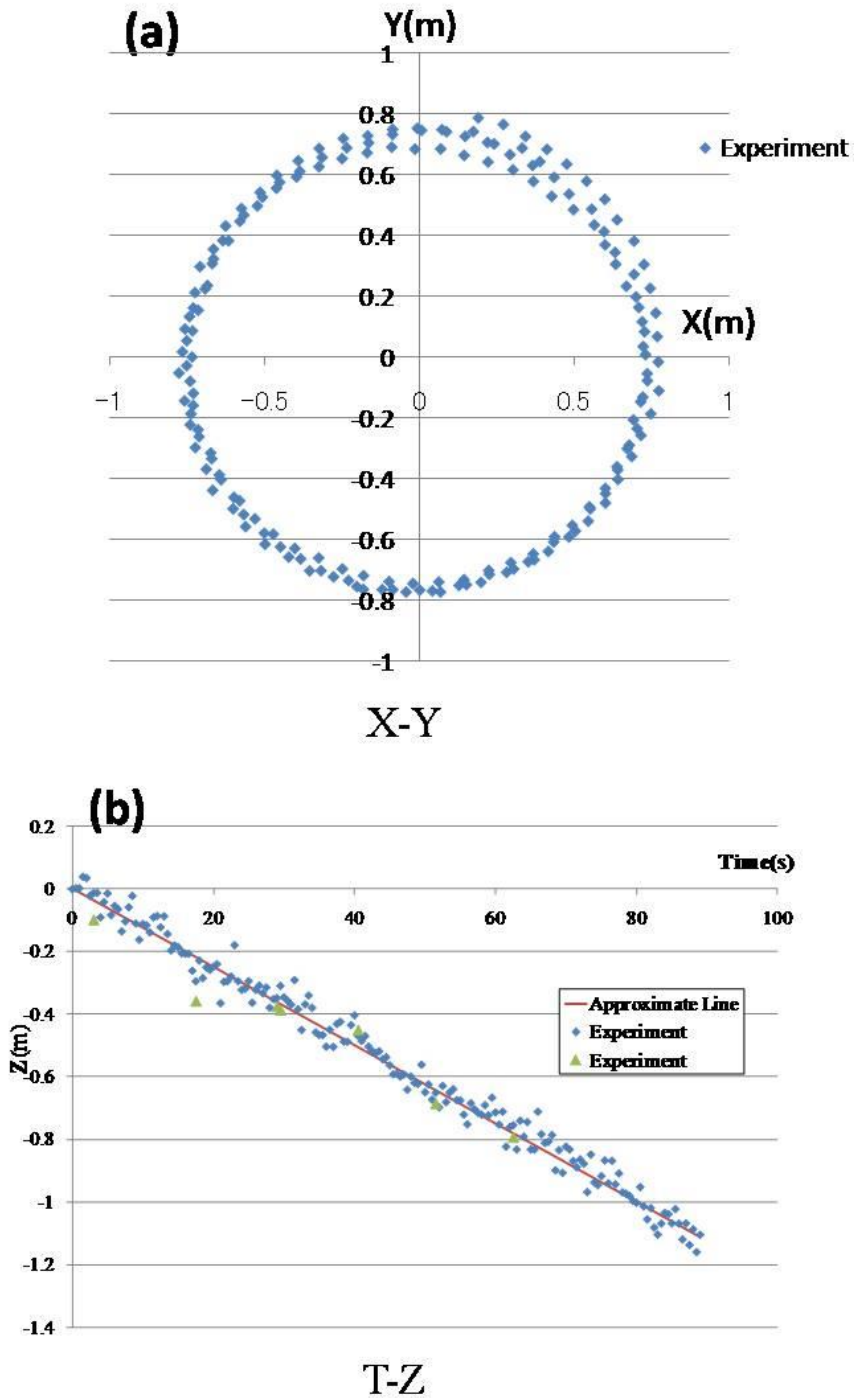
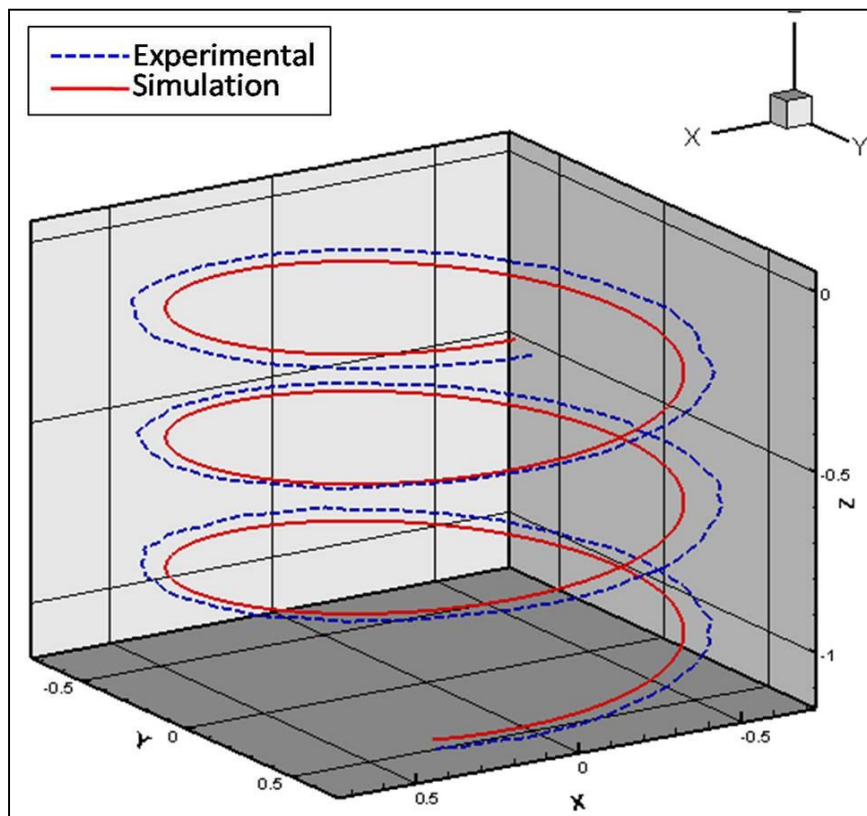


**Fig. 4.12 Experimental result of spiral motion without caudal fins (a) Trajectory of the centre of gravity, (b) Distance in z-direction**

In this case, the frequencies of 1 Hz. and 0.5 Hz. were applied to the right and left fin respectively. The maximum fin angle was set to 45 degree and the displacement angle from the horizontal position

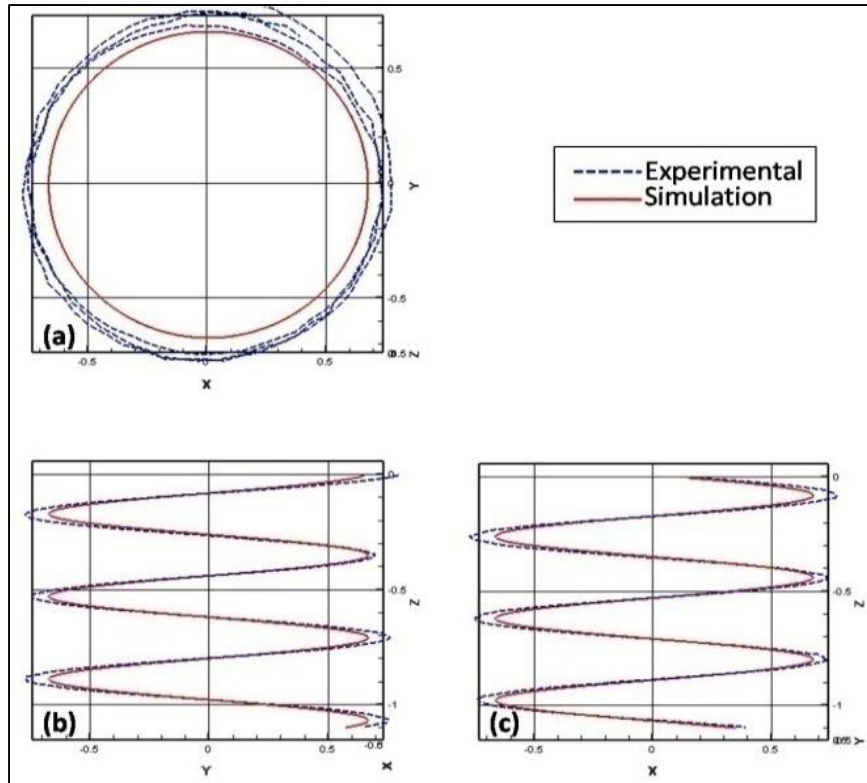
was set to +15 degree (up) for both fins. The experimental results of the trajectory of the center of gravity (top view) and the time series of distance in  $z$ -direction are shown in Fig. 4.12. Since this moving distance of  $Z$ -direction was estimated from top view, so these data are scattered. But in reality the robot must be descending smoothly. So this could be approximated by this red line and we used this approximated line to compare with simulation.

The simulation was also conducted in the same condition and the equations of motion used in the simulation were discussed in the section 4.3.1. The comparison of three dimensional trajectory of the centre of gravity during the spiral motion is shown in Fig. 4.13.



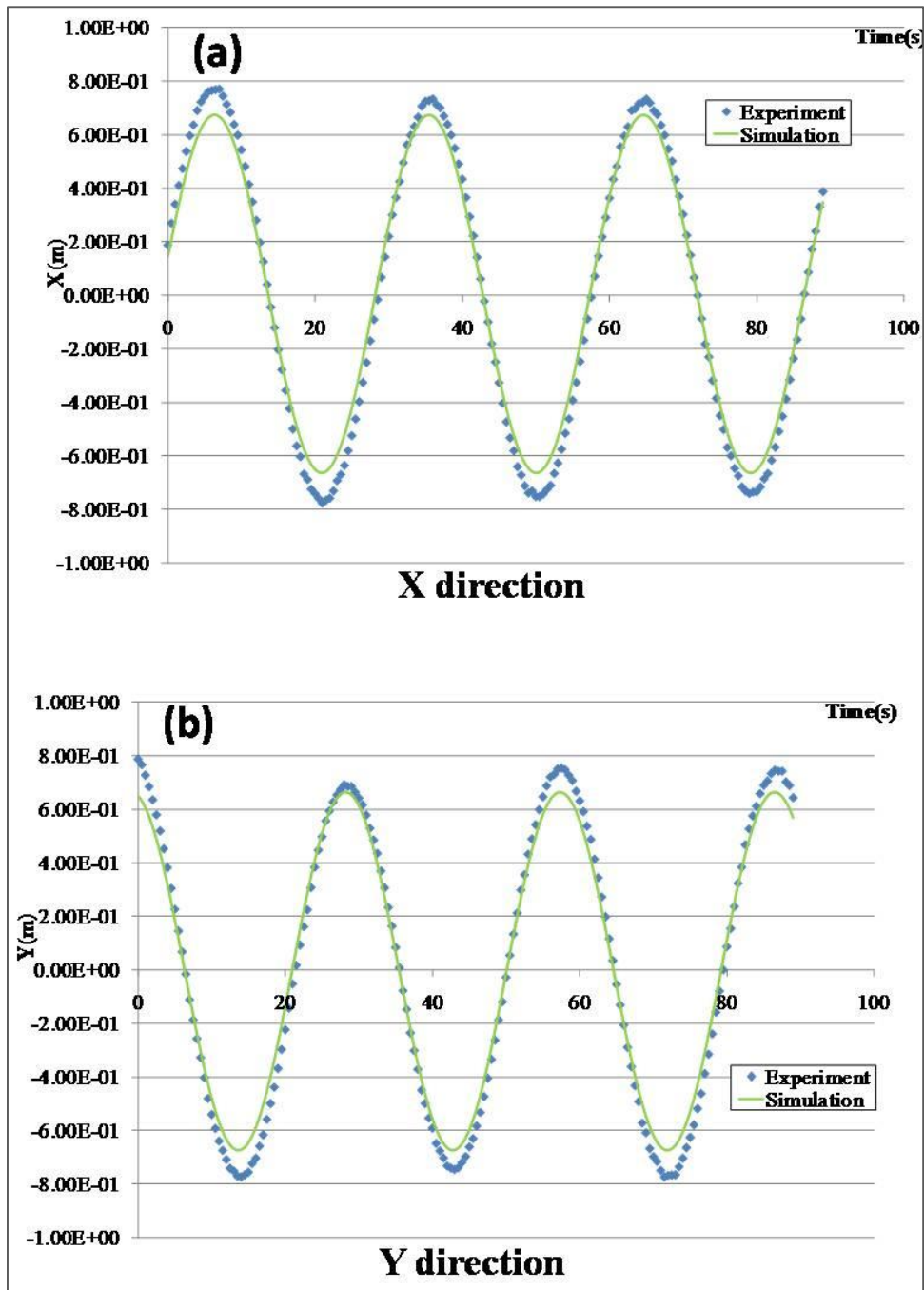
**Fig. 4.13 Path of the centre of gravity of the models for spiral motion in 3D space**

Fig. 4.14 shows the comparison of the experimental and simulation results of the trajectories of the centre of gravity in a bird's eye view of the  $XY$  plane,  $YZ$  plane and  $ZX$  plane.



**Fig. 4.14 Trajectory of the centre of gravity of the models in (a)  $XY$ -plane, (b)  $YZ$ -plane and (c)  $ZX$ -plane**

In Fig. 4.14a, it is seen that the radius of experimental result is little bit larger than that of the simulation; which might be because of the difficulty of reading the actual value of the experimental data and/or due to the tension effect of cable. The time series of distance of  $x$ ,  $y$ ,  $z$  direction and turning angle are shown in Fig. 4.15. From these results, we can see that this simulation result is in excellent agreement with experiment's one.



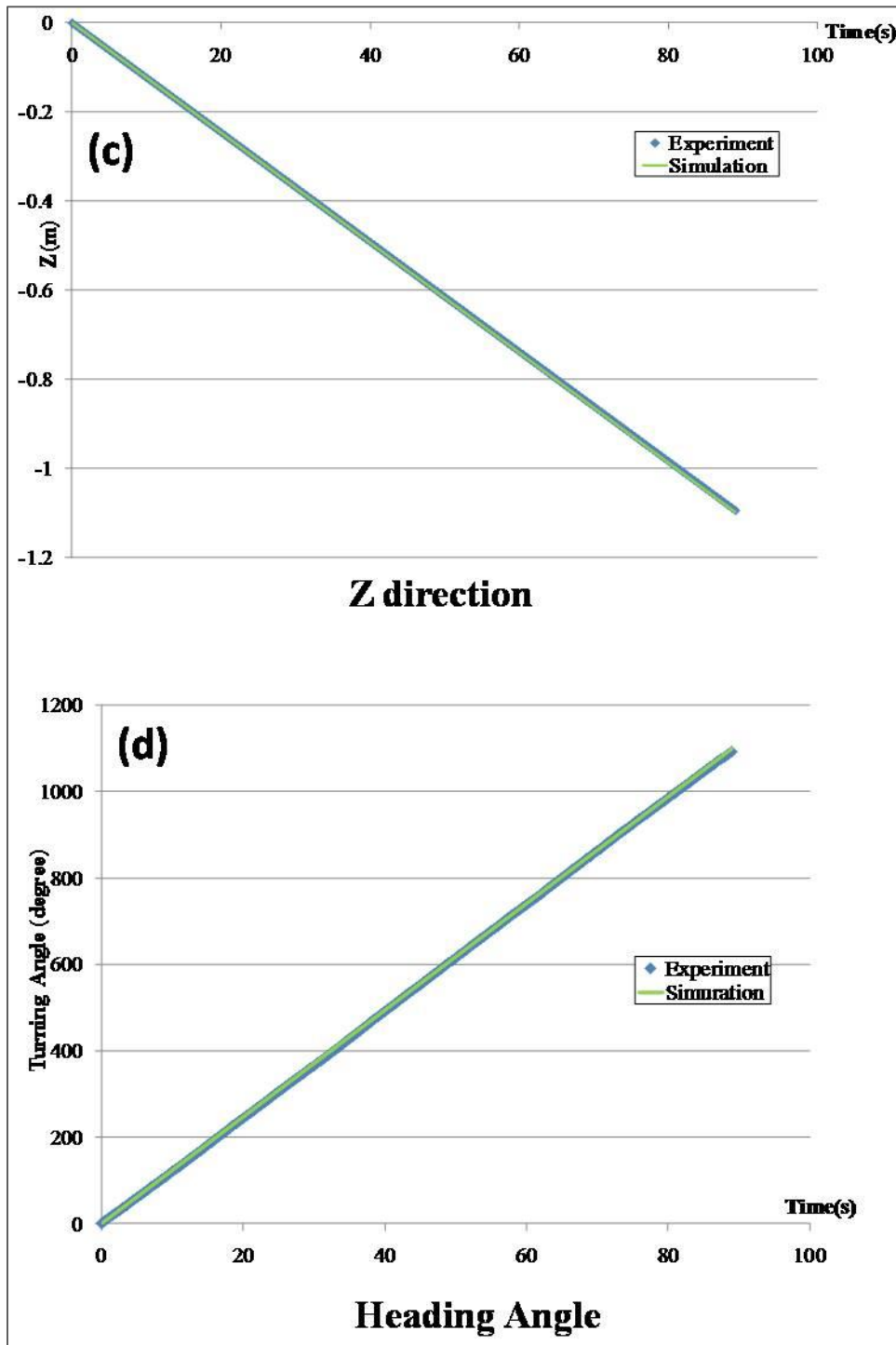


**Fig. 4.15** The time series of X, Y, Z direction and heading angel

Six seconds interval snapshots from the video clip of the comparison in spiral motion are shown in Fig. 4.16. The series of pictures in the left column and the right column are the view captured by top

camera and the side underwater camera respectively. The top view might be seemed like the circular motion however the combined observations of the pictures of the cameras revealed that the model is concurrently in circular and in downward motions, i.e. spiral motion. It is also observed that the robots are in almost similar motion, which proves the accurateness of the simulation. Finally, from the above discussion it can be concluded that our program can predict the 6-DOF motion in 3-dimensional space successfully.

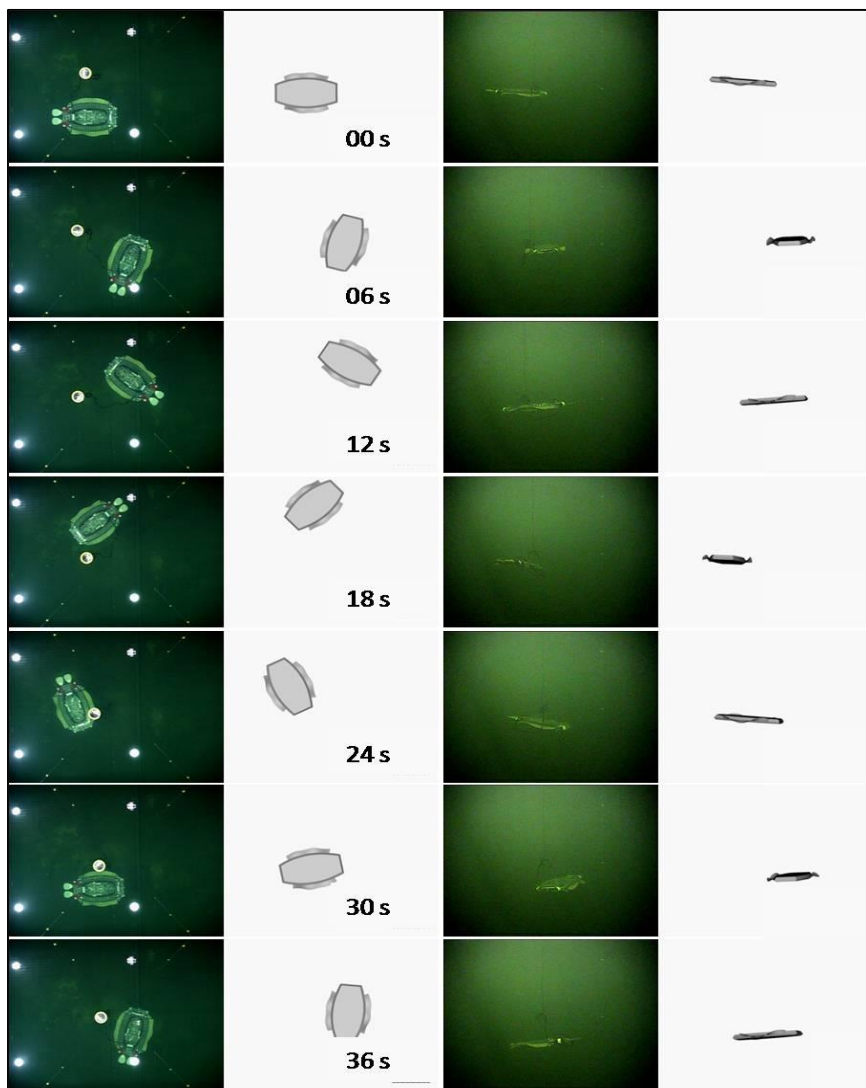


**Fig. 4.16 Comparison of simulation result and experimental film in case of spiral motion by only side fins in 3D space**

#### 4.4.5 Real Time Simulator

At the last stage, applying the derived mathematical model the real time simulator for Model-4 was developed. The simulation system was developed with the help of Open Dynamic Engine (ODE) based on the equation of motion discussed in the section 4.3.1. ODE is an open source for simulating rigid body dynamics. The model was embedded in the ODE for making the visualization, background etc. The simulator was the combination of the mathematical model and ODE. The operation in this simulation allows operating the model in the simulator by using the controller of a video game which is same as the controller of real robot. In this simulation, the robot in the simulator can be operated by human control. The frequency, the maximum fin angle, the caudal fin angle can be changed freely even during the operation. The centre of oscillation of the side fins, vertical distance between the center of buoyancy and the center of gravity can also be changed in the program by changing the initial setting. The default input form of ODE is shown in Fig. 4.17 .

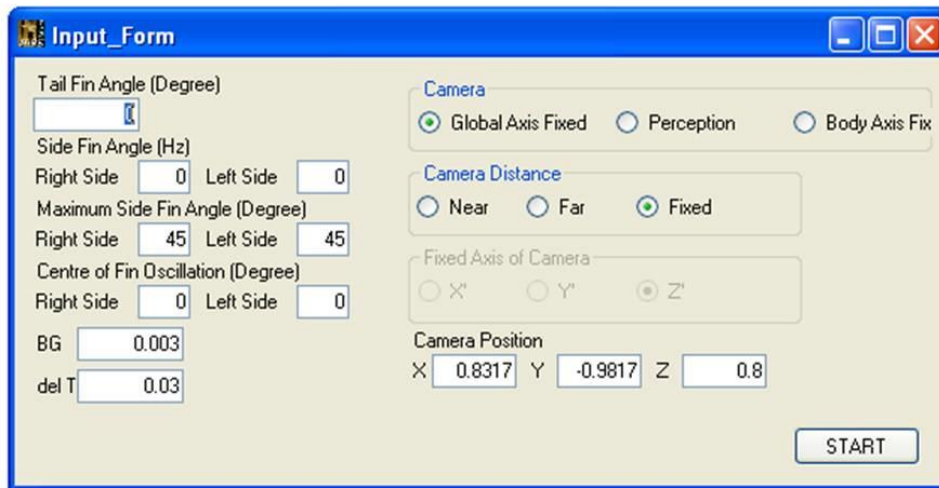


**Fig. 4.17 Default input form of ODE**

The screen image of the real time simulator, the controller and the joystick are shown in Fig. 4.18. The motion of each side fins can be controlled by the controller similarly as the real Model-4.

Additionally by using the controller, the frequency of each side fins could be changed which made it easier to control the motion of the robot in this simulator.

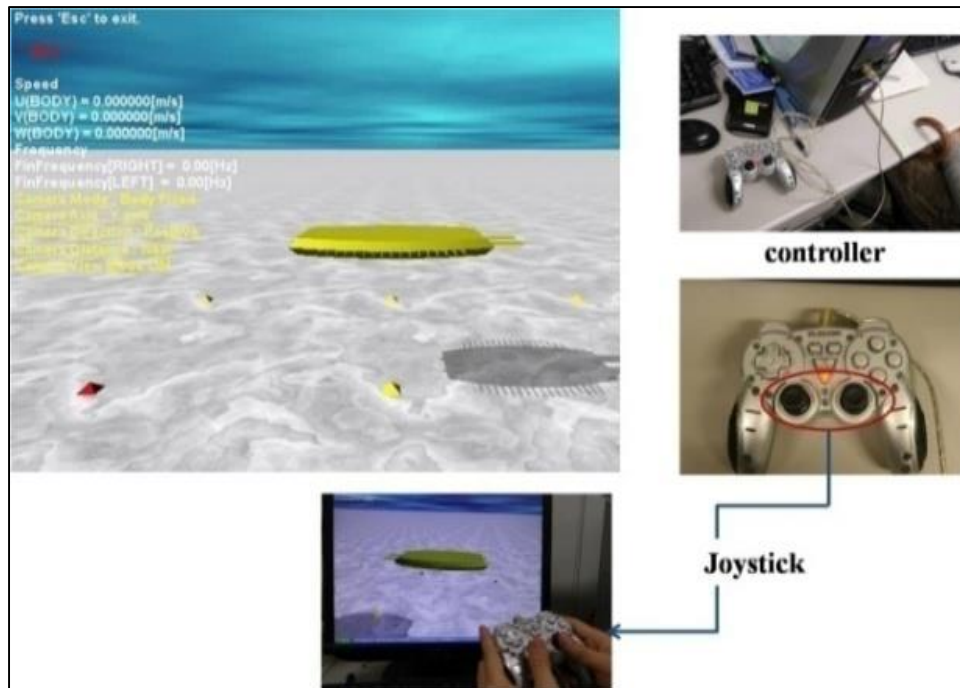


**Fig. 4.18 Picture of the real time simulator with controller and joystick**

During the operation, it is also possible to change the viewpoint of the camera to observe the animation from different position; some snap shots are shown in Fig. 4.19. With this simulator, it became possible to create any type of regular or irregular motions without complex operation including braking motion. The simulator is very easy to handle. Even the little children can operate the robot in the simulator like video game.

To verify the accuracy of the simulator, the motion of the model in the simulator was compared with that of the real model by the same control. Fig. 4.20 shows the video clip at every 2 seconds as an example of movement of the real time simulator with the real robot. In this figure the model shows the forward motion, stopping motion and rotation motion. It is seen that the model starts movement to

forward direction then brakes at 2 seconds and then starts rotation after 4 seconds. From this figure, it is also observed that the robot's motion in this simulator is very similar to the real Model-4's motion by the same control. Therefore it can be concluded that this simulator is a practically usable one for operation training to improve the operators' adeptness.

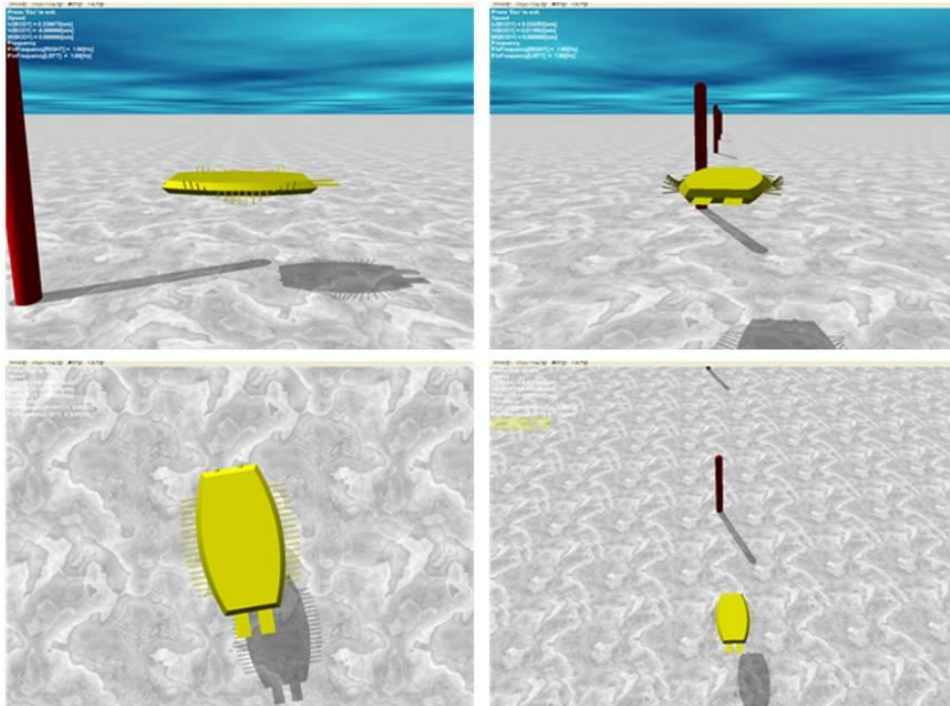


**Fig. 4.19 Robot in the simulator at different viewpoint of camera**

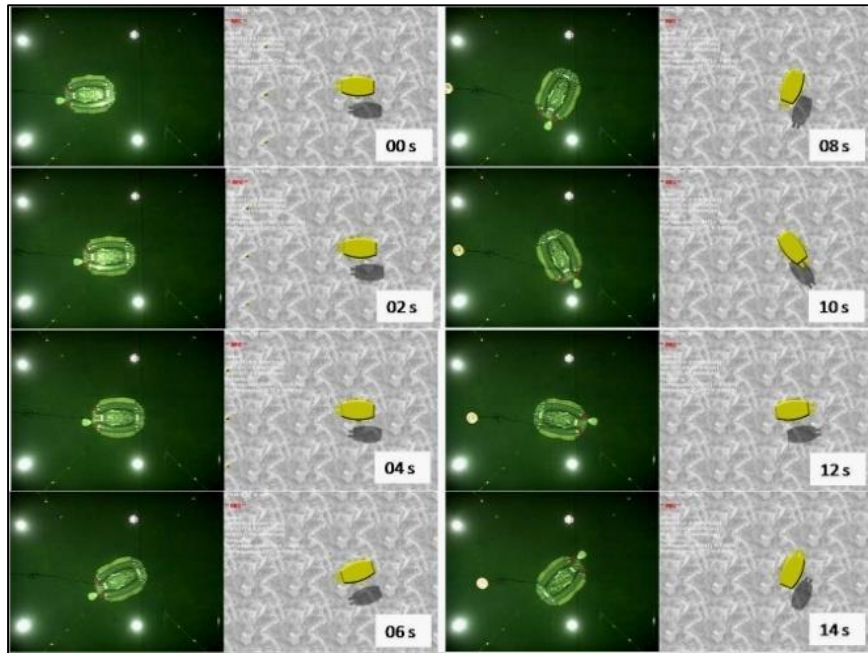


**Fig. 4.20 Comparison experimental film and the real time simulator**

#### **4.5 Summery**

The mathematical model of 6-DOF motion of the Model – 4 of Squid-like underwater robot with two undulating side fins was developed. The simulation was done for free run condition and compared with the experimental results. The accuracy of the model was confirmed. Finally, using this mathematical model, a real-time simulator was developed. It was confirmed that the robot in this simulator can be controlled in the similar way as real robot by the same control. This simulator is capable of making any type of motion. It can be used in the operation training to improve the skill of operators as well as for other purposes.

## 5. Chapter 5:

### 5.1 General Conclusion

The contribution of the author in the development of a competent and environmentally friendly underwater robot has been discussed in this thesis. The study on the Squid-like underwater robot with two undulating side fins can be divided in two main parts; first, the CFD computation of the flow field around the robot; second, the simulation of motion including braking motion of the undulating fin propulsion system. In both cases, the experimental study has been conducted or collected data from previous study. From the above study, the following points can be written in conclusion:

1. The CFD computations around a flat body with two undulating side fins and the real Model-4 have been conducted. The relationship between the relative velocity of fluid and the fin's surface were investigated based on the distribution of pressure difference of upper and lower surfaces and thrust force distribution. The computational model exhibited a considerable agreement with the empirical observations. A simple relationship among the fin's principle particulars and hydrodynamics was established using the computed result. The comparison between the force measurement and integrated force using CFD result for simple model showed that the CFD techniques can predict the hydrodynamic force produced by the undulating side fin.
2. The braking ability of the undulating fin propulsion system of the squid-like underwater robot has been investigated through experiment and simulation. The stopping motion by fin's stopping force and no thrust force for the translational and rotational motions were investigated. Good agreement between the experimental and simulation results was confirmed. It is confidently concluded that the undulating fins of the robot are capable of producing very large negative (stopping) thrust to stop itself instantly and within a very short distance. The breaking performance undoubtedly proves the applicability of this underwater propulsion system in the exploration of complicated areas of oceans with unprecedented control and minimal disturbances to the underwater environment.

3. The mathematical model of 6-DOF motion of the Model – 4 of Squid-like underwater robot with two undulating side fins was developed. The simulation was done for free run condition and compared with the experimental results. The accuracy of the model was confirmed. Finally, using this mathematical model, a real-time simulator was developed. It was confirmed that the robot in this simulator can be controlled in the similar way as real robot by the same control. This simulator is capable of making any type of motion. It can be used in the operation training to improve the skill of operators as well as for other purposes.

## **5.2 Future Plan**

Our continuous effort towards developing a competent and environmentally friendly underwater robot will be continue. In future, more investigation will be conducted on the present model. Form the computation result of Model-4, it was suggested that if the gap between the fin and body can be covered by extending the rubber sheet then the real model will produce more thrust. However more experimental and computational studies are needed to finalize the decision; this point will be taken in to consideration in future studies. The achieved knowledge from the previous studies will be used to develop new models. The fifth generation of the robot, Model-5 has already been developed. In the new model, the side fins were created by using the Scotch Yoke mechanism. This model is very simple and powerful. The experimental and numerical study on this model has been started. In future, different type of Scotch Yoke mechanism will be tested to find the most capable one. Moreover, the development of the control system of the robot will be continued simultaneously.

## References

- Azuma, A. and Nasu, K., (1977), The Flight Dynamics of an Ocean Space Surveying Vehicle, *Institute of Space and Science, Univ. of Tokyo*, Report No. 547, Pp. 41-90.
- Barrett, D.S., Triantafyllou, M.S., Yue, D.K.P., Grosenbaugh, M.A. and Wolfgang, M.J., (1999), Drag Reduction in Fish-like Locomotion, *J Fluid Mechanics*. Vol. 392, Pp. 183-212.
- Breder, C., (1926), The locomotion of Fishes, *Zoologica*, Vol. 4, Pp. 159-256.
- Bulletin of the Society of Naval Architects of Japan (1985), English Translation by Danish Maritime Institute in 1986, No. 668, Pp. 43.
- Cebeci, T., *An Engineering Approach to the Calculation of Aerodynamic Flows*, (1999), Springer: Horizons Publishing Inc. California, Pp. 14.
- Chen, C.J and Chen, H.C, (1984), Finite Analytic Numerical Method for Unsteady Two Dimensional Navier-Stokes Equation. *Journal of Computational Physics*, Vol. 53, No. 2, Pp 209-226.
- Harvald, S.A., (1983), *Resistance and Propulsion of Ships*, A Willy-Interscience Publication, Jhon Wiley & Sons, Pp. 4.
- Heo, S., Wiguna, T., Park, H.C. and Goo, N.S., (2010), Effect of an Artificial Caudal Fin on the Performance of a Biomimetic Fish Robot Propelled by Piezoelectric Actuators, *Journal of Bionic Engineering*, Vol. 7, Pp 113-119.
- ISABMEC (2000), *Proceedings of 1st International Symposium on Aero Aqua Bio-Mechanisms*, Honolulu, Hawaii, USA.
- ISABMEC (2003), *Proceedings of 2nd International Symposium on Aero Aqua Bio-Mechanisms*, Honolulu, Hawaii, USA.
- ISABMEC (2006), *Proceedings of 3rd International Symposium on Aero Aqua Bio-Mechanisms*, Ginowan, Okinawa, Japan.
- ISABMEC (2009), *Proceedings of 4th International Symposium on Aero Aqua Bio-Mechanisms*, Shanghai, China.
- ISABMEC (2012), *Proceedings of 5th International Symposium on Aero Aqua Bio-Mechanisms*, Taipei, Taiwan, 2012.
- Kato, N. (2000), Control Performance of Fish Robot with Mechanical Pectoral Fins in Horizontal Plane, *IEEE J Oceanic Eng.*, Vol. 25, No. 1, Pp 121-129.

- Kato, N., Ayers, J. and Morikawa, H., (2004), Bio-Mechanism of Swimming and Flying, *Springer-Verlag*, Tokyo, Japan.
- Low, K.H., (2009), Modelling and Parametric Study of Modular Undulating Fin Rays for Fish Robot, *Mechanism and Machine Theory*, Vol. 44, Pp. 615-632.
- Rahman, M.M., Toda, Y. and Miki, H., (2010), Study on the Performance of the Undulating Side Fins with various Aspect Ratios using Computed Flow, Pressure Field and Hydrodynamic Forces, *Proceedings of the 5<sup>th</sup> Asia-Pasific Workshop on Marine Hydrodynamics*, Pp. 333-338, Osaka, Japan.
- Rahman, M.M., Toda, Y. and Miki, H., (2010), Computational Study on the Fish-Like Underwater Robot with Two Undulating Side Fins for various Aspect Ratios, Fin Angles and Frequencies, *Proceedings of the International Conference on Marine Technology (MARTEC)*, Pp. 29-34, Dhaka, Bangladesh.
- Rahman, M.M., Toda, Y. and Miki, H., (2011), Computational Study on a Squid-Like Underwater Robot with Two Undulating Side Fins, *Journal of Bionic Engineering*, Vol. 8, No. 1, pp.25-32.
- Rahman, M.M., Miki, H., Yamamoto, R., Sanada, Y. and Toda, Y., (2012), Study on the Braking Performance of a Biomimetic Squid-Like Robot with Two Undulating Side Fins, *Proceedings of the 6th Asia Pacific Workshop on Marine Hydrodynamics*, pp. 547-552, Johor Bahru, Malaysia.
- Rahman, M.M, Miki, H., Sugimori, S., Sanada, Y. and Toda Y., (2013), Development of a Real Time Simulator Based on the Analysis of 6-Degrees of Freedom Motion of a Biomimetic Robot with Two Undulating Side Fins, *Journal of Aero Aqua Bio-mechanisms*. Vol. 3, No. 1, Pp 71-78.
- Rahman, M.M., Sugimori, S., Miki, H, Yamamoto, R, Sanada, Y. and Toda, Y., (2013), Braking Performance of the Undulating Fin Propulsion System of a Biomimetic Squid-Like Underwater Robot, *Journal of Bionic Engineering*. (Accepted)
- Riggs, P., Bowyer, A. and Vincent, J., (2010) Advantages of a Biomimetic Stiffness Profile in Pitching Flexible Fin Propulsion. *Journal of Bionic Engineering*, Vol. 7, Pp.113-119.
- Sfakiotakis, M., Lane, D.M. and Davies J.B.C., (1999), Review of Fish Swimming Modes for Aquatic Locomotion, *IEEE Journal of Oceanic Engineering*, Vol. 24, No. 2.
- Shang, L., Wang, S., Tan, M., and Dong, X., (2009), Motion Control for an Underwater Robotic Fish with two Undulating Long-Fins, *28<sup>th</sup> Chinese Control Conference*, Shanghai, P.R. China.

- Tahara, Y. (1993), Computation of Viscous Flow around Series 60 Model and Comparison with Experiments, *Journal of Kansai Society of Naval Architects*, Vol. 220, Pp. 29-47.
- Toda, Y., Hieda, S. and Sugiguchi, T., (2002A). Laminar Flow Computation around a Plate with Two Undulating Side Fins, *Journal of Kansai Society of Naval Architects*, Japan, No. 237, Pp. 71-78 (In Japanese).
- Toda, Y., Fukui, K. and Sugiguchi, T., (2002B), Fundamental Study on Propulsion of a Fish-like Body with Two Undulating side Fins, *Proceedings of the 1<sup>st</sup> Asia Pacific Workshop on Marine Hydrodynamics*, Pp. 227-232, Kobe, Japan.
- Toda, Y., Suzuki, T., Uto, S. and Tanaka, N., (2004). Fundamental Study of a Fishlike Body with Two Undulating Side-Fins, *Bio- Mechanisms of Swimming and Flying*, Springer, Pp. 93-110.
- Toda, Y., Ikeda, H. and Sogihara, N., (2006). The Motion of a Fish-Like Under-Water Vehicle with two Undulating Side Fins, *Proceedings of the Third International Symposium on Aero Aqua Biomechanisms* S. No. 27, Ginowan, Okinawa, Japan.
- Toda, Y., Danno, M., Sasajima, K and Miki, H., (2009), Model Experiments on the Squid-Like Under-Water Vehicle with two Undulating Side Fins, *Proceedings of the 4<sup>th</sup> International Symposium on Aero Aqua Biomechanisms* , S. No. 45, Shanghai, China.
- Zhang, Y.H., He, J.H., Yang, J., Zhang, S.W. and Low, K.H., (2006), A Computational Fluid Dynamics (CFD) Analysis of a Undulatory Mechanical Fin Driven by Shape Memory Alloy, *International Journal of Automation and Computing* , Vol. 4, Pp. 374-381.
- Zhang, Y, Jia, L-B, Zhang S-W and Low, KH (2007). “Computational Research on Modular Undulating Fin for Biorobotic Underwater Propulsor”, *Journal of Bionic Engineering*, Vol. 4, No. 1, Pp. 25-32.
- Zhang, Y., He, J. and Low, K.H., (2012), Parametric Study of an Underwater Finned Propulsor Inspired by Blue-spotted Ray. *Journal of Bionic Engineering*, Vol.9, Pp. 166-176.
- 
-